

University of Nottingham
UK | CHINA | MALAYSIA

PhD Thesis

Towards an atomic Sagnac interferometer with full dynamical control of atoms in ring waveguides

Candidate: Fabio Gentile

Supervisor: Ass. Prof. Thomas Fernholz

18th August 2019

Thesis submitted to The University of Nottingham for the degree of Doctor of Philosophy

Cold and Ultracold Atoms Group
School of Physics and Astronomy

To my child, who's on its way to join us in this world.

Abstract: The advances towards a fully guided matter-wave rotation sensor are illustrated in this document. As in optical gyroscopes, the presented interferometer is based on the Sagnac effect, i.e. the phase difference accumulated between two waves counter propagating in a closed loop that is rotating with respect to an inertial frame of reference. Besides being a recent field of study, atomic Sagnac interferometry already presents results comparable to commercial devices based on the well established optical technology. Differently from other atom based devices, in the studied scheme atomic clouds are steered around a ring trap in a controlled fashion, instead of using free propagating atomic beams. This thesis reports on the current status of the experimental apparatus and on the experimental feasibility of the interferometric protocol. Moreover, a new technique to produce closed loop lattices is presented. This consists in dressing a ring shaped magnetic quadupole with multi-pole fields oscillating in the radio frequency regime. The state dependent potential landscape produced is dynamically controllable and can be used to improve the current interferometric design. Moreover, it opens for more fundamental applications in lattice physics and, in general, quantum simulators.

"O frati," dissi, "che per cento milia
perigli siete giunti a l'occidente,
a questa tanto piccola vigilia

d'i nostri sensi ch'é del rimanente
non vogliate negar l'esperïenza,
di retro al sol, del mondo sanza gente.

Considerate la vostra semenza:
fatti non foste a viver come bruti,
ma per seguir virtute e canoscenza".

Dante Alighieri
La Divina Commedia – Inferno, canto XXVI.

1. Acknowledgements

Many people crossed my path in these four years spent in Nottingham. I became friend with some of these people, others were somehow neutral to me and me to them and with some there wasn't much understanding or we simply didn't like each other. There wouldn't be time to thank them all, but each single one of them contributed to shape the person I am now. Here I'll be mentioning only some of these people, with my deepest apologies for the others.

I would like to start thanking Mark Fromhold and Michael Holynski who evaluated my work and helped me re-evaluating it from a different perspective.

Within the university, in the research group of Cold Atoms, I'd like to thank Thomas Fernholz, for his guidance and useful comments on the draft of the thesis, and all the other collaborators on the 'RingLab' project: Stefano Bettelli who I never personally met, actually, but it feels like I had since he initiated this research project and worked out most of the preliminary designs and notes; Thomas Bishop, the first PhD student working on this project; Mark Bason with whom I spent a lot of time aligning the optics and building the experimental apparatus; Jamie Johnson, whose help during the last period of the PhD has been very precious; Kostas Poulios for helping me and Jamie to push for a project that otherwise would have remained on the 'maybe' list; and to Vilius Atkočius I wish the best of luck!

I'd like to thank my colleagues from the 'Memory Lab' and "Magnetometry Lab": Bethany Foxon and Sindhu Jammi, who helped me taking measurements with their experimental apparatus; and Tadas Pyragius, Hans Marin Florez and Sanjay Kumar for sharing opinions, comments and suggestions.

In the present and former Cold Atoms group I'd like to thank: Lucia Hackermüller, Nathan Cooper, Jon Nute, Asaf Paris Mandoki, Jizhou Wu, Samanta Piano, Somaya Madkhali, Hayat Abbas, Vineeta Naniyil, Reece William Saint, Amruta Gadge, Fedja Oručević, William Evans, Xiaoke li, Tom Barrett, Tim

James, Peter Krüger.

Among these colleagues there's been some that have been more than colleagues. With them I shared laughs, frustrations, adventures and a lot meals (lunches and dinners: in the week, late at work, while working in the weekends or just in our free time): Jorge Ferreras, Elisa da Ros, Lars Körner and Simon Svatek.

Also I'd like to thank the people that had, for a long time, the patience necessary to share a house with me: Miguel Socolovsky, Nephtalí Garrido Gonzales and Felipe Maykot and later on Valeria Maroni.

Besides the academics, there a plethora of incredibly skilled professionals that *make it happen* (they really do): Pete Smith, Tommy Napier, Susan Warburton, Andrew Solomon, Ian Taylor, Stuart Andrew, Terry Wright, Phil Parry and many others. Thanks a lot for your help!

Moving away from the workplace, other people and other activities filled my soul and ensured that I did not lose my mind on the way. Even if they are not really aware that they helped me, they have been absolutely crucial. The Judo Club is one of these realities, an extended family in which people have a different idea of what an hug is! Thanks to all people that have been rolling, sweating, suffering and joking with me. Specially, of all the judokas, I'd like to mention two people: William James Austin and Cameron Jackson. Also, I would like to thank Michael (Mike) Ian Smith managing the Climbing Club at the university and, in general, the climbing community in Nottingham that hang around the Depot and the Nottingham Climbing Centre. The Post Graduate New Theatre, a self organised group of amazing people from any sort of discipline and nationality across the university with whom I had the opportunity to enjoy great human experiences on the stage, in the backstage and outside the theatre.

I am immensely thankful to the Consuelling Service of the University Specially to Maggie Shen who guided me into seeing things from a different perspective.

Thanks to all the friends that helped me during these years. Specially, I would like to thank Giulia Cappetti and my close-even-if-far-away friends Francesco Ferrari and Linda Vissers.

I wish to thank my family, always there to support me. Thanks to my parents Anna Maria Roggio and Crescenzo Gentile who fed me of everything I could need of: love, food, music, education, sport and much more. Thanks to my sister Tiziana Gentile for teaching me what determination means and for listening to

me when nobody else does, and to my brother Luca Gentile for treating me like a brother even though I am his brother.

Last, but not the least, thanks to Julie Daujat. Thanks for walking my same path, for supporting me every day, for coming with me in the past adventures and in the ones to come.

Contents

1. Acknowledgements **6**

2. Introduction **1**

3. Atom interferometry **9**

3.1. Splitters reflectors and re–combiners 10

3.1.1. Nano–gratings 10

3.1.2. Light gratings 11

3.1.3. Light–atom interactions 11

3.2. Phase difference in an atom interferometer 12

3.3. Sagnac Atom interferometers 15

3.3.1. Sagnac Effect 15

3.3.2. Phase of Sagnac Atom Interferometers 19

3.3.3. Time domain vs Space domain 20

4. Guided matter–wave Sagnac interferometry **22**

4.1. Sagnac interferometry with atomic clocks 23

4.1.1. Interferometric protocol 26

4.1.2. Interferometric signal 28

4.2. Dressed potentials 32

4.2.1. Dressed quadrupole ring 35

4.3. About the experimental realization of guided matter wave interferometers 40

4.3.1. Alternative experimental schemes 41

4.3.2. Challenges of this specific implementation 44

5. Experimental apparatus **50**

5.1. Rubidium Structure 50

5.1.1. Coarse structure 51

5.1.2. Fine structure 52

5.1.3. Hyperfine structure . . . 52
5.1.4. Interaction with magnetic fields for Rubidium and trapping techniques . . . 54
5.2. Lab layout . . . 57
5.3. Vacuum chamber and external coils . . . 57
5.3.1. Coils on the chamber . . . 62
5.4. Laser setup . . . 63
5.4.1. Optical tables . . . 65
5.4.2. On chamber optics . . . 66
5.5. Chip Design . . . 69
5.5.1. Ring quadrupole electro–magnet . . . 70
5.5.2. Radio–frequency chip . . . 73
5.5.3. Printed Circuit Board for loading atoms in the chip . . . 74
5.5.4. Assembly . . . 76
5.5.5. Loading Sequence . . . 78
5.6. Rate Table . . . 80
5.6.1. Rate table protection . . . 81
5.6.2. Performances . . . 84

6. Experiments **87**
6.1. Early stage experiment . . . 87
6.1.1. Magnetic fields: from MOT to ring . . . 91
6.1.2. Optical pumping . . . 93
6.1.3. Recapture . . . 95
6.1.4. Temperature estimation . . . 96
6.1.5. Results . . . 97
6.2. Three pulse Ramsey sequence . . . 99
6.2.1. Theoretical model . . . 99
6.2.2. Microwave and radio-frequency dressing . . . 101
6.2.3. Sequence . . . 104
6.2.4. Results . . . 108

7. Ring lattices with multi-pole radio-frequency dressing **113**
7.1. Multi-pole fields . . . 114
7.1.1. Amplitude variation across the torus . . . 115

7.2. Coupling terms 116
7.2.1. Toroidal confinement 118
7.3. Geometrical considerations 120
7.4. Overlap of wave functions 124
7.5. Multi-pole fields using planar wire structures 128

8. Conclusions and Outlook **133**

A. On rubidium structure **139**
A.1. Coarse structure 139
A.2. Fine structure 140
A.3. Atom-magnetic field interaction 141
A.3.1. Optical molasses and Magneto Optical Traps (MOT) . . . 142

B. Complex plane representation of 2D magnetic multipoles. **146**
B.1. Bi-dimensional multipoles. 146
B.1.1. Amplitude of a magnetic multipole field in the origin . . . 147
B.1.2. Behavior in the neighboring of the origin. 149

Bibliography **153**

2. Introduction

The subject of this thesis is to report on the development of an high precision atom-based rotation sensor.

The working principle of this sensor relies on interference phenomena. Specifically, it uses the phase difference accumulated by waves counter propagating in a closed loop, namely the Sagnac effect [1]. As a matter of fact, interferometry techniques are widely used in precision metrology, spanning any range of applications: from experimental testing of fundamental physics as gravitational wave detection and Michelson-Morley experiments [2, 3], to industrial applications as geometric measurements and profilometry [4], to the definition of the unit of mass in the International System of Units (SI) [5]. Also, its applications include a wide variety of scales: from astronomic measurements [6] to attometer vibrometry [7].

In most of the interferometric devices the oscillating field used for the observation of interference is represented by electromagnetic waves with a various range of wavelengths. Conversely, this sensor makes use of the undulatory property of matter, exploited via quantum mechanical treatment, to observe interference [8, 9, 10].

As frequently pointed out in the literature, atom-based Sagnac interferometers present a remarkable enhancement of the size-accuracy ratio [11, 12], with respect to their optical counterpart.

For this specific sensor, further fundamental advantages justify this specific atom based design, as will be pointed out in Section-4.1.1 on page 26. To better appreciate the advantages and disadvantages of this sensor, it is useful to point out how rotation sensing is employed in various industrial and research fields, together with the requirements needed within each specific application.

The outcome of a measurement using interferometric techniques, corresponds to the average of the signal over a certain time period τ. Since this corresponds to a numerical integral over time, τ is also referred as integration time. The

standard deviation of a measurable over a certain integration time is referred as sensitivity and presents units of $\propto 1/\sqrt{\tau}$. When evaluating the performances of an interferometer, one usually refers to the sensitivity of the interferometer and to the maximum accuracy observed. This can be the accuracy obtained after a certain long integration time, or in case external noise sources limits the accuracy level after a certain integration time, the so–called bias–stability.

In the following paragraphs are listed the accuracy and sensitivity levels required for applications in inertial navigation systems, rotational seismology and fundamental research. Successively, a description of various categories of rate sensors and corresponding performances are indicated.

Inertial navigation: One of the most appealing industrial applications of rotation sensing is represented by inertial navigation. An inertial navigation system (INS) is necessary whenever a global navigation satellite system (GNSS) is not available (every time that an unobstructed line of sight between the navigation system and the satellites cannot be achieved, e.g. underground or under water) or as a supporting navigation device.

This last backing role is crucial in the airway sector, where interference caused by external interfering signals (due to natural phenomena or even intentional, 'jamming', activities [13, 14]) can cause to the complete disruption of the positioning system, leading to potentially disastrous outcomes [15, 16]. This weakness of the GNSS is well known and research activity is very active on this topic [17].

Conversely to GNSS, INSs are robust to electromagnetic interference. This because an INS keeps track of the variations of accelerations and rotation from a known initial condition of position and orientation. The current position is then evaluated through double integration over time of the registered measurements [18]. It is then evident that high accuracy estimation of the initial position and orientation, as well as their evolution through time, is of crucial importance to the performance of an INS.

For inertial navigation purposes gyroscope performances are commonly categorized in grades, depending on their application. The higher end of the classification sees Inertial and Strategic grade categories requiring sensitivities $< 1.5\times10^{-6}\, rad/\sqrt{s}$ and $< 5.2\times10^{-6}\, rad/\sqrt{s}$ respectively [19]. Recently, record sensitivity on commercial devices has been reported in the order of $2.9\times10^{-9}\, rad/\sqrt{s}$.

This would allow geo-localisation systems to achieve position uncertainty below 1 nautical mile after a month of navigation [13].

Seismology: In geophysics there is an increasing interest in the study of seismic rotational waves [20], also known as rotational seismology. The study of seismic excitations is performed through recordings of the displacement, under the assumption of isotropic elastic media the displacement can be described as a sum effect of a compressional (referred as primary or P) and a shear (referred as secondary or S) wave components, the first of which is irrotational by definition.

Rotation measurements allow then to isolate the S component and evaluate the ratio of the magnitude of the two fields (see reference [21]). This can be useful for determination of the mechanical properties of the transmission medium.

For weak motion seismology a sensor usually required to be able to measure $10^{-7}\,rad/s$ with periods between 10 and 100s [22]. Also rotational sensors have been used in earthquake engineering to study the seismic behaviour of complex civil structures [23]. While requirements for these specific applications are not explicitly stated in the literature, typical performances see accuracy in the order of $6 \times 10^{-7}\,rad/s$ with sensitivities of about $4 \times 10^{-6}\,rad/\sqrt{s}$ [24].

Fundamental research: Advanced rotation sensors are employed in General relativity tests [25, 26] as the evaluation of the Lense-Thirring (L-T) [27] and de Sitter effects [28], i.e. the resulting reference frame drag due to a rotating massive object and the deformation of vectors orbiting around a massive object. While the de Sitter effect has been experimentally demonstrated with Gravity probe-B [28], the L–T effect has not been directly measured yet. A proposal aiming to evaluate this effect is the GINGER (Gyroscopes IN General Relativity) project [25]. Both of these effects produce rotation rates in the order of $10^{-14}\,rad/s$ [25]. It is to be remarked that the gyroscopes in the GINGER project are also used for far field rotational seismology [29].

Along with the applications, it is beneficial to mention what are the techniques used to achieve high accuracy rate sensors. In the following some of the most used technologies for rotation probing are mentioned, together with their best performances.

Mechanical gyroscopes: Mechanical gyroscopes rely on the conservation of the angular momentum of a rotating body. Practically, they are composed by a massive object spinning at a high rate. The analysis of the precession dynamics caused by an external torque is then used to extract information about the change in direction. Alternatively feedback controlling torque generators can be used to suppress precession dynamics. Monitoring the back-action of the torque generators can then be used to extract information of the direction.

Electro-statically Suspended Gyroscope (ESG) represents the mechanical gyroscope achieving best performances. It consists of a spinning Beryllium sphere electro-statically suspended in hard vacuum. The sphere is initially spun at very high rate and successively allowed to coast with respect to the case. The relative inclination between the case and the direction of the spin can then be detected electronically or optically[18].

Well engineered ESGs fall into the strategic grade performance, previously mentioned. Exceptionally accurate ESGs were utilized in the gravity probe-B experiment with pointing accuracy of $9.8 \times 10^{-7}\, rad$ [30, 31, 28].

For INS applications this device presents some technical and practical difficulties. For instance, the manufacture of the spinning ball is required to fit sufficient accuracy, and the read-out system needs to be designed such to perturb the rotation motion as little as possible. Also, damages to the sphere can occur in case of power supply failures [19, 14].

Optical Gyroscopes: These are devices relying on the Sagnac effect to perform rotation measurements. This technology is the most used for navigation applications, since it offers high precision measurements into relatively compact devices whose size is comparable to the one of a suitcase. More importantly, Fibre Optical Gyroscopes do not require mechanical moving parts; so these sensors can be directly fastened to the vehicle, with enhanced mechanical stability w.r.t. other devices [32, 14]. This property is usually referred to as strap-down, literally meaning that the device can be strapped down to the vehicle [18].

Ring Laser Gyroscopes (RLG) are based on a closed loop (ring) resonant cavity composed by a set of high reflectivity mirrors and a semi-reflective (output) one. Two beams are counter-propagating into the cavity and are emitted at the output mirror. If the cavity is not rotating the beams on the output are at the same frequency. In case the cavity is rotating, the optical paths of the two beams are

slightly different. As a result the output light will be modulated at the beating frequency [18].

These devices suffer from a mechanism known as mode locking. For very low rotations, the two counter-propagating beams oscillate at a very low frequency difference and due to weak coupling between the two counter-propagating beams (mainly generated by back scattering from the mirrors) they tend to self lock and oscillate at the same frequency [32]. As a result for low rotations a dead region of sensitivity applies. This effect can of course be damped by improving the characteristics of the mirrors with high quality reflection coating or using nano-fabrication techniques (see, for instance, reference [33]). Albeit, this leads to the reduction of the dead zone and not to its elimination. Another strategy used is to mechanically oscillate the resonator with a dither in order to avoid the dead zone [14]. Alternatively, two different amplifying media producing slightly different frequencies can be used.

Typical commercial device performance sensitivity: $1.2 \times 10^{-6} rad/\sqrt{s}$ bias stability of $6.7 \times 10^{-9} rad/s$. While, super large Ring laser Gyroscopes [34], used for geodesic studies, with enclosed areas of about $867 m^2$ can present accuracy down to $7.8 \times 10^{-12} rad/s$ [35].

An alternative optical-based family of devices is represented by Fibre Optical Gyroscopes or FOG. These consist of a spool of optical fibre, in which the light is introduced externally in both of the ends [36]. The coil diameter can be as large as 30 cm and contain a 10 km long optical fibre. This corresponds to a Sagnac interferometer of an area of 750 m^2, enhancing therefore the sensitivity of the interferometer. There are two main subgroups of FOG, the so called Resonant–FOG or R–FOG and Interferometric–FOG or I–FOG [14, 19].

The R–FOG working principle is similar to the RLG but the light is injected into the cavity that is now substituted with a spool of optical fibre. The output beat frequency is generated injecting two different frequencies in input. For instance, one of the input beam is maintained at a fixed frequency while the other is shifted by a controlled de-tuning. The output beat signal can then be processed for a feed-back loop that controls the de-tuning such that the beat signal is maintained at a specific frequency [19]. The finesse is much smaller than the one of a RLG but it is compensated by a much wider effective area given by the number of turns in the coil. It requires a sharp line-width of the light source and is easily affected by fibre imperfections.

The I–FOG requires a single frequency in input and uses a longer length of fibre w.r.t. a R–FOG. It can be treated as a very low finesse ring cavity with a large enclosed area. Its strength is that it does not require sharp spectral line of the input beam. On the contrary, the low coherence time of the light source causes the back-reflections in the fibre to dissipate quickly into white noise. The best performing I–FOG, to my knowledge at the present time, present a sensitivity of $2.9 \times 10^{-9}\, rad/\sqrt{s}$ [13].

Atomic Gyroscopes: These are a specific type of quantum interferometers, i.e. devices that using the quantum–mechanical wave–particle duality to perform interferometry with particles. First proposals and experiments involving matter–based interferometry were using electrons in the 1950's [37, 38] and neutrons in the 1970's [39]. Successively, the particle choice moved towards atoms. The concept of atom interferometry has been patented in 1974 [40] followed by experimental proposals in the second part of the 1980 decade [41, 42, 43].

Atom interferometers provide various advantages with respect to light. To begin with, atom interferometers offer shorter wavelengths than visible light interferometers as this is represented by the de Broglie wavelength λ_{db} and the speed of the wave can be controlled, conversely to photonic interferometers where the speed is fixed by the propagation speed of light in the used medium [12]. Furthermore, as in other branches of atomic physics, atom chip technology can be implemented to miniaturize the volume of the setup [44, 45]. Also with respect to other particle interferometers, the use of atoms offers a wider selection of properties, a larger cross section, better characterized environmental interactions, higher precision and portability [12].

On the other hand, atomic beams usually offer a shorter coherence length. This problem is usually addressed by implementing "white light interferometers" designs, i.e. interferometric schemes in which the period and position of the fringes is independent of the wavelength [12].

The challenge in atom interferometers is the necessity to implement the equivalent of optical elements (e.g. beam splitters and mirrors) to split deflect and recombine atomic beams. Equivalents to optical elements can be obtained using mechanical and optical gratings. Hence, using diffractive phenomena [12]. Among atomic interferometers, atomic gyroscopes can be categorized as:

Space domain: These atomic interferometers are produced with thermal atoms,

usually a collimated beam of atoms obtained with collimating slits preceding a heated atom source. In this type of interferometers the sensitivity increases with distance between splitters, for this reason they are usually referred to as space domain interferometers. The diffractive elements consist of mechanical gratings or lasers running in continuous mode [11]. The best performance achieved with space domain interferometers sees short term sensitivity at approximately $6 \times 10^{-10}\, rad/\sqrt{s}$ and long term sensitivity at about $3 \times 10^{-10}\, rad/s$ [46].

Time domain: This type of interferometers see cold atomic clouds actively launched with optical techniques in a parabolic trajectory. The diffractive elements are substituted by Ramsey sequences produced by pulsed lasers [11]. The sensitivity of these devices increases with the duration of the interferometric sequence. At the time being, the state of the art is represented by [47] with a short term stability of $1 \times 10^{-7}\, rad/\sqrt{s}$ and long term stability of about $1 \times 10^{-9} rad/s$ after $10000\, s$ of integration time.

Wave guide interferometers: Can be labelled as time domain interferometers but, conversely to the previous examples, in this case atoms are confined and actively moved during the entire interferometric sequence. The signal is recovered through population imbalance of two trappable states of a neutral atom. Experimental examples of guided atomic clouds are present in the literature [48, 49] but observation of interference phenomena are still lacking. Accordingly to [50] these interferometers can reach a short term sensitivity of roughly $10^{-9} rad/\sqrt{s}$ with a flux of $10^6\, atoms/s$ for an interferometer with a diameter of $1\, cm$.

The interferometer discussed in this thesis falls in the category of wave guide interferometers. As will be described in Section5.5.1, our setup sees a interferometric loop of $1\, mm$ in diameter, with a resulting expected short term sensitivity in the order of $10^{-7}\, rad/\sqrt{s}$, for atomic fluxes in the order of $10^6\, atoms/s$ [50]. This fulfils requirements for INS at the strategic level and for far field seismic investigation applications. Thus, the performances of this interferometer are expected to be comparable to commercial I–FOGs and high end commercial RLGs.

In the following chapters, the efforts for experimental demonstration of this device and the current status of the project will be reported. The structure of the thesis is organized as follows:

- Chapter–3 will focus on atom interferometers. An exhaustive description

of their working principle will be given, together with an illustration of the techniques used to implement the equivalents of optical elements in what is sometimes referred to as atom optics [8]. Specific attention will be given to Sagnac-type atom interferometers, describing how the rotation imprints a phase difference between the two arms of the interferometer and how this is translated in a population imbalance between two internal atomic states.

- In Chapter–4, an in-depth description of guided matter wave Sagnac interferometers, with specific attention to the scheme implemented in this project, will be provided. At the end of the chapter a more conscious description of the goals of this thesis will be listed.
- The description of the experimental setup built in the previous four years will be given in Chapter–5. This starts with the description of the atomic species used, i.e. the mass number $A = 87$ isotope of rubidium (^{87}Rb), together with an explanation of common trapping techniques used in atomic physics. Successively, it proceeds with illustrating the disposition and function of the experimental equipment in the laboratory area.
- A preliminary experiment, aiming to form a ring shaped magnetic trap using the fields produced by a commercial loudspeaker magnet will be illustrated in Chapter–6. Also, the realization of a three pulse Ramsey sequence on radio frequency dressed, magnetic sensitive, sub–levels of the hyperfine states of ^{87}Rb will be shown. This is formally equivalent to the interferometric protocol described in [50] that will be used in this project.
- In Chapter–7, making use of multi-poles oscillating at radio frequency regimes, a generalization of the trapping scheme described in [51] for an arbitrary number of minima will be shown. This can be used to to increase the size of the interferometer, and consequently its sensitivity. As previously mentioned, reaching interferometer sizes of about $1\,cm$, would allow for sensitivities in the order of $10^{-9} rad/\sqrt{s}$, matching best to knowledge performances of I–FOGs. Moreover, since the resulting potential landscape corresponds to a uni–dimensional lattice with periodic boundary conditions. Thus opening more fundamental applications in the area of lattice physics.

3. Atom interferometry

One of the fundamental ideas of quantum mechanics is that mass carrying systems, classically seen as particles, possess also an undulatory behaviour. Specifically, this concept (namely referred to as wave particle duality) states that a particle with momentum of modulus p can be associated with a wave characterized by the de Broglie wavelength

$$\lambda_{DB} = h/p \tag{3.1}$$

with h being the Planck constant. The idea of performing interferometric measurements using the wave particle duality of quantum mechanics was first demonstrated using crystal grating beam splitters for electronic beams by Marton et al. [52, 37, 38] and then accurately described in a patent by Altshuler and Franz [40]. Quoting from this patent, a "matter wave interferometric apparatus" comprises of:

> ‹‹
>
> *a. A source of particles;*
>
> *b. A beam splitter disposed in the path of the particles to split the particles into two distinct beams, each carrying a matter wave; said matter waves being in phase with each other;*
>
> *c. A first and a second beam reflector disposed in the path of each of said beams and so disposed as to reflect and then recombine the two beams;*
>
> *d. Means for detecting the recombined particles;*
>
> ››
>
> *S. Altshuler, L. Franz: "Matter wave interferometric apparatus" – US3761721A, 1973.*

This list, outlining a typical interferometric sequence, emphasize the need of few components required to build an atom interferometer. These are a source of particles, two coherent beam–splitters / re-combiners, two beam reflectors and a detector. The source of particles can be a very simple device as, for instance, an incandescent wire containing the desired atomic species or an oven heating up some material, these followed by two collimating slits. Suitable detection can be achieved with micro channel plate detectors or hot wire detectors. While to coherently split, reflect and recombine atomic beams diffractive techniques are commonly used.

3.1. Splitters reflectors and re–combiners

As previously introduced, interferometry with atoms requires the equivalent of the optical beam splitters and mirrors to form the interferometric path. A solution utilized in various experiments is to adopt diffraction techniques [12]. These can be based on transmission gratings, i.e. thin membranes with periodic slits, or light gratings, that is two counter–propagating light beams forming a standing wave or making use of light–atom interaction phenomena.

3.1.1. Nano–gratings

A nano–grating consists of a screen presenting an array of uniformly distributed slits whose size and separation lie in the sub–micron scale. When a coherent beam, having transverse wavelength larger than the distance between neighbouring slits hits a grating, the waves transmitted past the grating can be treated as coherent waves originated from each single slit [12, 53]. This results in preferred transmission directions, ruled by the grating equation

$$d \sin \theta_n = n \lambda_{DB}, \quad n \in \mathbb{Z} \tag{3.2}$$

where θ_n is the refraction angle relative to the n-th order and d is the period of the grating. This provides a technique to deflect part of a collimated beam into a desired angle θ_n. Opportunely placing three sets of gratings it is possible to produce closed paths between different trajectories, thus producing valid interferometric schemes. Note that the direction of diffraction linearly depends on the

de Broglie wavelength, and consequently, on the average speed of the beam. It is therefore possible to tune the diffraction angle acting on the average speed of the atoms, e.g. by changing the temperature of the source. Examples of interferometers using mechanical gratings are given by [53] using Sodium atoms and [54] with helium atoms. Albeit providing a valid method to manipulate atoms for interferometric purposes, mechanical gratings are unpractical for experimental implementations; e.g. the flux of atoms is reduced, since only a fraction of the atoms passes through the gratings. Furthermore, atomic beams need to propagate in hard vacuum, and correcting a nano–grating misalignment can result in cumbersome and time consuming operations. To address these difficulties, different strategies have been developed. An effective solution is to make use of optical gratings shone into the vacuum system through view ports, keeping the optomechanical elements out of vacuum.

3.1.2. Light gratings

Through light–atom interaction it is possible to produce refractive, reflective and absorbing structures for atomic beams. The simplest example stems from considering a beam of atoms modelled as a two level system crossing a far off resonance light field forming a standing wave. In this case, the atoms will experience an optical potential that is proportional to the intensity of the light, creating a transmission grating [55, 56, 57]. Specifically, in a $x - y$ plane, assuming the atomic beam propagating in the direction $\hat{\boldsymbol{x}}$ and that the light field being formed by two counter–propagating beams in the $\hat{\boldsymbol{y}}$ axis having same frequency ω, the atoms experience a potential of the form

$$U(y) \propto I_0 \cos^2 ky$$

where $k = 2\pi/\lambda = \omega/c$ (λ being the light field wavelength and c the speed of light). This is equivalent to a grating of period $d = \lambda/2$ without the disadvantage of losing atomic flux due to mechanical blocking.

3.1.3. Light–atom interactions

A third possibility is to perform beam splitters using on resonance atom–light interaction [12, 58]. A two level model of an atom having a ground state $|g\rangle$ of

energy E_g and an excited state $|e\rangle$ of energy E_e interacting with a light beam of frequency $\omega_L = (E_e - E_g)/\hbar$ undergoes oscillations between the two levels at the Rabi frequency Ω_R dependent on the intensity of the light beam. As before, consider the case of an atomic beam of speed v and momentum $p = Mv$ directed towards $\hat{\boldsymbol{x}}$, crossing a transverse light field orientated along $\hat{\boldsymbol{y}}$. Also, assume that the light beam has a finite waist w so that the atoms interact with the photons for a time $\tau = w/v$ and that the atoms are initially prepared in the ground state $|g\rangle$.

When absorbing a photon atoms in the ground state $|g\rangle$ acquire a momentum of modulus $p_L = \hbar k_L = \hbar\omega_L/c$ in the direction of the light beam and end up in the excited state $|e\rangle$. As a result after traversing the illuminated region, the atoms are found in a superposition of the states $|g, p\hat{\boldsymbol{x}}\rangle$ and $|e, p\hat{\boldsymbol{x}} + p_L\hat{\boldsymbol{y}}\rangle$ in a proportion dependent on $\Omega_R\tau$.

Two cases are of relevant importance: when $\Omega_R\tau = \pi/2 + l\pi$, $l \in \mathbb{N}$ atoms initially prepared in $|g, p\hat{\boldsymbol{x}}\rangle$ end up in an equal superposition of $|g, p\hat{\boldsymbol{x}}\rangle$ and $|e, p\hat{\boldsymbol{x}} + p_L\hat{\boldsymbol{y}}\rangle$ thus acting as a coherent beam splitter or re–combiner, referred to as a $\pi/2$–pulse; while an interaction time satisfying the condition $\Omega_R\tau = \pi + 2l\pi$, $l \in \mathbb{N}$ causes the swap between the two states, acting therefore as a mirror, called a π–pulse.

3.2. Phase difference in an atom interferometer

In this section we consider an interferometer built using light–atom interaction techniques (see Section–3.1.3) to obtain beam splitters and mirrors. The interferometric path is divided into four regions (I to IV as in figure (3.1)) separated by light–atom interaction events happening at times t_i, $i \in \{0, 1, 2\}$ with $t_1 - t_0 = t_2 - t_1 = T$.

In region I, a collimated atomic beam prepared in the ground state $|g\rangle$, is propagating with momentum $\boldsymbol{p}$. At time t_0, the atoms in the beam interact with a resonant laser beam L_1 with momentum $\boldsymbol{p}_L = \hbar\boldsymbol{k}_L$, whose waist and intensity induce a $\pi/2$–pulse transition on the atoms. This causes the atomic beam to split (in region II) into equally populated states $|g, \boldsymbol{p}\rangle$ and $|e, \boldsymbol{p}+\boldsymbol{p}_L\rangle$, following two different paths γ_a and γ_b respectively, separated by a distance $\Delta\boldsymbol{l}_I(t - t_0) = \boldsymbol{p}_L(t - t_0)/M$ linearly increasing with time.

At time t_1 a second laser beam L_2 with the same orientation and the product

waist–intensity twice as large, interacts with the two separated beams inducing a π–pulse, i.e. inverting the states and directions of the atoms in the trajectories γ_a and γ_b. Thus, the distance $\Delta \boldsymbol{l}_{II}(t-t_1) = \Delta \boldsymbol{l}_I(T) - \boldsymbol{p}_L(t-t_1)/M$ between the two trajectories in region III progressively reduces down to zero at time t_2 in which a third laser beam L_3 with the same properties as L_1 recombines the two atomic beams with a $\pi/2$–pulse.

Depending on the difference $\Delta\phi$ of the accumulated phases along the curves γ_a and γ_b, the proportion of atoms found in the state $|g, \boldsymbol{p}\rangle$ or $|e, \boldsymbol{p}+\boldsymbol{p}_L\rangle$ in region IV will vary and can be detected with opportunely placed detectors. The interferometer obtained is the equivalent of an optical Mach–Zehnder interferometer.

The phase difference $\Delta\phi(t-t_0) = -\Delta E(t-t_0)/\hbar$ accumulated in regions II and III is easily calculated looking at the energy difference $\Delta E = E_{\gamma_b} - E_{\gamma_a}$ between the two possible trajectories.

In region II, for the atoms following trajectory γ_a, the energy contributions are represented by the energy of the ground state E_g and the kinetic energy of the atoms $\boldsymbol{p}^2/2M$. While, for the trajectory γ_b, the total energy balance (atom

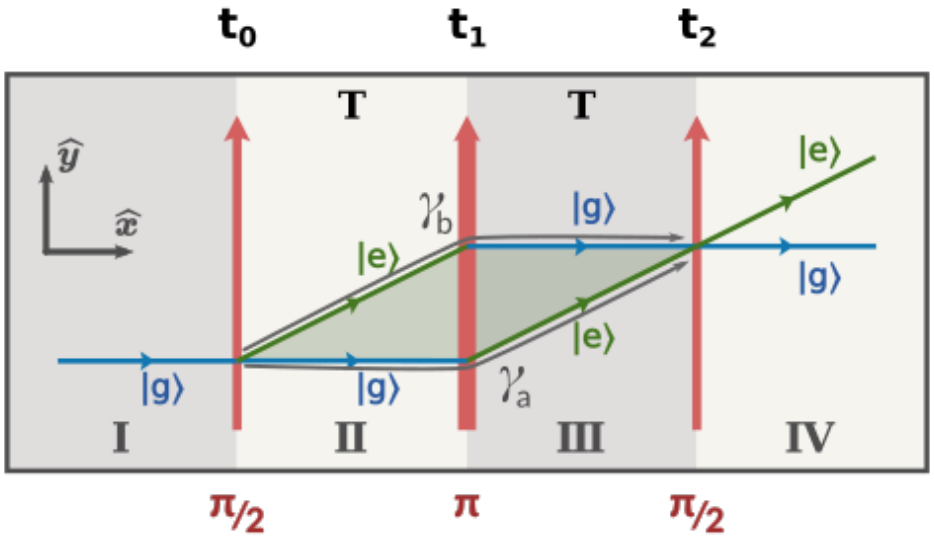


Figure 3.1.: Schematics of an atom interferometer. The atoms freely propagate in region I to IV and interact with light at times t_0, t_1 and $t_2$with π and $\pi/2$ pulses. The internal states $|g\rangle$ and $|e\rangle$, together with the possible trajectories γ_a and γ_b are indicated. With reference to the text, the initial momentum of the atoms $\vec{p}$ is assumed to be parallel to the direction $\hat{x}$, while the momentum of the light beam is directed towards $\hat{y}$.

and field) presents positive contributions of the energy of the excited state E_e and the kinetic energy $(\boldsymbol{p}+\boldsymbol{p}_L)^2/2M$ minus the energy of the absorbed photon $\hbar\omega_L$, as the number of photons is reduced by one. Thus, the energy balance in region II amounts to $\Delta E_{II} = [E_e - E_g - \hbar\omega_L + (\boldsymbol{p}+\boldsymbol{p}_L)^2/2M - \boldsymbol{p}^2/2M] = (\boldsymbol{p}+\boldsymbol{p}_L)^2/2M - \boldsymbol{p}^2/2M$ (considering the resonance condition $\hbar\omega_L = E_e - E_g$) leading to an accumulated phase difference at time $t = t_1$ of [59, 58]:

$$\Delta\phi_{II} = \Delta\phi(T) = -\frac{\boldsymbol{p}_L^2 + 2\boldsymbol{p}\cdot\boldsymbol{p}_L}{2M\hbar}T \tag{3.3}$$

For symmetry considerations it is evident that the phase difference accumulated in region III is equal and opposite in sign to $\Delta\phi_{II}$ resulting in a null accumulated phase difference at time t_2. As a result, in the absence of external effects, in region IV the same situation of region I is recovered resulting in a single atomic beam represented by $|g,\boldsymbol{p}\rangle$. Conversely, when external physical phenomena contribute differently in the two paths, the final phase difference is not negligible causing a portion of the beam to populate the channel $|e,\boldsymbol{p}+\boldsymbol{p}_L\rangle$.

By detecting the flow of atoms in the two channels it is possible to quantify the accumulated phase and therefore obtain an indirect measure of the external effect through its phase contribution. To see this, consider an interferometric sequence with an accumulated global phase $\Delta\phi_G$ and label the atoms with their internal states and the possible path $\gamma_{a(b)}$ as $|g,a(b)\rangle$ and $|e,a(b)\rangle$ in regions II and III.

The $\pi/2$–pulse transforms the internal ground state in $(|g\rangle - i|e\rangle)/\sqrt{2}$ and the excited one into $(-i|g\rangle + |e\rangle)/\sqrt{2}$, while a π–pulse causes the transformations $\pi|g\rangle \to -|e\rangle$ and $\pi|e\rangle \to -|g\rangle$.

The interferometer starts with atoms in the state $|g\rangle$ undergoing a $\pi/2$–pulse, which outputs $(|g,a\rangle - i|e,b\rangle)/\sqrt{2}$. After a π–pulse is applied and the state of interferometer can be represented as $(-|g,b\rangle + i|e,a\rangle)/\sqrt{2}$. At time t_2, the atoms following the path γ_b accumulate a global phase $\Delta\phi_G$ with respect to the other path. At this time also a $\pi/2$–pulse is applied, as a result the interferometer output is found in the state

$$|\Psi_{IV}\rangle = ie^{-\Delta\phi_G/2}\left(|g\rangle\sin\frac{\Delta\phi_G}{2} - |e\rangle\cos\frac{\Delta\phi_G}{2}\right)$$

The portion of atoms in the excited state can be found considering the modulus square of the projection $(|e\rangle\langle e|)\,|\Psi_{IV}\rangle$ of the output state $|\Psi_{IV}\rangle$ onto the excited

state $|e\rangle$, explicitly [11]

$$\mathbb{P}\left[|e\rangle\right] \equiv \frac{N_e}{N_e + N_g} = \cos^2\frac{\Delta\phi_G}{2} = \frac{1-\cos\Delta\phi_G}{2}$$

where $N_{e(g)}$ is the number of atoms in the state $|e\rangle$ ($|g\rangle$).

Suitably engineered interferometers can be used to evaluate measurables such as gravity [60, 61] and gravity gradients [62], atomic polarizability, determination of the fine structure constant [63, 64] and inertial measurements such as accelerations and rotations [46, 65].

3.3. Sagnac Atom interferometers

The scope of this thesis is to report on the construction of a rotation sensitive interferometer, i.e. a Sagnac interferometer. In the next section, a description of the Sagnac effect (following [66]) is provided.

3.3.1. Sagnac Effect

Let's consider an inertial frame where each point is expressed in cylindrical coordinates $\{x^\mu\} = (ct, r, \theta, z)$ in which a disk of radius R is rotating with a frequency Ω as pictured in Figure–3.2. Two beams counter-propagate from a source (and detector) Σ sitting on the rim of the disk. In this frame, the line element (consider $dz = 0$ for a planar disk) results

$$ds^2 = g_{\mu\nu}dx^\mu dx^\nu = c^2dt^2 - dr^2 - r^2d\theta^2$$

The coordinates $s_\Sigma = (x^0, x^1, x^2)$ of Σ in the frame of reference K, co–rotating with the disk, are $s_\Sigma = (ct, R, \theta = \Omega t)$, rewritten as $s_\Sigma = (c\theta/\Omega, R, \theta)$ when eliminating the time dependence. Similarly, the positions of the co–rotating $(+)$ and counter–rotating $(-)$ beams can be written as $s_\pm = (c\theta/\omega_\pm, R, \theta)$, with $\omega_\pm$ being their angular velocity.

The event of interest is the first contact of the co(counter)–rotating beam with the source(detector) Σ. This event takes place at the time

$$\frac{\theta_\pm}{\Omega} = \frac{\theta_\pm \pm 2\pi}{\omega_\pm}$$

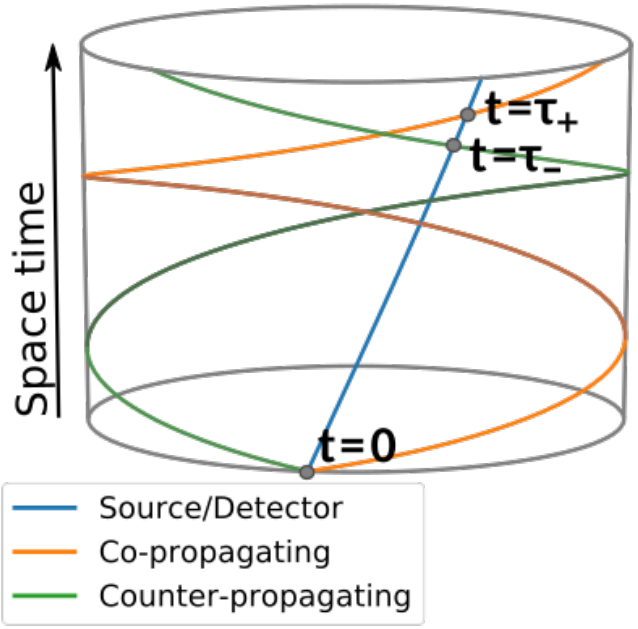


Figure 3.2.: Space time trajectories of the source-detector, and two co(counter)-propagating beams in the inertial frame. The basis of the cylinder represents the rim of the disk at time $t = 0$, when the source and the two counter-propagating beams are co-local. Then, the rim of the disk moves along the space-time direction forming a cylindrical surface and the beams travel around the disk in opposite directions, to then become co-local again with the detector at time $t = \tau_{+(-)}$.

with $\theta_\pm$ indicating the angular distance covered by Σ moving at the angular speed Ω, while $\theta_\pm \pm 2\pi$ represents the angular distance travelled by the co(counter)–rotating beam at the angular speed $\omega_\pm$. The travelled distance then solves as

$$\theta_\pm = \pm\frac{2\pi\Omega}{\omega_\pm - \Omega} = \pm\frac{2\pi\beta}{\beta_\pm - \beta}$$

indicating with $\beta = \Omega R/c$ and $\beta_\pm = \omega_\pm R/c$ the dimensionless velocities of the source and beams respectively. For a clock at rest in Σ, the proper time reads as

$$\begin{aligned}\tau &= \frac{1}{c}\int_{s_\Sigma}\sqrt{c^2dt^2 - dr^2 - r^2d\theta^2}ds_\Sigma = \int d\theta\sqrt{\left(\frac{dt}{d\theta}\right)^2 - \frac{R^2}{c^2}} \\ &= \int d\theta\sqrt{\frac{1}{\Omega^2} - \frac{R^2}{c^2}} = \frac{\sqrt{1-\beta^2}}{\Omega}\int d\theta\end{aligned}$$

Consequently, the first encounter time $\tau_\pm$ can be easily determined evaluating the integral $\int_0^{\theta_\pm} d\theta = \theta_\pm$, obtaining

$$\tau_\pm = \pm\frac{2\pi\beta}{\beta_\pm - \beta}\frac{\sqrt{1-\beta^2}}{\Omega}$$

The proper time difference is then calculated as

$$\Delta\tau = \tau_+ - \tau_- = 2\pi\beta\frac{\sqrt{1-\beta^2}}{\Omega}\frac{\beta_- + \beta_+ - 2\beta}{(\beta_- - \beta)(\beta_+ - \beta)}.$$

In a reference frame at rest with the rotating disk, the two beams move at relative velocities $\beta'_\pm = (\beta - \beta_\pm)/(1 - \beta\beta_\pm)$. As a consequence, the proper time difference can be rewritten as

$$\Delta\tau' = \frac{2\pi\beta}{\Omega\sqrt{1-\beta^2}}\left(\frac{1}{\beta'_+} + \frac{1}{\beta'_-}\right) + \frac{4\pi}{\Omega\sqrt{1-\beta^2}}\beta^2$$

Assuming that the two beams have equal velocity in opposite directions, then the first term vanishes. Furthermore assuming $\beta \ll 1$, i.e. the disk rotates at a speed much smaller than the speed of light, and indicating with λ the particles' wavelengths the resulting phase difference $\Delta\phi = 2\pi c\Delta\tau'/\lambda$ in the rotating frame gives:

$$\Delta\phi = \frac{8c\pi^2\omega}{\lambda\Omega}\beta^2 = \frac{8\pi}{\lambda c}A\Omega \tag{3.4}$$

where $A = \pi R^2$ the area of the disk. It can be shown that this formula applies to any shape of the path, so it does not restrict to the circular case. The phase difference is proportional to the area of the interferometer and to the rotation velocity of the system, generalizing to the 3D case is easily done by substituting A with $\boldsymbol{A}$ the vector area, Ω with the rotation speed vector $\boldsymbol{\Omega}$ and taking the scalar product of these two vectors.

Also, this work is focused on matter–wave interferometry. One of the striking advantages of atom interferometry w.r.t. light–based ones, comes from the gain in sensitivity. This becomes evident, in this case, comparing a light-based interferometer with a matter-wave one with atoms of mass M having de Broglie wavelength λ_{DB} and speed $v = h/M\lambda_{DB}$, in the non–relativistic regime, sharing the same geometrical properties. Comparing the phases of the two devices, i.e. evaluating the ratio between the phase differences, results in:

$$\frac{\Delta\phi_{matterwave}}{\Delta\phi_{light}} = \frac{\lambda c}{\lambda_{DB} v} = \lambda \frac{cM}{h}$$

that for light in the visible spectrum (with a wavelength $\lambda \sim 5 \times 10^{-7} m$, for green light) and Rb^{87} as atomic species used, gives approximately:

$$\frac{\Delta\phi_{matterwave}}{\Delta\phi_{light}} \approx 5 \times 10^{-7}\mathrm{m} \frac{3 \cdot 10^{8}\mathrm{m/s} \times 87 \cdot 1.6 \cdot 10^{-27}\mathrm{Kg}}{6.6 \cdot 10^{-34}\mathrm{J \cdot s}} \approx 3.5 \cdot 10^{10}.$$

Meaning that atom–based devices are ten orders of magnitude more sensitive than their light–based counterpart.However, this result can be misleading. To begin with, this comparison assumes equal geometry in the two cases. As a matter of fact, state of the art atom based interferometers enclose an area of $11\,\mathrm{cm}^2$ [47], while high performance commercial fibre optic gyroscopes present an effective area of $1\,\mathrm{km}^2 = 10^{12}\,\mathrm{cm}^2$.

Moreover, the particle detection follows Poissonian statistics, meaning that the uncertainty on the measure scales as $\Delta\phi \propto 1/\sqrt{N}$, where $N = \mathcal{F}\tau$ is the number of particles detected in a time interval τ for a beam of flux $\mathcal{F}$. Atom interferometers present low flux with respect to their optical counterpart. According to various examples illustrated in [12], atom fluxes are in the order $\mathcal{F}_{atom} \leq 10^{10}\, atoms/s$. While, the photon flux of a $1\,\mu W$ of power laser beam is in the order of $\mathcal{F}_{photon} \simeq 10^{13}\, photon/s$ for a red light source.

As a consequence, optical devices still represent the leading technology for ro-

tation sensing, enclosing an interferometric area $\sim 10^{11}$ larger than atomic ones and presenting much higher particle flux.

Nonetheless, besides being a relatively young field of research, compact matter wave Sagnac interferometers already have been shown to reach sensitivities of about $10^{-7} rad/\sqrt{s}$ for a $11\,cm^2$ interferometric area [47], with best record sensitivities on the order of $10 \times 10^{-10}\, rad/\sqrt{s}$ [65, 11], while commercial high end FOG present sensitivities of $2.9 \times 10^{-9}\, rad/\sqrt{s}$ [13] using several km of spooled optical fibres.

3.3.2. Phase of Sagnac Atom Interferometers

To explicitly evaluate the Sagnac phase accumulated in an atom interferometer it is possible to refer to Section–3.2 and account for modification due to a rotation Ω oriented counter-clockwise. As previously remarked, the final phase difference is given by the sum of the phases $\Delta\phi_{II}$ and $\Delta\phi_{III}$, having the same form of (3.3), but opposite sign with respect of each other. When a rotation is taking place, at time t_1 the light beam of momentum $\boldsymbol{p}_L$ is rotated by an amount ΩT with respect to its initial orientation at time $t_0 = 0$. Similarly, the second light beam at time t_2 is rotated by an amount ΩT with respect to its position at time t_1. Indicating with α the angle formed between the vectors $\boldsymbol{p}$ and $\boldsymbol{p}_L$ at time t_1 the phase differences $\Delta\phi_{II}$ and $\Delta\phi_{III}$ take the form

$$\Delta\phi_{II} = -\frac{|p_L|^2 + 2pp_L\cos(\alpha + \Omega T)}{2M\hbar}T$$
$$\Delta\phi_{III} = \frac{|p_L|^2 + 2pp_L\cos(\alpha - \Omega T)}{2M\hbar}T$$

that in the limit of $\Omega T \ll 1$ can be approximated as

$$\Delta\phi_{II} \approx -\frac{|p_L|^2 + 2pp_L\left[\cos(\alpha) - \sin(\alpha)\,\Omega T\right]}{2M\hbar}T$$
$$\Delta\phi_{III} \approx \frac{|p_L|^2 + 2pp_L\left[\cos(\alpha) + \sin(\alpha)\,\Omega T\right]}{2M\hbar}T,$$

resulting in a global phase difference $\Delta\phi = \Delta\phi_{II} + \Delta\phi_{III} \approx 4pp_L\sin(\alpha)\,\Omega T^2/(2M\hbar)$. Noticing that $|\boldsymbol{p} \times \boldsymbol{p}_L| = pp_L\sin(\alpha)$ and representing Ω as a vector orthogonal to

the interferometric plane:

$$\Delta\phi \approx 2\frac{(\boldsymbol{p}\times\boldsymbol{p}_L)\cdot\vec{\Omega}}{M\hbar}T^2 = 2\,(\boldsymbol{v}\times\boldsymbol{k}_L)\cdot\vec{\Omega}T^2. \tag{3.5}$$

The term $(\boldsymbol{v}\times\boldsymbol{k}_L)\,T^2$can be rewritten as $\frac{M}{\hbar}\,(T\boldsymbol{v}\times T\boldsymbol{p}_L/M)$ in which the term between parentheses can be understood as an area vector [11]

$$\boldsymbol{A} = (\boldsymbol{v}\times\boldsymbol{v}_L)\,T^2 \tag{3.6}$$

of modulus equal to the area of the interferometer and oriented in the normal direction. Expressing the pre-factor in terms of the de Broglie wavelength $M/\hbar = 2\pi/v\lambda_{DB}$ (from (3.1)), it shows that equation (3.5) coincides with equation (3.4), observing that the wave packets travel half a revolution around the closed path.

3.3.3. Time domain vs Space domain

In equation (3.6) it is evident that to increase the interferometric area (and therefore the sensitivity of the device) two strategies are readily available. The first technique is to increment the distance $d = vT$ between the splitters and mirrors; interferometers utilizing this option are sometimes referred to in the literature as space domain interferometers [11]. The possible alternative is to increment the time T leading to a quadratic increment of the area, obtaining a time domain atom interferometer, see [11]. In the first case the coherence required for the observation of interference effect is achieved utilizing atoms moving at very high speed (achieved with heated up gases, with atoms moving at average speeds in the order of Km/s or higher) ensuring that the time necessary for the atoms to propagate in the interferometer to be shorter than the coherence decay rate. Conversely, time domain interferometers require long interrogation times, it is then necessary to reduce the temperature of the atoms to reduce the coherence decay rate.

Also, the splitting Raman beams are pulsed instead of remaining in continuous wave mode. In this way, all the atoms interact with the light field for the same amount of time and consequently separate by equal amounts, allowing better control of the trajectories.

Examples of experimental implementations include free falling atoms released

from a Bose Einstein Condensate [67] and cold atomic clouds launched vertically to follow strongly parabolic trajectories [47]. Experimental realizations of time domain atom interferometers present the largest enclosed areas that, as previously mentioned, reach up to 11cm^2 [47]. In this last work, a $\pi/2 - \pi - \pi - \pi/2$ sequence is used and dead times (i.e. the time interval required for the preparation and detection of the instrument) are eliminated thanks to a "juggling" method [68, 47]. This consists in concatenated interferometric sequences in which the atom preparation of a certain run happens while the atoms of the previous run are following the parabolic trajectory. This is made possible using common $\pi/2$ pulses, i.e. the light pulse causing the splitting of the ascending atoms of the incoming run is the same pulse that causes the recombination of the descending atoms of the preceding run.

4. Guided matter–wave Sagnac interferometry

In all the schemes presented in Chapter–3, atoms freely propagate along the arms of the interferometer and the control of their trajectories is performed through deflection by means of optical pulses, mechanical or optical gratings. As a result, enclosed areas are usually quite small compared to the size of the interferometer itself, limiting its sensitivity, as seen in Section–3.4. Also, common path configurations, allowing to suppress biases due to imperfections in one of the two arms, become infeasible or, at the very least, unpractical.

Conversely, schemes in which atoms are confined on predefined potential geometries and actively moved along them by means of potential perturbations, can be built. These confining potentials can be interpreted as matter wave guides in which de Broglie wavelengths are propagated, in analogy to optical elements such as optical fibres and integrated optical circuits. For rotation sensing, ring shaped wave guides provide large enclosed areas compared to the device's size (especially considering the possibility to perform multiple round trips [49]) and allow for long interrogation times [48]. Full round trips or their multiples are easily implemented, so that counter propagating matter waves travel the same common path compensating for imperfections of the wave guide. Furthermore, the velocity of each matter wave–packet can be arbitrarily controlled, in contrast to optical wave guides (e.g. optical fibres) were propagation speed is set by the physical properties of the medium.

These arguments show how atomic wave guides represent a powerful and versatile tool towards the realization of compact and highly sensitive interferometric devices. Albeit, coherent matter wave propagation in guiding potentials turns out to be an experimentally challenging task and evidence of interferometric signal based on this technique is yet to be demonstrated [12]. This is due to multiple reasons, such as the the technical difficulty to engineer a trapping scheme working

as a matter wave guide and the prolonged mechanical coupling with the environment, causing vibrational noise to dominate the interferometric signal. A more detailed description will be provided in Section-4.3.

In this chapter it will be shown, conceptually, how Sagnac interferometry can be implemented with matter wave guides, described as atomic clocks counter propagating along closed trajectories. Also, possible candidates for experimental implementations will be discussed, pointing out the relative challenges, with specific attention for the model utilized for the experimental design of this project.

4.1. Sagnac interferometry with atomic clocks

The manifestation of the Sagnac effect in a circular matter wave guide can be described in terms of proper time differences between atomic clocks travelling at different speeds. The working principle is an analogue of the Hafele–Keating experiment, that in 1972 demonstrated that atomic clocks flown around the world in opposite directions on board commercial jet flights would measure time differences in agreement with relativity theory [69].

Two atomic clocks are confined in a circular guide of radius R. Initially located in the same position, the two clocks start moving in opposite directions along the wave guide until they recombine on the final position, different from the initial one. This defines two distinct events, i.e. an initial splitting event $\mathbb{E}_S$ and a final recombining event $\mathbb{E}_R$, in any frame of reference.

According to an observer sitting on the laboratory frame L, the two clocks move with equal angular speed $w^{(L)}$ in opposite directions. While, according to an observer, placed on an inertial frame of reference I, the frame L is rotating with an angular speed $\Omega_S \neq 0$ (see Figure–4.1) and the two clocks are moving at different angular speeds $w_{\pm}^{(I)}$. In the notation used, $w_{-}^{(I)}$ is the angular speed of the clock moving clockwise, while $w_{+}^{(I)}$ indicates the angular speed of the clock moving counter–clockwise.

For the inertial reference frame I, the time elapsed between the two events $\mathbb{E}_S$ and $\mathbb{E}_R$ amounts to $\Delta t_I = T_f - T_0$. Defining $w = \pi/\Delta t_I$, the speed of each of the two clocks can then be written as $w_{\pm}^{(I)} = w \pm \Omega_S$ in the frame I.

From the perspective of each of the clocks, $\mathbb{E}_S$ and $\mathbb{E}_R$ are co–local events. Therefore, the proper time $\Delta t_{clock}^{\pm}$ of each of the two clocks can be obtained according

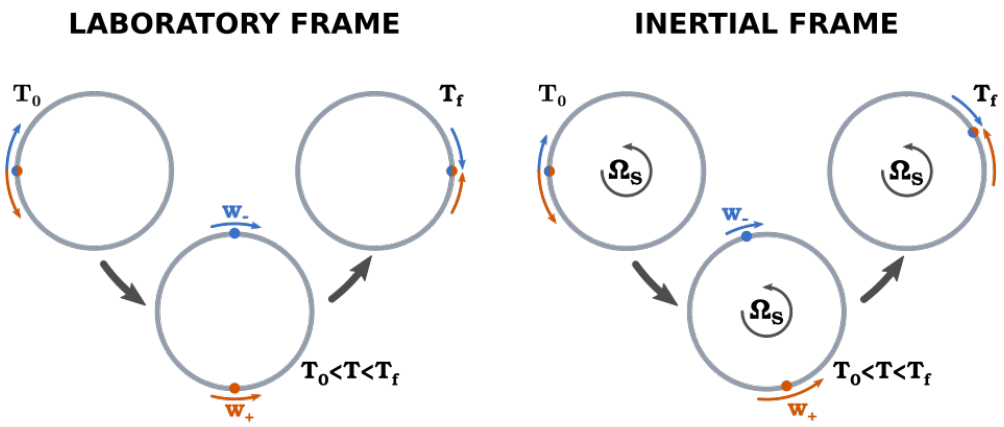


Figure 4.1.: Trajectories of the clocks as seen as the laboratory frame (on the left) and as seen from an inertial reference frame (on the right). With the atomic clock co-moving with the inertial frame is represented in orange, while the counter-moving one is coloured in blue. In the laboratory frame the clocks are perceived move symmetrically ($|w_+| = |w_-|$). While, from the perspective of an inertial frame, due the additional angular speed Ω_S of the laboratory frame, the clocks move with different speeds.

to the time dilation relation

$$\Delta t^{\pm}_{clock} = \Delta t_I \alpha(\beta_\pm)$$

where $\alpha(\beta) = (1-\beta^2)^{1/2}$ is the reciprocal of the Lorentz factor $\gamma(\beta) = 1/\alpha(\beta)$ and the ratio between the tangential speed of each of the clocks and speed of light c is indicated as $\beta_\pm = w^{(I)}_\pm R/c$.

Defining the dimensionless speeds $\beta_w = wR/c$ and $\beta_{\Omega_S} = \Omega_S R/c$, the Taylor expansion of factor $\alpha(\beta_\pm)$ in the limit $\beta_w \ll \beta_{\Omega_S}$ reads as

$$\alpha\left(\beta_w \pm \beta_{\Omega_S}\right) = \alpha\left(\beta_w\right) \pm \alpha'\left(\beta_w\right)\beta_{\Omega_S} + \frac{1}{2}\alpha''\left(\beta_w\right)\beta^2_{\Omega_S} + O\left(\beta_{\Omega_S}\right)^3 \tag{4.1}$$

When considering the proper time difference between the clocks $\Delta T_{f,clock} = \Delta t^-_{clock} - \Delta t^+_{clock}$, all the terms in (4.1) cancel out except for the term linear in β_{Ω_S}. Observing that $\alpha'(\beta) = -\beta\gamma(\beta)$, the proper time difference in the non

relativistic limit $\beta_w \ll 1$, using $T_0 = 0$, explicitly reads as

$$\Delta T_{f,clock} = \Delta t_I \left(\alpha(\beta_-) - \alpha(\beta_+)\right) \simeq -2T_f \alpha'\left(\beta_w\right) \beta_{\Omega_S} \tag{4.2}$$

$$= 2T_f \gamma\left(\beta_w\right) \beta_w \beta_{\Omega_S} \overset{\beta_w \ll 1}{\simeq} \frac{2\pi \Omega_S R^2}{c^2} \tag{4.3}$$

$$= \frac{2\Omega_S A}{c^2} \tag{4.4}$$

where the area enclosed by the wave guide is $A = \pi R^2$. Considering the Compton frequency $\omega_C = Mc^2/\hbar$ of an atom of rest mass M, the phase difference between the two clocks will be given by

$$\begin{aligned} \phi &= \omega_C \Delta T_p + T_f \Delta\omega_c \\ &= \underbrace{2\frac{M}{\hbar} A\Omega_S}_{S} + \underbrace{T_f \frac{\Delta E}{\hbar}}_{C}. \end{aligned} \tag{4.5}$$

Here the term S corresponds to the phase difference due to the Sagnac phase, while the term C accounts for internal energy differences $\Delta E = \hbar\Delta\omega_c$ between the two clocks in case the atoms are in different energetic configurations. When the energy difference ΔE and the interrogation time T_f are known with high accuracy, the phase difference due to the Sagnac phase can be simply obtained as $\phi_S = \phi - T_f \Delta E/\hbar = 2MA\Omega_S/\hbar$.

An interesting case to consider is when an observer in L is able to independently control the rate at which the two clocks move around the ring.

In fact, if the laboratory operator can move the atomic clocks such that their angular speed equals w in the inertial frame I, the resulting proper time difference between the clocks becomes null. Thus simulating the situation in which $\Omega_S = 0$.

Considering the two clocks based on the same atomic transition, i.e having the same Compton frequency, the phase read by the interferometer depends only on the area of the interferometer A and the angular speed Ω_S. The remaining pre–factor depends only on constants that are known with high accuracy from literature. Thus the uncertainty on the phase reads as

$$\Delta\phi \propto \Omega_S \Delta A + A\Delta\Omega_S$$

indicating with $\Delta\Omega_S$ and ΔA the uncertainties on the angular speed and on the interferometric area, respectively. Having $\Omega_S \approx 0$ means that the component

of the phase error due to area uncertainty becomes negligible, improving the accuracy of the interferometer. This result is not achievable with fibre optical Sagnac interferometers as described in Section–3.3.1. Indeed, for the optical case, the beam splitter and detector moves with the laboratory frame, defining the sequence in three co–local events instead of two. Hence, the only way of obtaining this effect on a fibre optical gyroscope is placing it on a rate table counteracting the rotation of the laboratory, such that the recombining events between the two photons and the beam splitter are simultaneous.

4.1.1. Interferometric protocol

The dressed state potential scheme presented in Section–4.2 is used by Navez and collaborators in [48] and Fernholz and his collaborators as described in [51] to build a circular atomic wave guide in which the atomic clouds can be state dependently steered in a controlled fashion. Meaning that the position of atoms with positive g_F–factors can be controlled arbitrarily as well as for atoms with negative g_F–factors and these positions can be controlled independently one from each other.

The approach followed by Navez consists in the following. Starting from a magnetic quadrupole trap the potential landscape is radio frequency dressed into a spherical shell. For gravity the atoms accumulate in the lower part of the shell. An oscillating field in the vertical direction is then used to modulate the direction of the quantization axis, causing the potential minima to coincide with the equator of the resonant shell. This technique was first derived by Lesanovsky and Klitzing in 2007 [70] and experimentally demonstrated by C. Foot in 2009 [71]. While the technique developed by Fernholz and collaborators, the working principle at the basis of this work, consists in perturbing a static magnetic ring quadrupole with a magnetic field oscillating in the radio frequency regime and it will be described with further detail in Section–4.2.1.

This calls for an atomic clock Sagnac interferometric scheme as described in Figure- 4.2 nella pagina seguente. Indicating atomic states with positive(negative) Landè factor as $|\uparrow\rangle(|\downarrow\rangle)$, this interferometric protocol can be described as follows [50]:

a) Initially the atoms are prepared in the state $|\uparrow\rangle$ and accumulated in one part of the ring trap. Successively, using a $\pi/2$-pulse the cloud is

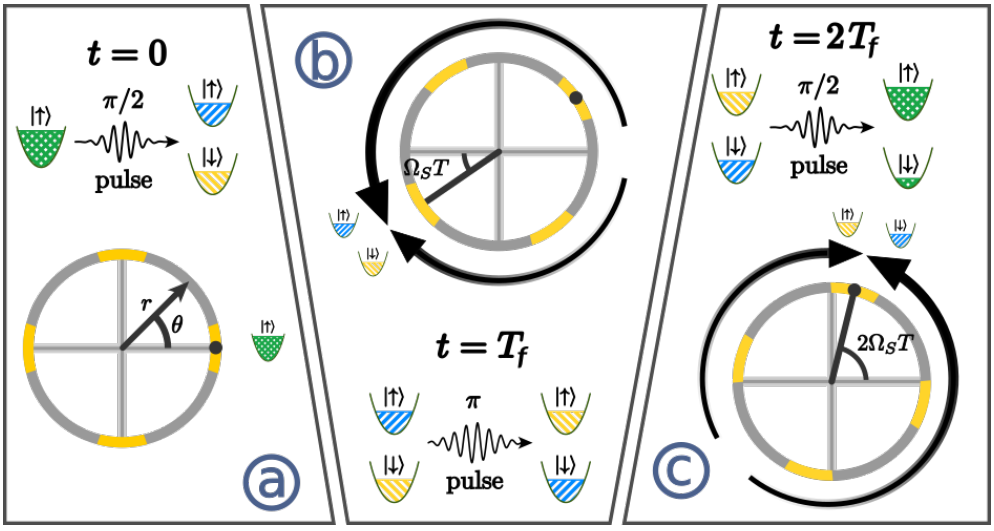


Figure 4.2.: Interferometric protocol: The ring represents the ring trap, with the grey and yellow sections highlighting the rotation of the laboratory frame with respect to the inertial frame (described by the orthogonal axes inscribed in the ring). The black circle marks the position of the atoms at time $t = 0$, while the black arrows show the motion of the two clouds. The angular position of the atoms at time $t = T_f$ and $t = 2T_f$ is also indicated in b) and c). The black arrow in a) indicates the radius of the ring trap r and θ the angular coordinate.

split into a superposition $|\Psi_a\rangle = (|\uparrow\rangle + |\downarrow\rangle)/\sqrt{2}$ of the two states $|\uparrow\rangle$ and $|\downarrow\rangle$.

b) The two states experience different trapping potentials that make them counter-propagate around the ring. After a time $t = T_f$ the two clouds recombine at the other end of the ring and a π-pulse swaps the population of the states.

c) The atoms are then driven for another time interval $\Delta t = T_f$ at the end of which we get a second recombination of the two clouds at the original location where a final $\pi/2$-pulse can be used to convert the accumulated Sagnac phase into a population imbalance.

Notice that a protocol ending in b) applying a $\pi/2$-pulse instead of a π-pulse followed by a readout procedure, would coincide with the interferometer discussed in (4.1) (see Figure-4.2, a and b). The phase measured by the interferometer at this stage is the sum of the Sagnac and the Compton frequency difference. The $\pi/2$-pulse would convert the total accumulated phase into a detectable population imbalance; therefore knowing with precision the value of Compton contribution

$\phi_C = T_f \Delta E/\hbar$ would allow an estimation of the Sagnac phase. Not shining any pulse in b) would lead to an interferometric signal in the same way. Nonetheless, the complete sequence provides valuable advantages [50]:

1. The atoms spend an equal amount of time T_f in each state. As a consequence, the global phase accumulated at time $t = t_0 + 2T_f$ would read $\phi|_{t=2T} \approx T_f \Delta E/\hbar + \omega_C \Delta T_f - T_f \Delta E/\hbar + \omega_C \Delta T_f = 2\omega_C \Delta T_f$, cancelling out the components due to differences of energy in the two different states.
2. The trajectories of the two wave-packets follow the same path in opposite directions, cancelling out phase differences due to time independent imperfections of the trapping potential[1].
3. The process can be repeated for multiple revolutions increasing the effective area of the interferometer.

4.1.2. Interferometric signal

Referring to the Section– 4.1.1 a pagina 26, the protocol, up to the point (b) can be formally described by the operator

$$\hat{V}^{\alpha} = \hat{U}^{\alpha}_{\pi/2} \hat{U}^{D}(T_f) \hat{U}^{0}_{\pi/2} \tag{4.6}$$

where $\hat{U}^{\alpha}_{\pi/2}$ indicates a $\pi/2$–pulse operator with a controlled phase α, while $\hat{U}^{D}(T_f)$ indicates the evolution operator of the Hamiltonian describing the driving of the states for a time interval T_f. The phase α in the last pulse introduces a controllable phase in the readout of the interferometric signal. This allows operations of calibrations of offsets and scanning of the phase for data interpolation purposes. The protocol for a full revolution is simply obtained applying the operator $\hat{W}^{\alpha} = \hat{V}^{\alpha} \hat{V}^{0}$.

A quantum-mechanical model can be built to analyse this atom Sagnac interferometer architecture, as illustrated in [50] and [72].

The relativistic nature of the quantum mechanical treatment of the Sagnac effect is a debated topic. The Schrödinger equation is often presented to be invariant w.r.t Galilean transformations, but theoretical derivations of non Galilean

[1] Time dependent perturbations of the trapping potential will still affect the measure, but they can be ruled out with repeated experiments or utilizing multiple sensors.

invariant effects are possible [73], as shown for the Sagnac effect in Section4.5[2]. Some authors argue that the Schrödinger equation is actually not invariant under Galilean boosts, but can approximate relativistic behaviours up to the first order in v/c [74]. Albeit these effects usually result in overall phases that do not add meaningful insight in the quantum behaviour of the system (hence the apparent Galilean invariance), they produce measurable effects for spatially separated wave functions [74], as for the case of the Sagnac effect.

Consider a particle in a circular wave guide of radius R in which atoms are trapped along the tangential direction θ with an harmonic potential:

$$V(\boldsymbol{x}) = \frac{1}{2} m\omega^2 \left|\boldsymbol{x} - \boldsymbol{x}_0(t)\right|^2$$

where $\boldsymbol{x} = (x, y) \in \mathbb{R}^2$ is the position of the particle, m it's mass, $= (x, y) \in \mathbb{R}^2$ the rest position of the harmonic oscillator and ω the trapping frequency of the potential. In polar coordinates the term $|\boldsymbol{x} - \boldsymbol{x}_0(t)|^2$, with Θ being the angular coordinate of $\boldsymbol{x}_0$, reads as

$$\left|\boldsymbol{x} - \boldsymbol{x}_0(t)\right|^2 = 2R^2 \left[1 - \cos\left(\theta - \Theta\left(t\right)\right)\right],$$

which using the approximation $\cos x = 1 - x^2/2 + O(x^4)$, $x \ll 1$ for small angles $\theta - \Theta(t) \ll 1$ leads to the potential:

$$V\left(\theta, \Theta\left(t\right)\right) = \frac{1}{2} m\omega^2 R^2 \left(\theta - \Theta\left(t\right)\right)^2$$

In polar coordinates the differential operator reads as $\nabla^2 = \partial_r^2 + 1/r^2 \partial_\theta^2 = 1/R^2 \partial_\theta^2$ since the radius of the wave guide is constant, making the Hamiltonian of the system read as

$$H = -\frac{\hbar}{2mR^2} \partial_\theta^2 + \frac{1}{2} \omega^2 m R^2 \left(\theta - \Theta\left(t\right)\right)^2. \tag{4.7}$$

For the considered interferometer, the particles present two internal states, e.g. $|g\rangle$ and $|e\rangle$, whose position can be independently controlled.

The Hamiltonian (4.7) holds for each internal state independently, assuming no interaction between the two internal states, resulting in two uncoupled equations. As a consequence, in the following all the equations are referring to a single internal state $|l\rangle$ and the relevant quantities labelled with a subscript l where l

[2]This incongruence of theoretical interpretations lead some authors to explicitly distinguish the *quantum Sagnac effect* from the Sagnac effect.

can be either g or e. Then this Hamiltonian modifies as follows

$$H = -\frac{\hbar}{2mR^2}\partial_\theta^2 + \frac{1}{2}\omega^2 mR^2 \left[\sum_{l\in\{g,e\}} (\theta - \Theta_l(t))\,|l\rangle\langle l|\right]^2 \tag{4.8}$$

To simplify the Hamiltonian, it is useful to consider a spin dependent rotating frame, assuming that the two internal states $|g\rangle$ and $|e\rangle$ are steered in opposite directions. This is achieved using the rotation transformation

$$U = e^{\Theta(t)\partial_\theta}$$

transforming the operator $\hat{O}$ as $\hat{O} \to \hat{O}' = U\hat{O}U^\dagger$, where $(\partial_\theta)^\dagger = -\partial_\theta$. Explicit calculations lead to an effective Hamiltonian

$$H_{eff} = -\frac{\hbar}{2mR^2}\partial_\theta^2 + \frac{1}{2}\omega^2 mR^2\theta^2 + i\hbar\sum_{l\in\{g,e\}} \dot{\Theta}_l\,|l\rangle\langle l|\,\partial_\theta$$

The operators θ and ∂_θ can be written in terms of annihilation $\hat{a}$ and creation $\hat{a}^\dagger$ operators as

$$\theta = \left(\hat{a}^\dagger + \hat{a}\right)\sqrt{\frac{\hbar}{2m\omega R^2}}$$
$$\partial_\theta = \left(\hat{a} - \hat{a}^\dagger\right)\sqrt{\frac{mR^2\omega}{2\hbar}},$$

which substituted back in (4.8), returns the Hamiltonian of the system in second quantization formalism:

$$H = \hbar\omega\left(\hat{a}^\dagger\hat{a} + \frac{1}{2}\right) + i\sum_{l\in\{g,e\}} |l\rangle\langle l|\,\dot{\Theta}_l(t)\sqrt{\frac{\hbar m\omega R^2}{2}}\left(\hat{a} - \hat{a}^\dagger\right)$$

The function $\dot{\Theta}_l(t)$ represents the angular speed at which the atoms are moving around the ring shaped wave guide, which is the sum of two contributions: the angular speed at which the whole system is rotating Ω_S with respect to the inertial frame and the velocity profile $w_l(t)$ of the state dependent trap centres with respect to the lab frame. With this in mind, the angular speed then can be expressed as $\dot{\Theta}_l(t) = \Omega_S + w_l(t)$.

For simplicity, assume the velocity profiles of the interferometer to be symmetric

with respect to the rotating frame, i.e. $w_e(t) = -w_g(t) = w(t)\,\forall t$. In this way it is possible to write the dimensionless Hamiltonian $\mathcal{H} = H/\hbar\omega$ as [50]

$$\mathcal{H} = \hat{a}^\dagger \hat{a} + \frac{1}{2} + \frac{i\tilde{R}}{\sqrt{2}} \left(\tilde{\Omega}_S + \sum_{l\in\{g,e\}} \tilde{w}_l(\tau) \left|l\right\rangle \left\langle l\right| \right) \left(\hat{a} - \hat{a}^\dagger\right) \tag{4.9}$$

where $\tilde{\Omega}_S = \Omega_S/\omega$ is the relative rate speed of the laboratory, $\tilde{w}_l(t) = w_l/\omega$ is the rational rate profile of the state $|l\rangle$, $\tau = \omega t$ the time unit and $\tilde{R} = \sqrt{m\omega R^2/\hbar}$ is a dimensionless radius.

The evolution operator $\hat{U}_l^D$ for the Hamiltonian $\mathcal{H}_l = \mathcal{H}\left|l\right\rangle\left\langle l\right|$ (4.9) can be written in terms of the eigenvalue $\alpha_l(\tau)$ of the coherent state[3] $|\alpha_l(\tau)\rangle$ and the phase accumulated $\phi_l(\tau)$, explicitly [72]

$$\begin{aligned}
\alpha_l(\tau) &= \frac{\tilde{R}}{\sqrt{2}} \left(i\tilde{\Omega}_S + e^{-i\tau} \int_0^\tau \tilde{w}_l(t) e^{it} dt \right) \\
\phi_l(\tau) &= \tilde{R}^2 \tilde{\Omega}_S \left(\int_0^\tau dt \int_0^t \tilde{w}(s) \sin(s-t)\, ds \right).
\end{aligned}$$

Substituting the Magnus expansion [75], of the operator

$$\hat{U}_l^D(\tau) = e^{\alpha_l(\tau)\hat{a}^\dagger - \alpha_l^\star(\tau)\hat{a}} e^{-i\hat{a}^\dagger\hat{a}\tau} e^{i(\phi_l(t) - \tau/2)} \tag{4.10}$$

into (4.6) returns the operator describing the interferometric protocol. In other words, the operator $\hat{U}_l^D(\tau)$ in (4.10) describes the dynamics of the atoms in the harmonic trap, which centre is moved along the wave guide at a rate described by the velocity profile $\tilde{w}_l(t)$; to complete the evolution operator describing the entire interferometric protocol, it is necessary to consider the $\pi/2$–pulse operators ($\hat{U}^0_{\pi/2}$ and $\hat{U}^\alpha_{\pi/2}$) at the beginning and at the end of the sequence acting as beam splitter and re–combiner respectively. For instance, considering atoms prepared in an initial state $|i\rangle = |g\rangle \otimes |0\rangle$, where $|0\rangle$ indicates the ground state of the harmonic oscillator, the final state ρ_f is obtained using

$$\rho_f = \hat{V}^\alpha \left|i\right\rangle \left\langle i\right| \left(\hat{V}^\alpha\right)^\dagger$$

where the evolution operator $\hat{V}^\alpha$ explicitly reads as $\hat{V}^\alpha = \hat{U}^\alpha_{\pi/2}(\hat{U}^D_g \otimes \hat{U}^D_e)\hat{U}^\alpha_{\pi/2}$,according to(4.6), with the dynamics evolution operator $\hat{U}_l^D,\ l = g, e$ described in

[3] Satisfying the equation $\hat{a}|\alpha_l(\tau)\rangle = \alpha_l(\tau)\,|\alpha_l(\tau)\rangle$.

equation (4.10).The signal of the interferometer is then given through estimation of the population imbalance, given by the Pauli operator $\hat{\sigma}_z = |g\rangle\langle e| - |e\rangle\langle g|$, explicitly [72]

$$\langle \sigma_z \rangle = -e^{-2\pi\omega^2 |\mathcal{F}[\tilde{w}](\omega)|^2} \cos\left(\phi_S \left(1 - \sqrt{\frac{2}{\pi}}\mathcal{F}\left[\tilde{w}(\omega)\right]\right) + \alpha\right)$$

where the operator $\mathcal{F}[\cdot]$ returns the Fourier transform of its argument. Two parts can be identified in this formula: the first part is $C = \exp(-2\pi\omega^2|\mathcal{F}[\tilde{w}]|^2)$ that corresponds to the amplitude of the signal, often referred to as interferometric contrast. The second part shows the Sagnac phase dependent term that allows access to the rotation rate Ω_S of the entire system.

It is evident from this formula that the shape of the velocity profile has a strong impact on both the contrast and the phase of the interferometric signal. This is manifest from the explicit dependency on the velocity profile's Fourier transform in both of the two terms, meaning that the choice of the velocity profile is crucial in the design of the interferometric sequence. To ensure that the terms depending in the Fourier transform do not dominate, it is necessary that the velocity profiles does not contain harmonic components in oscillating at the trapping frequency.

In case the initial state is thermal, i.e. for a non–zero temperature T case, the signal of the interferometer modifies, presenting an overall temperature dependent factor. In other words, only the contrast of the interferometer is affected. Using the results of [50], the interferometric signal for an initial thermal state reads as

$$\langle \sigma_z \rangle = -e^{-2\pi\omega^2 |\mathcal{F}[\tilde{w}](\omega)|^2 \left(1+\frac{k_B T}{\omega\hbar}\right)} \cos\left(\phi_S \left(1 - \sqrt{\frac{2}{\pi}}\mathcal{F}\left[\tilde{w}(\omega)\right]\right) + \alpha\right)$$

As for the previous result, the contrast of the interferometer strongly depends on the velocity profile of $w(t)$.

4.2. Dressed potentials

When studying an atom interacting with an oscillating electromagnetic field, it is convenient to represent the system in terms of the so–called dressed state picture [76]. In other words, considering the total energetic balance of the system

composed of the atom and a photon as the energetic structure of the atom itself, i.e. an atom dressed with a photon.

Practically, this leads to simplify a time dependent Hamiltonian to a time independent one with non-zero coupling terms between different internal states of the dressed atom whose strength depends on the amplitude of the interacting field. Hence, a two level atom with energy separation $E = \hbar\omega_0$ interacting with a light field of energy $\hbar\omega$ can be seen as a two level atom with energy separation $\Delta = \hbar(\omega - \omega_0) \ll \min\{\hbar\omega, \hbar\omega_0\}$ and non-zero coupling between the ground and excited state [77].

In the following, the dressed atom picture is used to describe the interaction of a neutral atom with a magnetic field composed of two parts, one of which is time-independent and the other one is oscillating at radio frequency regimes.

The behaviour of a neutral atom having magnetic momentum $\boldsymbol{\mu} = \mu_B g_F \hat{\boldsymbol{F}}$, in the presence of a time dependent magnetic field $\boldsymbol{B}(t)$ can be approximated (see Appendix–A.3) by the following Hamiltonian:

$$H = \mu_B g_F \hat{\boldsymbol{F}} \cdot \boldsymbol{B}(t) \tag{4.11}$$

where μ_B is the Bohr magneton, g_F the gyromagnetic Landé factor and $\hat{\boldsymbol{F}} = (\hat{F}_x, \hat{F}_y, \hat{F}_z)$ is the spin vector operator.

The magnetic field $\boldsymbol{B}(t)$ is the sum of a static term $\boldsymbol{B}_0$ and a second time-dependent term $\boldsymbol{B}_{TD}(t) = \mathrm{Re}\{\boldsymbol{B}_{TD} e^{-i\omega t}\}$ oscillating at a frequency ω, so that the total magnetic field reads as $\boldsymbol{B}(t) = \boldsymbol{B}_0 + \mathrm{Re}\{\boldsymbol{B}_{TD} e^{-i\omega t}\}$. Without loss of generality, the quantization axis $\hat{\boldsymbol{z}}$ is chosen to be parallel with the static field, i.e. $\boldsymbol{B}_0 = (0, 0, B_0)$.

Given the symmetry of the problem it is convenient to express the Hamiltonian H in the spherical coordinates $\hat{\boldsymbol{e}}_\pm = (\hat{\boldsymbol{x}} \pm \mathrm{i}\hat{\boldsymbol{y}})/\sqrt{2}$, $\hat{\boldsymbol{e}}_\pi = \hat{\boldsymbol{z}}$. Hence, the spin vectors are expressed in terms of the raising and lowering operators $\hat{F}_\pm = \hat{F}_x \pm i\hat{F}_y$ and similarly, the oscillating field can then be written in terms of the spherical polarization vectors as $\boldsymbol{B}_{TD} = B_+ \hat{\boldsymbol{e}}_+ + B_- \hat{\boldsymbol{e}}_- + B_\pi \hat{\boldsymbol{e}}_z$. Consequently, the Hamiltonian (4.11) can be re–written as

$$H = \mu_B g_F \frac{1}{2} \left[\left(\frac{\hat{F}_+ B_+ + \hat{F}_- B_-}{\sqrt{2}} + \hat{F}_z B_z \right) e^{-i\omega t} + \hat{F}_z B_0 \right] + \text{c.c.}$$

Rotating frame To simplify the Hamiltonian a frame rotating at angular rate $\pm\omega$ around the $\hat{\boldsymbol{z}}$ axis is considered, where the sign accounts for the sense of rotation. This is achieved through the rotation operator $\hat{U} = e^{\pm i\omega\hat{F}_z t}$. The state of the system $|\psi\rangle$ can be seen as the rotation of the state $|\psi'\rangle$ at rest in the rotating frame, according to the relation $|\psi'\rangle = \hat{U}|\psi\rangle$. The Schrödinger equation in the rotating frame then reads as

$$\begin{aligned} i\hbar\partial_t|\psi\rangle &= H|\psi\rangle \\ i\hbar\partial_t\left(\hat{U}^{-1}|\psi'\rangle\right) &= H\hat{U}^{-1}|\psi'\rangle \\ \pm\hbar\omega\hat{F}_z\hat{U}^{-1}|\psi'\rangle + i\hbar\hat{U}^{-1}\partial_t|\psi'\rangle &= H\hat{U}^{-1}|\psi'\rangle \\ i\hbar\hat{U}^{-1}\partial_t|\psi'\rangle &= H\hat{U}^{-1}|\psi'\rangle \mp \hbar\omega\hat{F}_z\hat{U}^{-1}|\psi'\rangle \end{aligned} \tag{4.12}$$

Multiplying both members of the equation (4.12) by $\hat{U}$ results

$$\begin{aligned} i\hbar\partial_t|\psi'\rangle &= \hat{U}H\hat{U}^{-1}|\psi'\rangle \mp \hbar\omega\hat{F}_z|\psi'\rangle \\ i\hbar\partial_t|\psi'\rangle &= \left(\hat{U}H\hat{U}^{-1} \mp \hbar\omega\hat{F}_z\right)|\psi'\rangle, \end{aligned}$$

using $[\hat{U}, \hat{F}_z] = 0$. This corresponds to a system ruled by a new Hamiltonian

$$\begin{aligned} H_R &= \hat{U}H\hat{U}^{-1} - \hbar\omega\hat{F}_z \\ &= \mu_B g_F \frac{1}{2}\left[\left(\frac{\hat{U}\hat{F}_+\hat{U}^{-1}B_+ + \hat{U}\hat{F}_-\hat{U}^{-1}B_-}{\sqrt{2}} + \hat{F}_z B_z\right)e^{-i\omega t} + (B_0 \mp \frac{\hbar\omega}{\mu_B g_f})\hat{F}_z\right] + \text{c.c.} \end{aligned}$$

describing the physics of the system as perceived in the rotating frame. Using the relation $e^{\alpha\hat{F}_z}\hat{F}_\pm e^{-\alpha\hat{F}_z} = e^{\pm\alpha}\hat{F}_\pm$, this can be written explicitly as:

$$H_R = \frac{g_F\mu_B}{2}\left[\left(B_0 \mp \frac{\hbar\omega}{g_F\mu_B}\right)\hat{F}_0 + B_+\hat{F}_+e^{i(\omega\mp\omega)t} + B_-\hat{F}_-e^{-i(\omega\pm\omega)t} + B_\pi e^{\mp i\omega t}\right] + \text{cc} \tag{4.13}$$

Depending on the orientation of the frame rotation, different terms become time independent. According to the dressed state picture, the orientation of rotation is selected depending on the sign of the Landé factor g_F such that the condition $g_F\mu_B B_0 \mp \hbar\omega \ll \min\{\omega_0, g_F\mu_B B_0\}$ holds. Consequently, for positive (negative) g_F the term in $B_{+(-)}\hat{F}_{+(-)}$ becomes time independent. By mean of the rotating wave approximation, i.e. neglecting terms oscillating at frequency $\omega \gg 1$, it is

possible to neglect the oscillating terms simplifying H_R as

$$H_R = \mu_B g_F \frac{1}{2}\left[\frac{B_+}{\sqrt{2}}\hat{F}_+ + \left(B_0 - \frac{\hbar\omega}{\mu_B g_f}\right)\hat{F}_z\right] + \text{c.c.},$$

whence diagonalization leads to the eigenenergies [78, 51, 48] :

$$E^{\pm}_{m_F} = m_F g_F \mu_B \sqrt{\left(B_0 - \left|\frac{\hbar\omega}{g_F\mu_B}\right|\right)^2 + \frac{|B_\pm|^2}{2}} \tag{4.14}$$

where the component $B_{+(-)}$ is selected for positive (negative) g_F–factors.

In equation (4.14) two aspects emerge: first only one of the $B_\pm$ components of the time-dependent field plays a role in the eigenvalues and second the energy minimum is moved from a zero field region to a non-zero one where losses due to spin flip (also referred as Majorana spin flip [79]) transitions are suppressed [51, 70]. For this second aspect to be true, the eigenvalues in 4.14 need to be non degenerate, hence it is required that the $B_\pm$ never vanishes on the resonant condition. This is achieved by opportunely choosing the geometry of $\boldsymbol{B}_{TD}$.

4.2.1. Dressed quadrupole ring

In two dimensions a static magnetic quadrupole field can be used to confine atoms (for states in which the product $m_F g_F$ is positive) at a specific point. Extending the trap in a third dimension by revolution on an in plane axis distant R_0 from the quadrupole centre, results in a ring trap as illustrated in Figure-4.3.

Albeit assessing the problem of confining atoms in a closed loop, the trap minimum is a line of zero-field leading to atom losses due to Majorana spin flip [79].

For the ring geometry discussed above this results in transforming the minimum from a zero field loop to a non-zero field toroidal surface with major radius R_0 and minor radius set by the resonance condition $r = \hbar\omega/(g_q g_F \mu_B)$, where g_q indicates the gradient of the quadrupole magnetic field [51]. The direction of the static field $\boldsymbol{B}_{DC}$ in the vicinity of the zero field is given by the unit vector $\hat{\boldsymbol{e}}_0 = (-\cos\theta\cos\phi, -\sin\theta\cos\phi, \sin\phi)$, its normal plane can be described by an arbitrary basis of two unit vectors orthogonal to $\hat{\boldsymbol{e}}_0$. For simplicity, the tangential to the ring $\hat{\boldsymbol{e}}_1 = (-\sin\theta, \cos\theta, 0)$ and the vector $\hat{\boldsymbol{e}}_2 = \hat{\boldsymbol{e}}_0 \times \hat{\boldsymbol{e}}_1 = -(\cos\theta\sin\phi, \sin\theta\sin\phi, \cos\phi)$ can be considered. It is then possible to write the

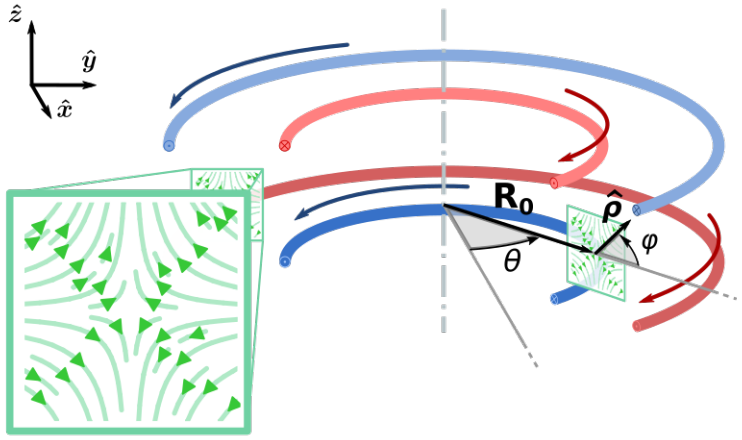


Figure 4.3.: A planar quadrupole field (green inset) is generated with four current carrying wires, by rotation around an axis distant R_0 from the quadrupole centre, a quadrupole ring is formed. The blue and red rings illustrate the wires carrying a current in anticlockwise and clockwise direction as indicated by the blue and red arrows generating the desired field geometry. The Cartesian coordinates are indicated together with $\boldsymbol{\rho}$ the distance from the zero-field ring, ϕ the poloidal angle, the radial direction $\boldsymbol{r}$ is parallel to the vector $\boldsymbol{R}_0$ and the toroidal coordinate θ.

spherical coordinate vectors

$$\hat{\boldsymbol{e}}_{\pm} = \frac{\hat{\boldsymbol{e}}_1 \pm i\hat{\boldsymbol{e}}_2}{\sqrt{2}} = \frac{1}{\sqrt{2}} \begin{pmatrix} -\sin\theta \mp i\cos\theta\sin\phi \\ \cos\theta \mp i\sin\theta\sin\phi \\ \mp i\cos\phi \end{pmatrix}.$$

The oscillating field coupling components $B_{\pm}$ in equation (4.14), due to the presence of an arbitrary dressing field $\boldsymbol{B}_{RF}$ oscillating at frequency ω, can then be simply calculated taking the projection $B_{\pm} = \hat{\boldsymbol{e}}_{\pm} \cdot \boldsymbol{B}_{RF}$ [51].

Two fields oscillating at a frequency ω are used to dress the static quadrupole ring.

The first one, $\boldsymbol{B}_{TD}^{(t)}$, is elliptically polarized on the plane section of the ring quadrupole field. It is labelled as a toroidal (t) field, as it reshapes the region of energy minimum from a uni–dimensional ring to a toroidal surface. This field is required to be non linearly polarized, thus it always contains a component oriented radially in the plane of the ring quadrupole. This can be generated by two coils positioned above and below the ring, running oscillating currents with different phases.

The second field $\boldsymbol{B}_{TD}^{(p)}$ (namely in–plane field, labelled with (p)) lies in the same plane of the quadrupole ring, being free to oscillate in any direction on this plane. For instance this can be produced by two pairs of coils whose axis direction coincides with $\hat{\boldsymbol{x}}$ and $\hat{\boldsymbol{y}}$. The total oscillating field is then given by $\boldsymbol{B}_{TD} = \boldsymbol{B}_{TD}^{(t)} + \boldsymbol{B}_{TD}^{(p)}$ resulting in a total coupling strength of $B_{\pm} = \hat{\boldsymbol{e}}_{\pm} \cdot \boldsymbol{B}_{RF} = B_{\pm}^{(t)} + B_{\pm}^{(p)}$.

The radial field $\boldsymbol{B}_{TD}^{(t)}$ can be expressed as

$$\boldsymbol{B}_{TD}^{(t)} = \frac{a}{\sqrt{2}} \begin{pmatrix} \cos\theta \\ \sin\theta \\ i \end{pmatrix} + \frac{b}{\sqrt{2}} \begin{pmatrix} \cos\theta \\ \sin\theta \\ -i \end{pmatrix}$$

where $a, b \in \mathbb{C}$ indicate the amplitudes of opposite circular components of the field. The relative coupling strength is then calculated as

$$B_{\pm}^{(t)} = \hat{\boldsymbol{e}}_{\pm} \cdot \boldsymbol{B}_{TD}^{(t)} = \frac{1}{2}\left(\mp a e^{-i\phi} \pm b e^{i\phi}\right). \tag{4.15}$$

Its modulus can be written as $|B_{\pm}^{(t)}| = 1/2 \times \sqrt{|a|^2 + |b|^2 - 2|a||b|\cos(2(\phi - \phi_{ab}))}$ where $\phi_{ab} = \phi_a - \phi_b$ and the components of the radial field are written as $a =$

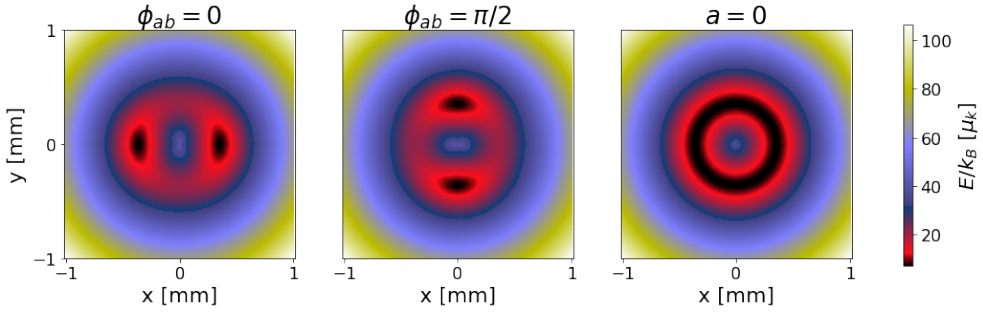


Figure 4.4.: Colour map in the $\hat{\rho}, \hat{z}$-plane section of the potential dressing by the effect of $\boldsymbol{B}_{TD}^{(t)}$ (see text): in case of elliptical polarization, with $\phi_{ab} = 0, \pi/2$; and pure circular polarization, for a null. This is obtained for a sample quadrupole with a 30G/cm gradient, $a = 0.5$ G (when $a \neq 0$) and $b = 0.3$ G.

$|a|e^{i\phi_a}$ and $b = |b|e^{i\phi_b}$.

It is evident that $|B_+^{(t)}| = |B_-^{(t)}|$, meaning that any trappable state will see the same potential, independently from the sign of the Landé factor. On the resonant surface $B_0 = \hbar\omega/g_F\mu_B$, corresponding to a toroidal surface in this case, the potential is directly proportional to the modulus $|B_\pm^{(t)}|$. In this condition it is possible to appreciate some interesting cases (see Figure–4.4 and reference [51]):

1. When a or b is negligible then the potential becomes independent of the poloidal coordinate ϕ, hence the atoms are uniformly trapped on the toroidal surface.
2. When $|a| = |b|$ there is a region, specifically when $\phi = \phi_{ab}/2 + k\pi$, $k \in \mathbb{Z}$, in which the potential becomes exactly zero. In this region the eigenenergies of (4.14) are degenerate and can lead to atom losses due to Majorana spin flip.
3. For arbitrary a and b, with the only condition $|a| \neq |b|$, two poloidal minima are formed in $\phi = \phi_{ab}/2 + k\pi$, $k \in \mathbb{Z}$. The position of the minima is dependent on the phase occurring between the amplitudes a and b.

The in–plane field $\boldsymbol{B}_{TD}^{(p)}$ can be written as

$$\boldsymbol{B}_{TD}^{(p)} = \frac{u}{\sqrt{2}} \begin{pmatrix} 1 \\ i \\ 0 \end{pmatrix} + \frac{v}{\sqrt{2}} \begin{pmatrix} 1 \\ -i \\ 0 \end{pmatrix}$$

where, similarly to the previous field, u and v are two complex numbers rep-

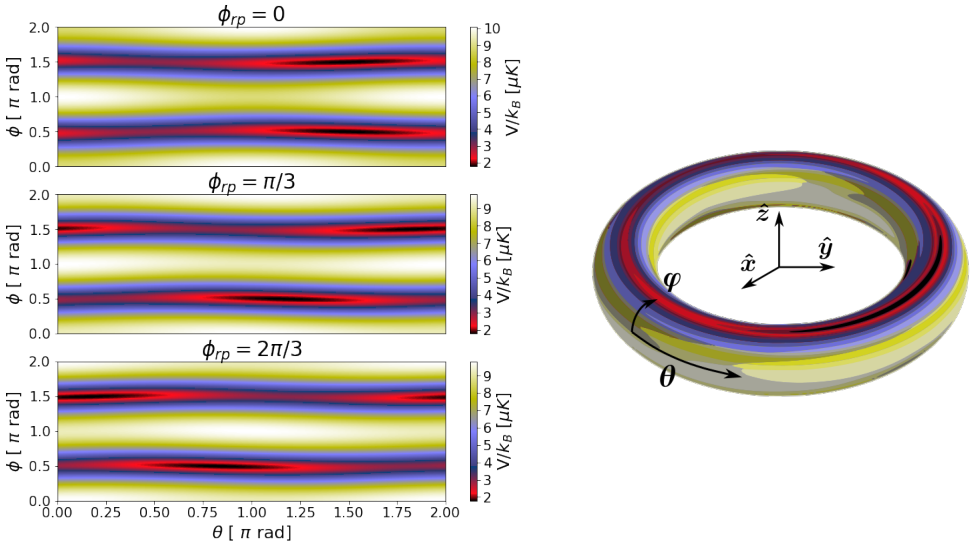
resenting the right and left handed circularly polarized component of the field respectively. Again, the coupling strengths for this field is given by the projection on the spherical coordinate unit vectors as

$$B_{\pm}^{(p)} = \hat{\boldsymbol{e}}_{\pm} \cdot \boldsymbol{B}_{TD}^{(p)} = \frac{i}{2}\left[u\left(1 \pm \sin\phi\right) e^{i\theta} - v\left(1 \mp \sin\phi\right) e^{-i\theta}\right]. \tag{4.16}$$

To easily understand the effect of this term, let us restrict to the case in which the poloidal confinement results in two equal ring minima at the top and bottom of the toroidal surface (i.e. $\phi_{ab} = \pi$ and $\phi = \pm\pi/2$)

$$B_{\pm}^{(p)}\Big|_{\phi=\pi/2} = \frac{i}{2}\left[u\left(1 \pm 1\right) e^{i\theta} - v\left(1 \mp 1\right) e^{-i\theta}\right]$$
$$B_{\pm}^{(p)}\Big|_{\phi=-\pi/2} = \frac{i}{2}\left[u\left(1 \mp 1\right) e^{i\theta} - v\left(1 \pm 1\right) e^{-i\theta}\right]$$

depending on the sign of g_F, the u and v components of the $\boldsymbol{B}_{TD}^{(p)}$ field will



(a) Position of the trap for different phases ϕ_{rp}. (b) 3D representation of the potential landscape with description of the coordinates.

Figure 4.5.: Toroidal confinement on the resonant surface (for which $B_0 = r g_q = \hbar\omega/g_F\mu_B$), with $a = 0.5$ G, $b = 0.3$ G and $|u| = |v| = 0.05\,a$. For (a) on the left: 2D representation of the potential for different relative phases ϕ_{pt} between the circular components of $\boldsymbol{B}_{TD}^{(p)}$ and $\boldsymbol{B}_{TD}^{(t)}$. In (b) on the right: 3D representation explains the coordinate system, minor and major radius of the toroidal surface are set arbitrarily.

exclusively couple at the top ($\phi = \pi/2$) or at the bottom ($\phi = -\pi/2$) of the torus. In the region in which the coupling takes place, this field component will interfere constructively or destructively with $\boldsymbol{B}_{TD}^{(t)}$ depending on the toroidal position and the relative phase between these two fields. This results in maxima and minima along the toroidal direction θ. Changing the phase $\phi_{uv} = \arg(u) - \arg(v)$ of the circular components of $\boldsymbol{B}_{TD}^{(p)}$ with respect to the phases ϕ_a and ϕ_b changes the position of the minima as shown in Figure-4.5.

The rotation sense also depends on the sign of the Landé factor, allowing for a high degree of control that can make the atomic clock scheme feasible. For instance, choosing linear polarization for $\boldsymbol{B}_{TD}^{(p)}$ and changing its phase linearly with time with respect to $\boldsymbol{B}_{TD}^{(t)}$ (i.e. oscillating at a slightly different frequency) results in driving atoms around the loop in opposite directions for opposite g_F-factors in one of the two rings and in an equal but reversed way on the other one, corresponding to the situation depicted in Figure–4.1. Moreover, an arbitrary elliptical polarization of $\boldsymbol{B}_{TD}^{(p)}$ results in moving the two state dependent traps independently one from each other, obtaining full control on their position on the poloidal coordinate θ.

4.3. About the experimental realization of guided matter wave interferometers

From the previous sections of this chapter, valuable characteristics of the presented guided atom interferometers emerge. One of the key features is to present easier calibration and re-adjustment compared to free space matter wave interferometers providing full control over the operation parameters (as the speed of the wave packets or even on the differential speeds of counter-propagating matter waves) with minimal effort. This makes operations such as the introduction of virtual rotations to operate the sensor in its most sensitive region (see Section–4.1) possible and easily implementable.

Having the atoms confined during the entire interferometric sequence, allows, at least on first principles, to operate the device in any desired orientation in the three-dimensional space under effect of gravity.

Moreover, this type of atom interferometer allows to increase the effective area of the interferometer (and therefore its sensitivity) by simply increasing the number

of revolutions travelled by the atoms around the wave guide.

On the other face of the medal, this category of atomic devices present quite hard problems to overcome.

To begin with, the task of building matter wave guides is already a challenging one as it requires the engineering of potential landscapes tight enough to maintain the trajectories of atoms in collective motion confined and smooth enough to allow the transit of the atoms without exciting undesired transverse motions.

The confinement of neutral atoms is usually performed making use of the interaction between atoms and magnetic field produced by wires running an electric current. A wire carrying a certain current produces strong magnetic fields in its proximity, but presents unavoidable corrugations due to the imperfections of the conducting material and thermal effects as the Johnson–Nyquist noise [80, 81]. At large distances, these microscopic effects average out, producing smooth potential landscapes, but the current required to produce the same field amplitude increases linearly with the distance from the wire and the creation of non trivial trapping geometries becomes cumbersome.

Assuming that a smooth and tight matter wave guide is already present in the laboratory setup, the more prolonged coupling time with the environment (compared to free trajectories of the other matter wave interferometers) introduces stronger environmental noise, that dominates the interferometric signal.

4.3.1. Alternative experimental schemes

The project reported in this thesis aims to build a guided matter wave Sagnac interferometer using the radio frequency scheme illustrated in Section–4.2.1. Nonetheless, other possible approaches are present in the literature aiming to the realization of guided matter wave interferometers. In the following I am going to briefly present two other possible experimental implementations representing valuable experimental approaches to the realization of a wave guide based atom interferometers: time averaged adiabatic potentials (TAAPs) and painted potentials.

Time averaged adiabatic potentials (TAAPs) Similarly to the technique explained in Section–4.2.1, TAAPs are based on the radio frequency dressing of a static magnetic trap. Initially proposed by Lesanovsky and von Klitzing [70],

it was first used by Heathcote et al. in [71] to experimentally demonstrate ring shaped wave guides for neutral atoms, and later by Navez and collaborators in [48] with a deeper focus on interferometric applications.

The atoms are initially trapped in a quadrupole field aligned with its axis of symmetry aligned along the vertical direction. The resulting trap is then dressed (following the theory explained in Section–4.2) using a time dependent magnetic field oscillating at a radio frequency ω, elliptically polarized in a plane containing the axis of symmetry of the quadrupole, causing the minimum of the trap to expand into a spherical surface. Because of gravity, the atoms populate the bottom half of this spherical shell into a bowl shaped confining potential. By shaking the trap along the vertical direction, i.e. modulating the static quadrupole along its axis of symmetry with a uniform magnetic field oscillating at a frequency $\omega_M \ll \omega$, the atoms are accumulated in the equator of the spherical surface. Hence, obtaining a circular wave guide. Tilting the modulating field in the polarization plane of the dressing can be used to accumulate atoms in one side of the wave guide. Changing the ellipticity of the dressing field can also be used to accumulate atoms in a specific region of the wave guide, but in this case the effect is state dependent for states with opposite Landé factors, as explained previously in Section–4.2. Thus, by a coordinated change of the polarization of the dressing field and tilting of the modulating field, it is possible to state dependently control the steering of atomic clouds around the wave guide.

This approach solves the problem of realizing smooth wave guides by placing the coils far away from the "science area" such imperfections of the confining potential due to microscopic or thermal effects in the conductors average out. Also, since higher frequencies ω of the dressing field produce larger spheres and, therefore, larger rings.

On the other hand, placing the coils outside the vacuum chamber results in bulky apparatus, not suitable for portable devices. It also needs higher currents to run in the conductors providing the oscillating fields, making the use of hazardous electrical equipment to drive the required current.

Painted Potentials: For a two level atom, an oscillating field produces a dipole potential. In case the field is oscillating at a frequency ω such that its detuning $\delta = \omega - \omega_0$ w.r.t. the resonant frequency ω_0 is much larger than the transition line-width Γ and its intensity being such that $|\delta| \gg \Omega$ (the Rabi frequency) then

the atom is subject to a potential $U \simeq \hbar\frac{\Omega^2}{4\delta}$. For positive (blue) detuning the potential is repulsive while for negative (red) detuning the potential is attractive. Also, the potential is dependent on the intensity of the oscillating field, since the square of the Rabi frequency can be written as $\Omega^2 = \Gamma^2 I/(2I_{sat})$ with I being the beam intensity and I_{sat} the saturation intensity of the gas [77]. Hence, a laser beam with a Gaussian intensity profile highly red (blue)–detuned with respect to the atomic resonance ω_0, shined on a cold atomic cloud will produce a local minima (maxima) in the potential with the same Gaussian profile. Furthermore, tightly focused red–detuned beams will provide trapping confinement in all the three directions, since the radiation intensity decreases both on the propagation axis and radial direction moving away from the focus region.

Using two beams orthogonal one to each other, it is possible to "paint" any desired potential in two dimensions [82, 49]. Pre–cooled atoms are loaded in a dipole trap, produced with a laser beam with a highly imbalanced Gaussian profile (examples from literature record section ratios of 1:40 between the vertical and horizontal waists [83]). Thus, trapping atoms in a flat surface that can be seen as a sheet.

A second red–detuned beam presenting an isotropic Gaussian profile with much tighter beam waist is shined across the light sheet. This second beam produces a further depression in the planar trapping potential. Scanning rapidly this dot across the surface it is possible, in principle, to "paint" any 2D time–averaged potential shape. The scanning is usually obtained using a bi–dimensional AOD (Acousto–Optical–Deflector, i.e. a set of two anisotropic crystals placed orthogonally one to each other that are vibrating by means of a piezoelectric transducer controlled by a function generator), allowing to deflect the laser beam in the two dimensions orthogonal to the propagation direction of the laser beam.

Experimentally, painted potentials have proven to be very versatile, allowing to paint various potential shapes and controlling the depth of the painted traces, and to modify them dynamically in time [83, 49]. Recently, this technique has been utilized to produce smooth ring potentials with a diameter of $140\mu m$ [83]. The trapped atoms, initially accumulated on one side of the ring, where allowed to expand in the uniform ring–shaped wave guide and imaged at different times. The coherent expansion of the condensate in the wave guide was expected to produce interference fringes on the opposite side of the ring. Although, the simulated fringes size were below the resolution of the optical imaging system and could not be detected in situ. Nonetheless, fringes due to phonon excitations where

imaged after releasing the atoms from the trap.

This technique represents a very versatile and well controllable way of producing matter wave guides, allowing a plethora of possible experiments in the same experimental setup without the necessity of changing a single component.

However, due to the necessary high intensity required for the "sheet" optical trap, tightly focused beams are required and usually only small wave guides can be produced. Moreover, since it is based on spatial fringes, high definition imaging necessary to image the interference patterns. In opposition to schemes like the use of state dependent techniques such as TAAPs or the one presented in this thesis, where no imaging system is required other than a lens collecting light into a photo diode.

4.3.2. Challenges of this specific implementation

To advance towards the realization of the guided matter wave interferometer previously described in this chapter, many steps need to be taken and many practical and fundamental challenges need to be overcome.

To begin with, there is the selection of the atomic species to work with, as this dictates the design of all the experimental equipment, from the laser setup to the gradients required. For the simplicity of the internal structure, common to all of the alkali elements, the availability of commercial lasers at the right wavelength and for acquired expertise within the experimental group (allowing for instance to share or exchange optical elements for the correct wavelength among different experimental projects), the element chosen for this specific project is the^{87}Rb isotope of rubidium. Further details about this isotope will be provided in the next Chapter. For the purpose of this section, it is only necessary to keep in mind that this project works on the electronic ground state of ^{87}Rb, which presents two hyperfine sub-levels of total angular momentum $F = 1$ and $F = 2$. The states of interest for this project are the $|F = 1, m_F = -1\rangle$ and $|F = 2, m_F = 1\rangle$ presenting Landé factors $g_F \simeq -1/2$ and $g_F \simeq 1/2$ respectively.

Accordingly to the atomic species, the design of the optical system required for the cooling, state preparation and imaging of the desired states requires lasers and optical elements optimized to work with wavelengths centred on $780.2\,nm$. The devices generating the magnetic fields necessary for the implementation of the scheme presented in Section–4.2.1, i.e. the atom chip set, needs to be designed and

Item	Designed	Manufactured or purchased	Equipped
Optical and laser setup	PART.	PART.	NO
Magnetic fields: coils	YES	YES	NO
Magnetic fields: micro-fabrication	YES	NO	NO
Magnetic fields: intermediate layer	NO	NO	NO
Vacuum setup	YES	PART.	NO
Control of the experiment: hardware	PART.	PART.	NO
Control of the experiment: software	YES	PART.	NO
Safety system	PART.	NO	NO
Rate table	NO	NO	NO

Table 4.1.: List of experimental equipment with record of the status at the beginning of the year 2015. The columns indicate if the item has been designed, manufactured or its components purchased and equipped in the experimental setup. The entries "YES", "NO" and "PART." indicate if the specific task has been fully completed, not started, or partially completed respectively.

manufactured, as well as the macroscopic coils used for the initial accumulation and cooling of atoms to be confined in the magnetic trap. A suitable structure, allowing to transfer the atoms from the initial macroscopic trap (formed by the external coils) to the atom chip needs to be designed and manufactured. A vacuum system allowing enough feed through electrical connections to operate the atom chip and other devices such as the dispensers of atoms, pumps and pressure probes, needs to be designed and assembled.

On top of this, the electronics necessary to stabilize the frequency of the laser, control the currents running in the coils and atom chip and other devices such as optical frequency shifters and beam shutters also need to be built. Since the aim of this sensor is to measure rotations, also a rate table capable of rotating the experimental apparatus with high accuracy, in order to imprint known speed rates to be measured and compensate for external rotations such as the rotation of the Earth, needs to be built. A computing hardware–software system allowing to control the behaviour of the electrical equipment and ultimately of the experimental setup needs to be designed. And finally all of the setup needs to be safe for the operators and for the equipment.

Milestone	Theoretically understood	Experimentally demonstrated
Magneto optical trap	YES	NO
Magnetic trap	YES	NO
Quadrupole ring trap	YES	NO
Poloidal control	YES	NO
State dependent toroidal control	YES	NO
Splitting/recombining operations	NO	NO
Read out scheme	NO	NO
Interferometric sequence	PART.	NO
Mechanical vibrational noise	NO	NO
Enhance toroidal confinement	NO	NO
Overlap of the toroidal surfaces	NO	NO

Table 4.2.: List of milestones to be achieved with record of the status at the beginning of the year 2015. The columns indicate if the task or problem has been theoretically understood or solved and if it had experimental demonstration. The entries "YES", "NO" and "PART." indicate if the specific task has been fully completed, not started, or partially completed respectively.

Some of the steps described have been discussed in the doctoral thesis of Thomas Bishop [84] with whom I collaborated to built the experimental setup. Here, the relevant results will be summarized in Section–5.5 and the description of new items not discussed in Bishop's thesis will be added. A list, summarizing the equipment required and its status of finalization at the beginning of the year 2015 is illustrated in Figure–4.6 and summarized in Table–4.1.

Besides the design and building of the experimental setup, there are some more experimental and fundamental challenges to be tackled for the realization of the interferometer and to foresee possible upgrades of performances.

It is necessary to design an experimental procedure to transfer atoms from an initial magnetic trap formed by the external coils into the chip.

It is also necessary to define an experimental technique to excite the transition $|F = 1, m_F = -1\rangle \leftrightarrow |F = 2, m_F = 1\rangle$, i.e. to be able to drive π and $\pi/2$ pulses for the interferometric protocol of Section–4.1.1, as well as a technique to read

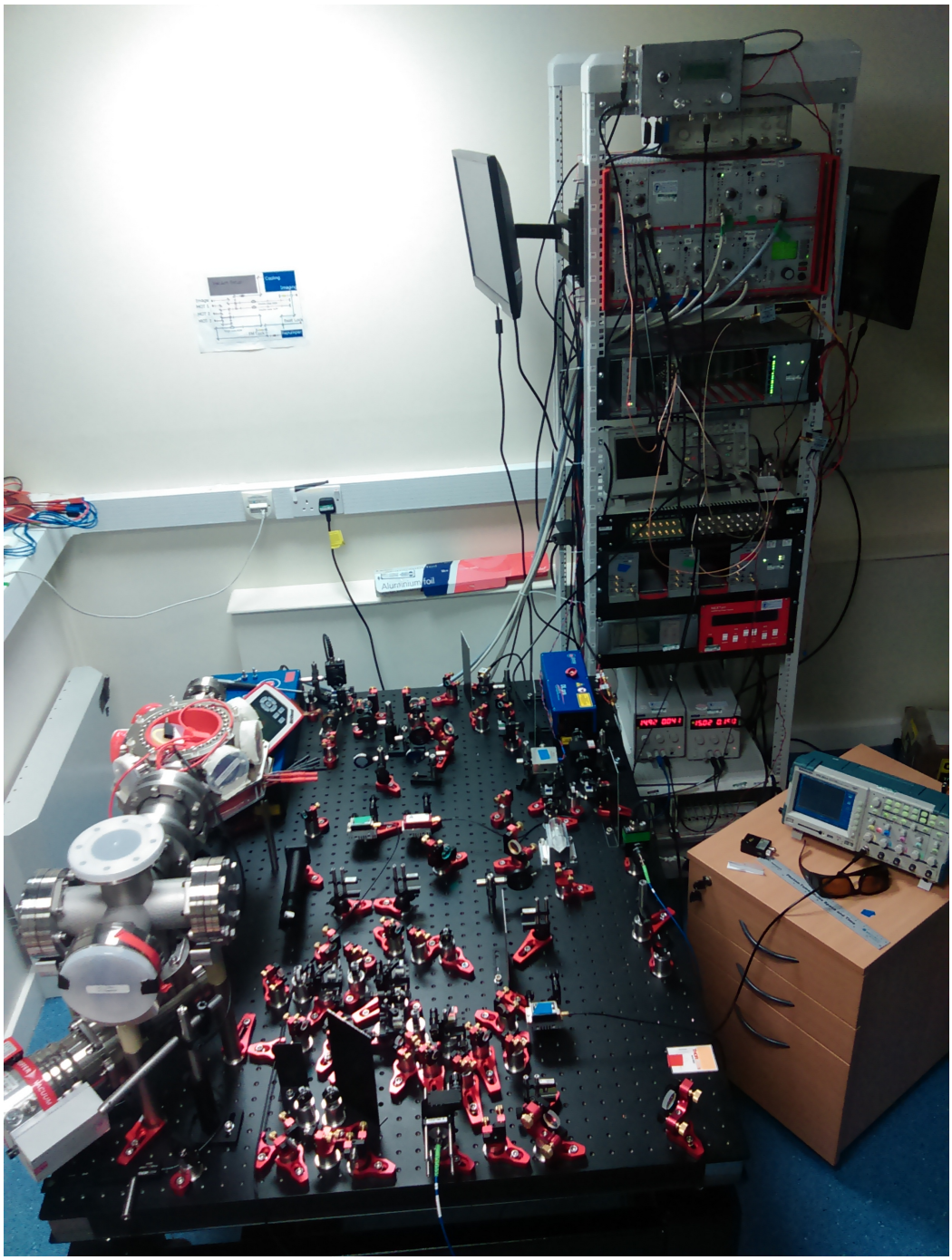
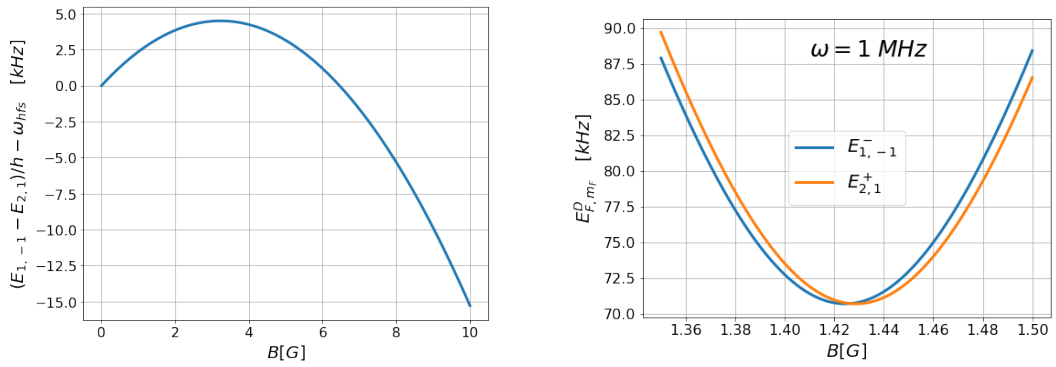


Figure 4.6.: State of the laboratory in January 2015. It can be seen the optical table presenting the lasers, partially aligned optics and on the left the vacuum chamber partially mounted and one rack presenting some power supplies, the laser control units, the computer controlling the experiment and other electronics.



(a) Difference of Zeeman splittings between $|F = 1, m_F = -1\rangle$ and $|F = 2, m_F = 1\rangle$.

(b) Minima of the dressed potential $E^{-}_{1,-1}$ and $E^{+}_{2,1}$ for the states $|F = 1, m_F = -1\rangle$ and $|F = 2, m_F = 1\rangle$ respectively.

Figure 4.7.: On the left the difference of the Zeeman splitting in the states of interest calculated as a function of the magnetic field. On the right, the consequent effects on the dressed potential, for a dressing field oscillating at $\omega = 1\,MHz$.

out the interferometric signal, i.e. to measure the population imbalance at the end of the sequence. In Section–(6.2) it will be made use of the results in [85, 86] to address the transition between the states of interest for this project. This will be used to experimentally demonstrate a three pulse Ramsey sequence, formally equivalent to the interferometric protocol illustrated in 4.1.1.

The result in equation (4.14) is valid under the assumption that (4.11) holds. That is, assuming that the energy scales linearly with the magnetic field amplitude. As shown in Figure–5.1b in the next chapter this is approximately true for low fields, but careful observation shows that the energy difference between the $|F = 1, m_F = -1\rangle$ and $|F = 2, m_F = 1\rangle$ is not constant, see Figure–4.7a showing the difference of the two levels referenced on the hyperfine spitting. This causes the radial minimum in the toroidal section not to be the same for both of the states of rubidium, see Figure–4.7b. In other words, the toroidal surfaces representing the topological minima of the potential landscape for the two different states is not coincident. As a consequence, when performing splitting and recombining operations such as π and $\pi/2$ pulses, atoms initially sitting in the minima of the potential landscape will suddenly be found in regions of non minimum potential, leading to kinetic excitations that can affect or destroy the interferometric signal.

The toroidal confinement of the traps in the scheme in Section–4.2.1 decreases linearly with the major radius of the torus. Hence, achieving large interferometric

areas would be limited by the low confinement in the toroidal direction.

In Chapter–7 it will be shown how multi-poles can be used in the radio frequency dressed trapping scheme to increase the number of minima formed around the ring and consequently increase the confinement along the angular direction θ. Also, a design generating multi-pole magnetic fields using planar wire structures will be presented. In Table–4.2 a list of milestones and challenges needed for the operation of the interferometer and their status of completion in January 2015 is presented.

5. Experimental apparatus

The aim of this thesis is to report on the experimental realization of a guided matter wave Sagnac interferometer of the type described in Section–4.2.1, i.e. using a radio–frequency dressing technique on a static ring quadrupole trap. In this chapter, the experimental setup to achieve this goal is described.

First of all, the atomic species used in this experiment is discussed. The apparatus is designed to work with the 87–isotope of Rubidium, of which the atomic structure is described in the next section. Then follows the description of the electromagnetic structures designed and manufactured for the manipulation of atoms as described in Section–4.2.1 to work with rubidium atoms.

Once the core element of the experiment is described, an overall layout of the lab with all the necessary equipment and its interconnections will be provided, followed by the description of each part of the equipment. This includes the optics required for the initial cooling of the atoms, together with the vacuum chamber, general purpose electronics for the control of the experiment and a high precision rate table that will be used to imprint rotations to be measured on the system.

5.1. Rubidium Structure

As previously mentioned, the experiment is designed to be used with Rubidium atoms, which is the element of period 5 of the first group of the periodic table, presenting atomic number $Z = 37$. Specifically, its unstable isotope having atomic mass $A = 87$, indicated as ^{87}Rb, is used.

As for all the alkali atoms, rubidium (Rb) presents a single electron on the outer shell, which gives it a very simple structure that can be derived analogously to the one of Hydrogen. As it will be evident later on, its total angular momentum possess integer spin, thus giving it bosonic properties widely used in atomic physics as, for instance, the production of Bose–Einstein condensates (BEC).

L	0	1	2	3	> 3
δ_L	3.13	2.64	1.35	0.016	~ 0

Table 5.1.: List of values of the quantum defect parameter, δ_L, for different angular momentum quantum numbers L in Rb atoms.

For ease of reading, only purely descriptive elements of the structure of ^{87}Rb will be provided in this section. Further detail and discussion is provided in Appendix–A.

5.1.1. Coarse structure

The electronic configuration of Rb is $1s^2 2s^2 2p^6 3s^2 3p^6 3d^{10} 4s^2 4p^6 5s$, where the notation $n(L)^{n_e}$ has been used; indicating with $n \in \mathbb{N}$ the principal quantum number of the level, with $L = 0, \ldots, n-1$ the orbital quantum number (using $(L) = s$ for $L = 0$, $(L) = p$ for $L = 1$, $(L) = d$ for $L = 2$) and n_e as the number of electrons occupying the level. The energy of the level can be easily determined by a modified version of the Bohr formula as [77]

$$E_{n,L} = -\frac{hcR}{(n - \delta_L)^2} \tag{5.1}$$

where h is the Planck constant, c the speed of light and R the Rydberg constant. The correcting factor δ_L depending on the orbital quantum number is usually referred to as the quantum defect and accounts for electron–electron interactions in multi-electron atoms. Its experimentally measured levels for Rb are listed in Table–5.1 [77, 87]. The same formula appears sometimes in literature using an effective principal quantum number $n^\star = n - \delta_L$ in place of its explicit form.

This energy level scheme is usually referred to as the coarse structure. For the purpose of this experimental setup the interest is focused on the $E_{n=5,L=0}/h = -940.8\,THz$ and $E_{n=5,L=1}/h = -590.7\,THz$ levels. The energy difference between these two levels lies in the near infra-red spectrum and, as it will be explained in the following section, transition between their fine sub-levels can be excited using commercially available lasers.

5.1.2. Fine structure

When considering the coupling between intrinsic spin and the orbital angular momentum of an electron, the energy levels of the coarse structure split into different sub–levels, creating a finer level scheme usually referred to as the fine structure. The amount of the spin orbit contribution can be written as [88, 89, 77]

$$\Delta E_{S-O} \propto \frac{\hbar^2}{2}\left(J(J+1) - L(L+1) - S(S+1)\right)$$

where L and $S = 1/2$ are the quantum numbers proportional to the eigenvalues of the orbital angular momentum $\hat{\boldsymbol{L}}$ and spin angular momentum $\hat{\boldsymbol{S}}$, while $J \in [|L-S|, L+S]$ is the quantum number relative to total angular momentum $\hat{\boldsymbol{J}} = \hat{\boldsymbol{L}} + \hat{\boldsymbol{S}}$.

For the levels of interest for this setup ($E_{n=5,L=0}$ and $E_{n=5,L=1}$), the fine structure contributions amount to zero for the $E_{n=5,L=0}$ level since $J = S$ and $L = 0$; while the $E_{n=5,L=1}$ level splits into two non degenerate sub–levels. This last one can indeed present two different values for the total angular momentum quantum number: $J = L - S = 1/2$ and $J = L + S = 3/2$ for which the spin–orbit contribution takes values $\Delta E_{S-O} \propto -\hbar^2$ and $\Delta E_{S-O} \propto \hbar^2/2$ respectively.

For the fine structure scheme, levels are usually expressed in spectroscopic notation $n^{(2S+1)}[L]_J$, where $[L]$ is defined in the same way as the electronic configuration notation using capital letters instead of lower case letters. With this notation, the levels of interest are expressed as $5^2S_{1/2}$, $5^2P_{1/2}$ and $5^2P_{3/2}$. The transition $5^2S_{1/2} \rightarrow 5^2P_{1/2}$ is usually referred to as D_1 line and it is addressed with electromagnetic radiation of wavelength $\lambda_{D_1} \simeq 794.979\,nm$, while the transition $5^2S_{1/2} \rightarrow 5^2P_{3/2}$ defines the D_2 line at $\lambda_{D_2} \simeq 780.241\,nm$ [89].

5.1.3. Hyperfine structure

When considering the spin of the nucleus, further splitting of the energetic levels due to the interaction between the total spin–orbit angular momentum of the electron and the spin of the nucleus needs to be taken into consideration, resulting in further splitting of the energetic levels, commonly referred as the Hyperfine structure.

Indicating with $\hat{\boldsymbol{I}}$ the nuclear spin operator with quantum number I, that in the case of ^{87}Rb takes the value $I = 3/2$, the hyperfine splitting contribution amounts

Level	A/h	B/h
$5^2S_{1/2}$	$3.41734130545215(5)\,GHz$	
$5^2P_{1/2}$	$408.328(15)\,MHz$	
$5^2P_{3/2}$	$84.7185(20)\,MHz$	$12.4965(37)\,MHz$

(a) Hyperfine splitting constants, measured values [90, 91, 92].

Level	Manifold	K	$\frac{3(K)^2+3/2(K)-I(I+1)J(J+1)}{I(I-1)(2I-1)J(J-1)(2j-1)}$
$5^2S_{1/2}$	$F=1$	-1.25	
	$F=2$	0.75	
$5^2P_{1/2}$	$F=1$	-1.25	
	$F=2$	0.75	
$5^2P_{3/2}$	$F=0$	-3.75	1.25
	$F=1$	-2.75	0.25
	$F=2$	-0.75	-0.75
	$F=3$	2.25	0.25

(b)

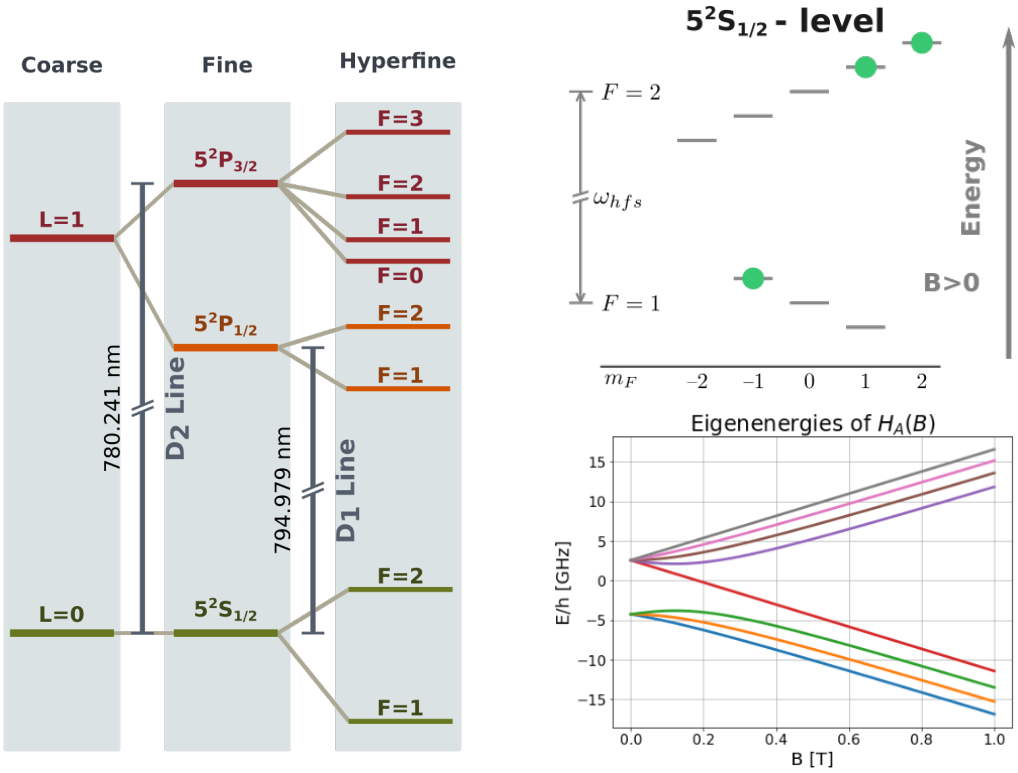
Table 5.2.: In 5.2a experimentally measured values of the magnetic dipole and magnetic quadrupole for different levels of ^{87}Rb. In 5.2b numerical values for the coefficients of the magnetic dipole and magnetic quadrupole for different levels and F–Manifolds.

to [88, 89, 90]

$$\Delta E_{HFS} = AK + B\frac{3\,(K)^2 + 3/2\,(K) - I\,(I+1)\,J\,(J+1)}{I(I-1)(2I-1)J(J-1)(2j-1)} + C \times O\left(K^3\right)$$

with $K = (F(F+1) - I(I+1) - J(J+1))/2$. Here $F \in [|J-I|, J+I]$ is the quantum number relative to the total angular momentum $\hat{\boldsymbol{F}} = \hat{\boldsymbol{J}} + \hat{\boldsymbol{I}}$. While A, B and C are the magnetic dipole, quadrupole and octapole respectively, whose values are known experimentally in the literature and here listed in Table–5.2a, together with the values of K and the multiplication factor in the second order of K for the $5^2S_{1/2}$, $5^2P_{1/2}$ and $5^2P_{3/2}$ levels. Note that the terms depending on $K^p\,, p > 1$ hold only for states presenting $J > 1/2$, which is satisfied only by the $5^2P_{3/2}$ level. Also, experimental measurements of C up to present time, are statistically compatible with zero [89]; for this reason they are not reported here.

For the $5^2S_{1/2}$ and $5^2P_{1/2}$ levels, the total angular momentum can assume the values $F \in \{1, 2\}$; while for $5^2P_{3/2}$, possible values are $F \in \{0, 1, 2, 3\}$. A summarizing scheme of the rubidium structure is provided in Figure–5.1a.



(a) Summarizing scheme of rubidium structure. (b) Zeeman splitting for low fields (top). Full Breit–Rabi diagram (bottom).

Figure 5.1.: In 5.1a the rubidium structure, with fine and hyperfine splittings is illustrated. The D_1 and D_2 lines and their respective wavelengths are indicated (energies not to scale). In 5.1b top: Zeeman splittings for small positive values of the magnetic field B for the $5^2S_{1/2}$ level, low–field seeking states highlighted with green bullets. Bottom: Eigenenergies of the atom–field interaction Hamiltonian for magnetic fields between $0\,T$ and $1\,T$.

5.1.4. Interaction with magnetic fields for Rubidium and trapping techniques

For weak magnetic fields $\boldsymbol{B} = B\hat{\boldsymbol{e}}_z$(i.e. for fields causing Zeeman splitting much smaller than the Hyperfine splittings, see Appendix–A.3), the interaction is well approximated considering only the total angular momentum $\boldsymbol{F} = \hat{F}_x\hat{\boldsymbol{e}}_x + \hat{F}_y\hat{\boldsymbol{e}}_y + \hat{F}_z\hat{\boldsymbol{e}}_z$ and the Hamiltonian can be approximated as [77, 88]

$$H = \mu_B g_F \hat{F}_z \cdot B$$

with eigenvalues

$$E_{m_F} = \mu_B g_F m_F B.$$

For higher fields the eigenenergies do not scale linearly and the diagonalization of the Hamiltonian leads to the Breit–Rabi diagram illustrated in Figure–5.1b (for further details see Appendix–A.3).

When the low field regime holds, the hyperfine sub–states for which the product $m_F g_F > 0$ presents increasing energy with increasing magnetic field magnitude. These states are usually called low–field seeking states. Since it is not possible to create magnetic local maxima using magnetic fields (also known as Earnshaw's theorem [58, 77]), while field minimum are available, low–field seeking states are the only ones that can be trapped using purely magnetic fields and for this reason they are usually referred to as trappable states. For the $5^2S_{1/2}$ level, two hyperfine levels with $F = 1$ and $F = 2$ split into 3 and 5 levels respectively. Of these only the $F = 1, m_F = -1$ and $F = 2, m_F = 1, 2$ are low–field seeking states and therefore trappable.

In order to achieve confinement, the force applied on the atoms by the magnetic field needs to overcome the gravitational attraction of the atoms in the vertical direction. The force created by the magnetic field in the vertical direction is $(\boldsymbol{F}_B)_z = -\partial_z(E_{m_F}) = -\mu_B g_F m_F \partial_z B$, hence of magnitude $|F_B| = \mu_B g_F m_F \, |\partial_z B|$, while that due to gravity acceleration is $\boldsymbol{F}_G = -gM_{^{87}Rb}\hat{\boldsymbol{e}}_z$, with g being the gravitational acceleration and $M_{^{87}Rb}$ being the mass of the rubidium atom. Thus, the condition $(F_B)_z \geq F_G$ must hold for the trap to hold atoms against gravity, setting the constraint for the magnetic field gradient to

$$\partial_z B \geq \frac{gM_{^{87}Rb}}{\mu_B g_F m_F},$$

which, within the same manifold, depends on the third spin component eigenvalue m_F. In the specific case, for the states mentioned above, the gradient must be larger than $30\,G/cm$ for the $|F = 1, m_F = -1\rangle$ and $|F = 2, m_F = 1\rangle$ trappable states and half as much for the $|F = 2, m_F = 2\rangle$ state.

A simple technique for trapping neutral atoms is using the field of a magnetic quadrupole. The magnetic quadrupole is simply obtained by running a constant current in a pair of Helmholtz coils in the anti–Helmholtz configuration. Orienting the two coils with the coaxial axis along the $\hat{\boldsymbol{z}}$ direction, the magnetic field produced can be described by $\boldsymbol{B}_Q = q(x, y, -2z)$ in the vicinity of the centre (note

that this satisfies the Maxwell equations $\nabla \cdot \boldsymbol{B} = 0$ and $\nabla \times \boldsymbol{B} = 0$) for a coordinate frame sitting in the centre of the middle point of the distance separating the two coils. The parameter q describes the gradient of the magnetic field and is proportional to the current running in the two coils. The magnitude of the magnetic field grows with the distance from the origin as $B(x, y, z) = q\sqrt{x^2 + y^2 + 4z^2}$ creating a field minimum at the origin.

In the zero field region, the Zeeman splitting is negligible and the quantization direction is not well defined. Thus, in the zero field region, trapped atoms in low field seeking states might flip spin, to end up in high field seeking states that are expelled from the trap causing atom losses. This process is known as *Majorana losses* [79], and it is more pronounced for steeper traps since the atoms are tightly confined in a low magnetic field region and for colder clouds, since most of the atoms will tend to accumulate in low potential regions. To avoid Majorana losses various strategies can be implemented as, for instance, the Ioffe–Pritchard (IP) trap and Time–averaged Orbiting Potentials trap technique (also known as TOP–trap [93]). The IP–trap consists in a specific arrangement of coils ensuring that the magnetic field is non negligible in any region of the trapping potential, whilst still providing a region of magnetic field minimum. The second case, the TOP–trap, consists in orbiting a quadrupole minimum around the desired trapping location at a frequency that is higher than the trapping frequency of the trap created by the bear quadrupole. This results in a average potential whose minimum sits in a region in which the magnetic field never vanishes. In our case, the zero field regions are avoided through radio frequency dressing of the trap, as described in Section–4.2.1.

Despite being able to hold atoms against gravity, magnetic trapping alone is not sufficient for the purpose of confining thermal atomic gases in a specific region. This is due to the fact that the atoms, of a gas at room temperature, present a very high kinetic energy that allows them to escape the trap. Thus, a pre–cooling stage is required. With the combination of a weak magnetic trap and three axes of counter–propagating circularly polarized light, it is possible to accumulate atoms in a specific region as explained in Section–A.3.1. This technique is commonly known as Magneto Optical Trap (MOT) [58, 77], a preliminary cooling and trapping stage that allows to reach the milli-Kelvin scale, where purely magnetic confinement is achievable.

5.2. Lab layout

The room hosting the laboratory is divided in two parts, respectively the control room and the actual laboratory namely known as laser side, separated by laser safety curtains.

In the control room there is some storage and a general purpose workstation plus a desk hosting a computer. This computer remotely controls the National Instrument PXI computer that queues the experimental sequence. The PXI unit is situated in the laser side Rack A in Figure–5.2, together with Toptica laser controllers; two electronic boxes containing lock–in amplifiers, shutter drivers and AOM drivers; brake-out boxes for analogue and digital input/output; two uni-polar power supplies; a fibre laser (CLEMI) and general electronics as oscilloscopes and function generators.

Always on the laser side there is a second rack (Rack B in Figure–5.2) hosting two bipolar power supplies and other six uni-polar power supplies, together with two optical tables and a rate table hosting a vacuum chamber. The two optical tables are labelled Table A and Table B and host the MOT light preparation and the imaging and optical pumping light preparation respectively.

On Figure–5.2 a schematic view of the laboratory area, showing the disposition of the various parts of the apparatus and the main connections between them. The vacuum chamber is situated on top of a rate table, which consists of an air bearing axis, a wireless high accuracy motor and a controller that is remotely accessed by the computer in the control room.

5.3. Vacuum chamber and external coils

The vacuum system is a relatively compact one, compared to other cold–atom experimental setups. It consists of a main octagonal chamber with seven of the eight lateral ports kept as glass view ports coated for maximum transmission in the infra-red optical spectrum allowing optical access for the MOT, imaging and optical pumping light. The remaining lateral port is connected to a six–way cross where the pumps and the pressure gauge are mounted.

The upper and lower ports are $10\,cm$ wide, on the lower one a coated glass view port is mounted, while on the upper one two different flanges have been mounted

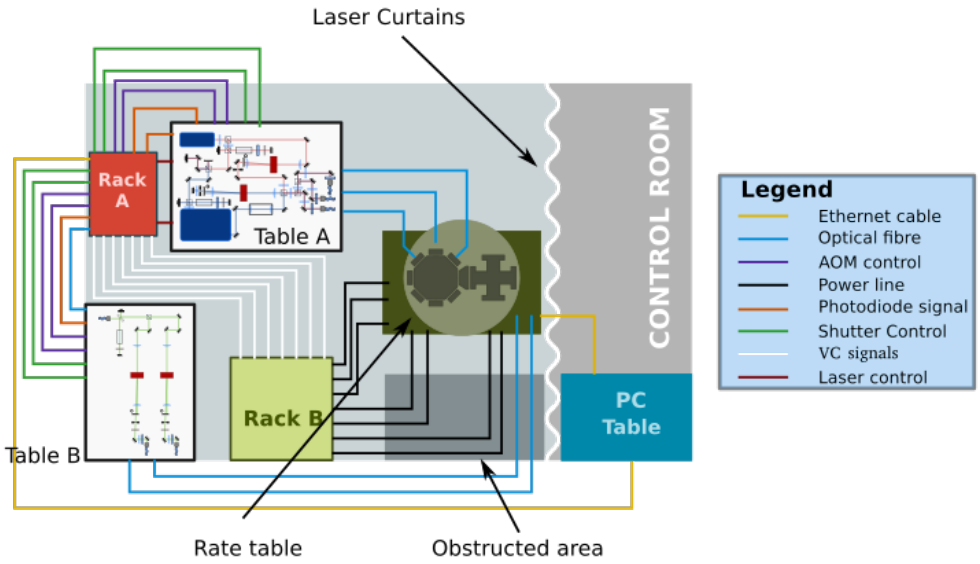


Figure 5.2.: Schematic of the laboratory area, showing the arrangement of experimental equipment and main connections between different devices. In the control room a computer allows to program the sequence exerted by the PXI unit in rack A and the behaviour of the rate table, through Ethernet connection. The rack A also hosts the electronics required for: the frequency stabilization of the lasers sitting in Table A and B, the operation of Acoustic Optical Modulators (AOM) and shutters required for the frequency tuning and the switching of the laser light, and generating the Voltage Control (VC) signals for the operation of the power supplies situated in Rack B.

in two distinct time phases. During the first phase a simple view port has been mounted. This had been used for a preliminary experiment using a permanent loud–speaker magnet to produce a ring quadrupole in cooperation with external coils as described with detail in Section–6.1. During this phase, the Rb dispensers were mounted on a flange situated on the port of the six–way cross, opposite to the main chamber. In the second phase, a flange with four 50–pin sub–D feedthrough connectors, four SMA feedthrough connectors, two optical fibre feedthroughs and a large copper stem feedthrough was mounted on the upper port of the octagonal main chamber. The copper stem plays the role of mechanical mounting for the PCB as well as thermal dissipation for the heat generated on the PCB. The design of this flange allows for experimental operation using the Atom chips and PCB described in Section–5.5 as shown in Figure–5.3.

The vacuum system mounts a NexTorr D200–5 pump, that combines an active

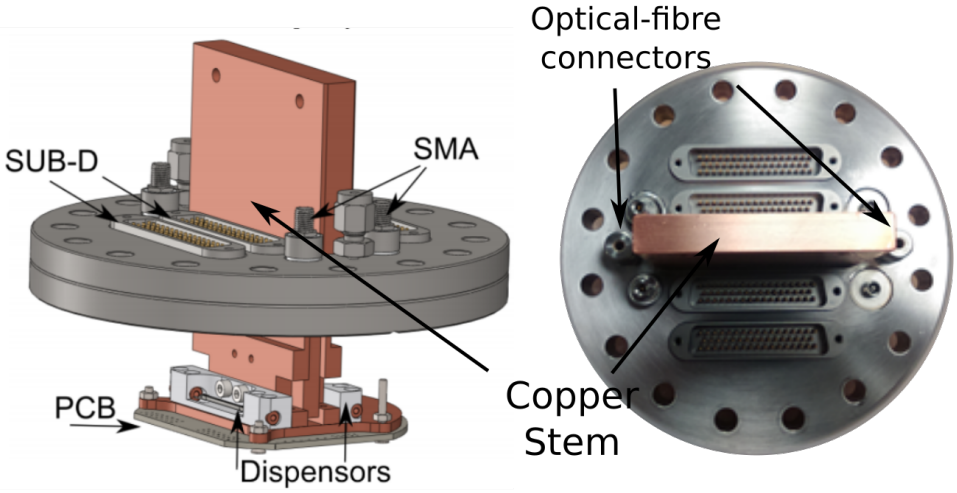


Figure 5.3.: The top vacuum flange. On the left a schematic representation of the PCB and dispensers when mounted on the copper stem. On the right a picture taken from the top. Positions of all the feedthrough connectors are indicated with arrows.

ion pump with a passive NEG (Non–Evaporable Getter) element. This pump can only operate at pressures below $10^{-7} mbar$. To get from atmospheric pressure to the operating range of the Ion–NEG pump, a pre–pumping stage composed by a Pfeiffer Hi-Pace 80 turbo molecular pump and a roughing pump is used in combination with a bake-out procedure.

The roughing pump allows to drop the pressure from atmospheric condition to approximately $10^{-4} mbar$. Successively, the Turbo–molecular pump is activated, reaching a pressure of about $10^{-6}\, mbar$ and a bake–out procedure is followed in order to eliminate water vapours and other residuals from the chamber. This consists of heating the vacuum setup up to a temperature between $150\,^{o}C$ and $200\,^{o}C$ for a time period of a few days up to a week (typical bake–out temperatures and pressures are given in Figure–5.4). To avoid the demagnetization of neodymium magnets present in the ion pump, these are usually removed previous to the bake-out procedure and mounted back when the temperature is dropped below safe temperatures for manual handling, i.e. below $50^{o}C$. However, the peripheral position of the ion pump (see Figure–5.6) allows to keep the pump at a lower temperatures w.r.t. the main body of the chamber. As a matter of fact, the temperature at the ion pump was anyway kept below the maximum temperature suggested by the manufacturer, i.e. $150^{o}C$, for baking-out without the removal of the magnets.

During the bake–out, a few side operations are performed as the activation of the NEG element, the activation of the Rb dispensers and the so called flashing of the pressure gauge. All of these operations consist of running a high current through the element being activated, heating the element to high temperature causing the burning and evaporation of accumulated dirt or chemicals on the surface of the device, sometimes causing the pressure to spike–up for short time–periods.

Once the bake–out procedure is terminated, the temperature of the chamber is progressively decreased allowing the pressure to drop below the threshold value of operation of the Ion–pump. Then the Ion–pump is activated and the temperature decreased, down to room temperature, dropping the pressure to values below $10^{-9}\,mbar$ suitable for cold atom experiments. In later times a valve placed between the six–way cross and the turbo–molecular pump allows to safely detach the latter from the vacuum system. This is needed in order to be able to operate the experiment in rotary motion.

Originally, the rate table was not present in the laboratory and the vacuum chamber was situated on the optical table Table–A. The original position of the vacuum chamber is pictured as a grey outline in Figure–5.8.

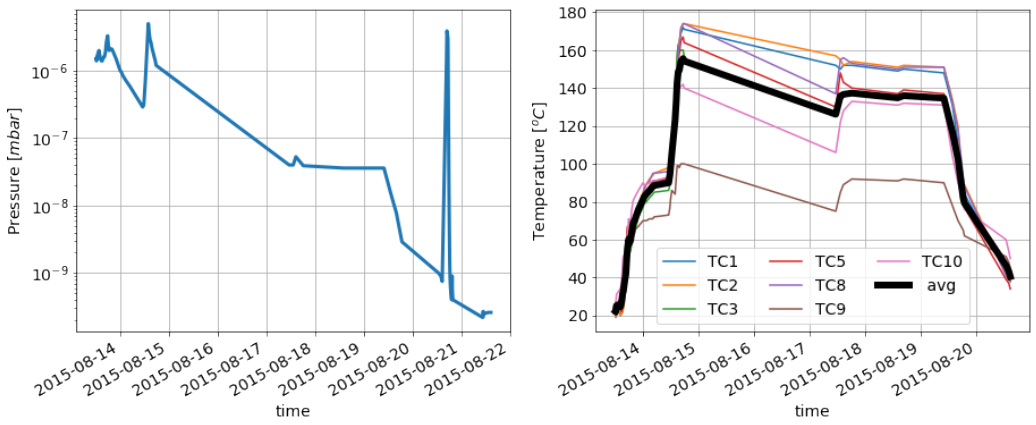


Figure 5.4.: Pressure and temperature of typical bake-out procedure. The high pressure peak around 2015-08-21 is due to the activation of the Ion-pump. The colour lines in the temperature diagram are the temperature readings from various temperature sensors – thermocouples (TC) – placed in different parts of the vacuum chamber as illustrated in Figure–5.6, while the black thick line pictures the average temperature of the chamber.

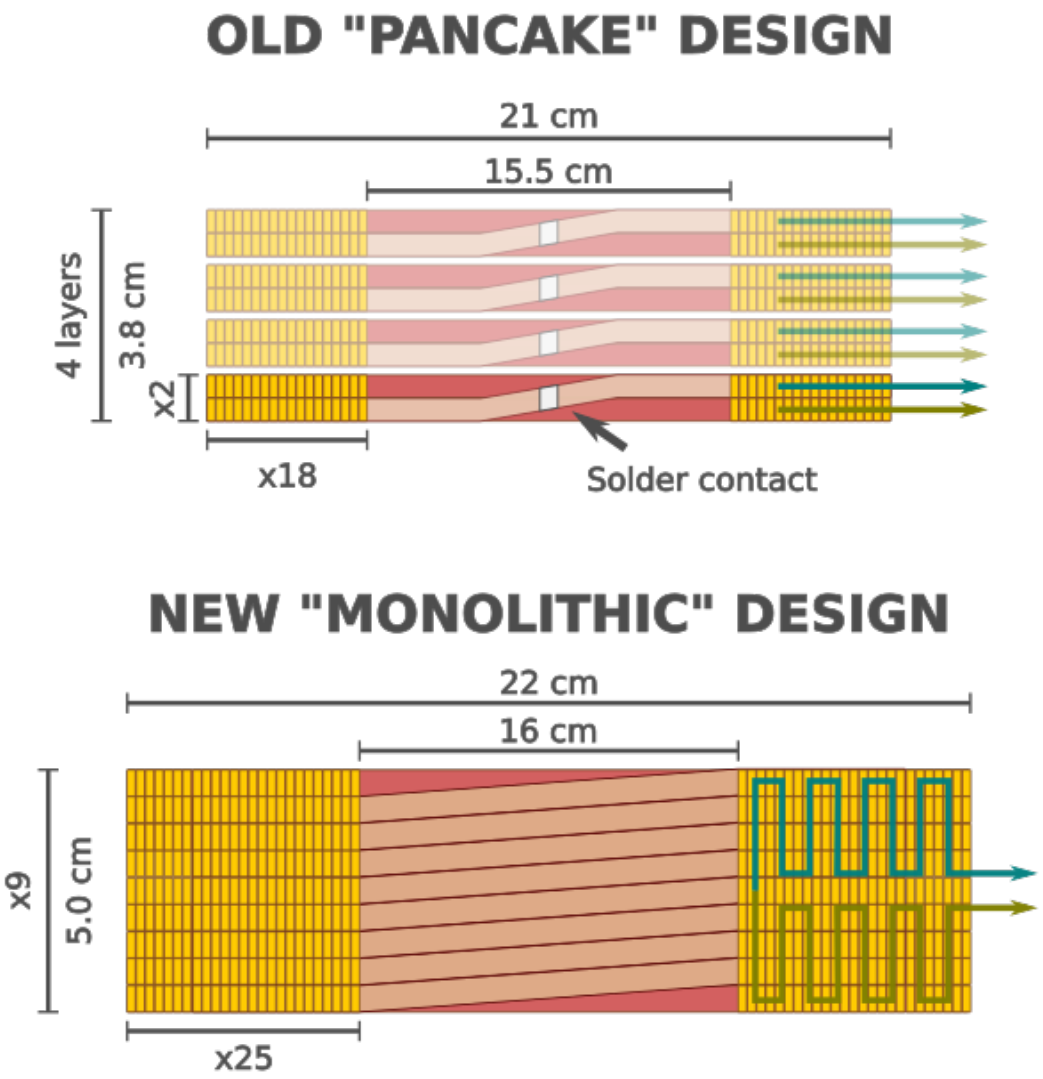


Figure 5.5.: Graphical scheme of the two coil designs. The earlier "pancake" design presents four couples of coils. Each pair is composed by two single layer spirals soldered together on the internal side of the solenoid, ensuring that the feeding contacts are found on its external side. The resulting coils are then stacked one on the other obtaining this pancake-looking structure. In the latter "monolithic" design the winding procedure starts from the centre and proceeds in two opposite directions, winding the lower half of the solenoid and back-winding the upper half. In both schemes the layering order of the coil is indicated with the green and blue paths: disconnected on the first case, while connected in the second one.

5.3.1. Coils on the chamber

On the top and bottom of the main chamber, two coils are mounted to generate the magnetic fields required for initial MOT and magnetic trapping stages separated by $85\,mm$ in the vertical direction (see Figure–5.6). Each of these two coils was originally composed by four sections containing 36 turns distributed in two layers for a total of 140 turns per coil with overall dimensions being: $21\,cm$ for the outer diameter; $15.5\,cm$ for the inner diameter and $2.8\,cm$ tall. In each section, the two layers were wound independently with a rectangular wire of $1.6 \times 3.5\,mm^2$, soldered together in the middle point facing the inner radius. Albeit having the advantage of being scalable and easy to manufacture and presenting connections accessible from the outside, this design resulted in interrupted circuits of few of the sections after several months of operation. This is due to the soldered joints in each of the sections presenting an increased resistivity with respect of the remaining section of the coil. Running currents up to $20\,A$, for extended periods of time, causes the joints to heat up to high temperatures and, consequently, their progressive decay.

These two coils have been substituted with two custom made coils presenting 225 turns each, with a single non–interrupted wire of $3.14 \times 1.4\,mm^2$ rectangular section and overall dimensions of: $16\,cm$ inner diameter, $22\,cm$ outer diameter and $50\,mm$ height. Each coil presenting a measured resistance of $0.9\,\Omega$. Albeit the overall structure of the coil is simpler than the "pancake structure explained above, its manufacturing results to be harder. For the pancake structure it is only necessary to wind a length of wire around itself and then connecting the resulting spiral with an identical one soldering the two internal ends. while, for the monolithic structure, it is necessary to wind from the middle section successively layering half of the coil and then start back–winding the other half in order to have the two ends of the wire on the external side of the solenoid. For a graphical explanation, see Figure–5.5.

Externally to the vertical axis coils, two pairs of coils oriented orthogonally on top of each other have been installed as illustrated in Figure–5.6. These coils provide bias fields in the horizontal plane. Each of these consists of two coils of 20 windings each, separated by $\sim 10\,cm$.

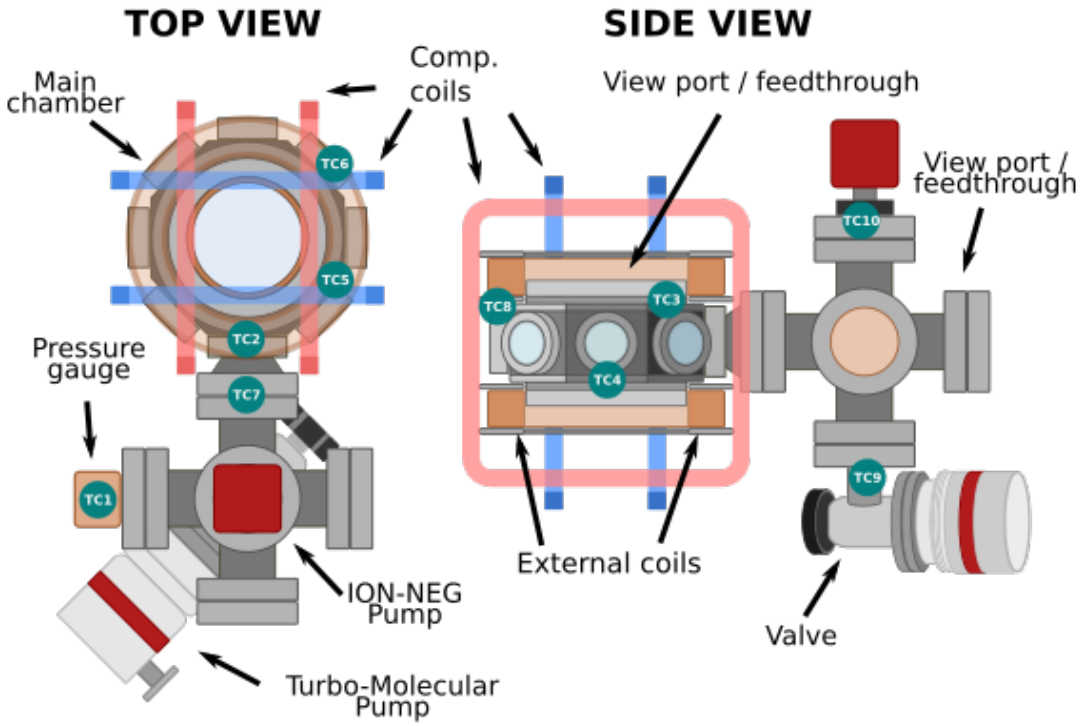


Figure 5.6.: Scheme of the vacuum chamber with coils mounted on it. The circles TC1–TC10 indicate the position of thermocouples during the bake–out operation. Detailed description in the text.

5.4. Laser setup

Laser light is used in this experiment to perform initial cooling of the atoms through a MOT stage, optical pumping of the atoms into the easiest trappable state (i.e. the state $|F = 2, m_F = 2\rangle$) of the $5^2S_{1/2}$ level and for absorption imaging of the atoms. Each of these operations requires one or more laser frequencies exciting specific transitions between different hyperfine levels of the D_2 line.

Specifically, the MOT requires two frequencies; one of which is red de–tuned from the transition $F = 2 \rightarrow F' = 3$ to establish the cooling cycle, while the other one is resonant with the transition $F = 1 \rightarrow F' = 2$ with the purpose of re–inserting atoms "fallen–off" from the cooling cycle back into the desired states (so–called re–pumping light). The optical pumping requires light resonant with the transition $F = 2 \rightarrow F' = 2$ and finally absorption imaging requires light resonant to the $F = 2 \rightarrow F' = 3$ transition. For shortness, the sub-levels of the $5^2P_{3/2}$ are distinguished from the sub-levels $5^2S_{1/2}$ with a prime symbol and the transition between sub-levels represented as arrows, e.g. the transition between

the $F = 2$ sub-level level of the $5^2S_{1/2}$ and the $F = 2$ sub-level level of the $5^2P_{3/2}$ is written as $F = 2 \rightarrow F' = 2$.

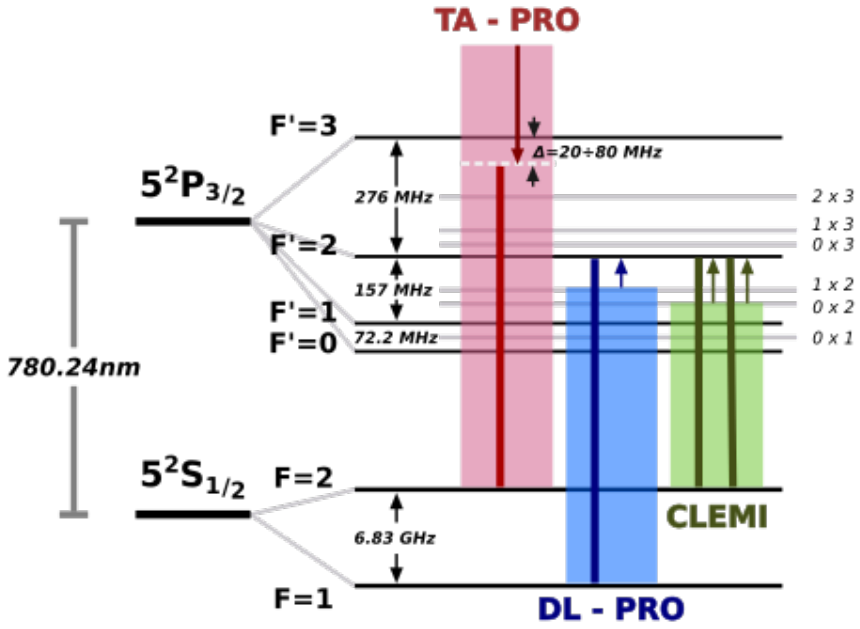


Figure 5.7.: This scheme pictures the hyper-fine structure and the locking scheme of the lasers in our setup for the $5^2\mathrm{P}_{3/2}$ and $5^2\mathrm{S}_{1/2}$ levels of ^{87}Rb. The red, blue and green rectangles indicate the locking frequencies for the TA-pro, DL-pro and CLEMI lasers respectively. The DL-pro is locked to the transition $F = 1$ and the crossover peak between $F' = 1$ and $F' = 2$ (abbreviated $1 \rightarrow 1 \times 2$), then its frequency is shifted up by $78.5\,MHz$ to get the re-pumping beam; the CLEMI is locked to the transition $2 \rightarrow 0 \times 2$ and shifted up by $114\,MHz$ for both the imaging and optical pumping beams. The frequency of the TA-pro is locked with respect to the DL-pro ensuring that the beat-frequency of the two laser corresponds to $6.83\,GHz$, it is then shifted down to the cooling frequency, red detuned by $20 \div 80\,MHz$ with respect to the $2 \rightarrow 3$ optical transition.

The experiment is equipped with three light sources for the generation of the required frequencies; namely two external cavity diode lasers from Toptica (models: DL–pro and a TA–pro), one of which includes an integrated tapered amplifier (the TA–pro); and a fibre laser designed and built at the University of Birmingham (CLEMI). Each of the lasers is frequency stabilized to a specific spectroscopy feature, using a lock–in amplifier or beat–lock with respect to some reference frequency scheme. The desired transitions are then obtained shifting the frequency of the light source by means of Acousto-Optical Modulator (AOM) stages. The

set of locking frequencies for each of the lasers and the transition frequency obtained from them is illustrated and described in more detail in Figure–5.7.

The prepared light is then collected into polarization maintaining optical fibres and delivered to optics directly mounted on the vacuum chamber to be shone onto the atoms. Further details are provided in Section–5.4.2.

5.4.1. Optical tables

The three light sources present in the laboratory are distributed on two different optical tables, namely Table–A and Table–B as illustrated in Figure–5.8. Table–A is host to the two Toptica external cavity diode lasers emitting light at 780.24 nm. The first one is a DL-pro model outputting about 70 mW of optical power, While the second one, a tapered amplified TA–pro produces two outputs, the first one is derived from the seed laser and consists of few milliwatt of power, while the second comes out of the amplified beam producing up to 900 mW.

Part of the output of the DL–pro is extracted from the main beam and is then

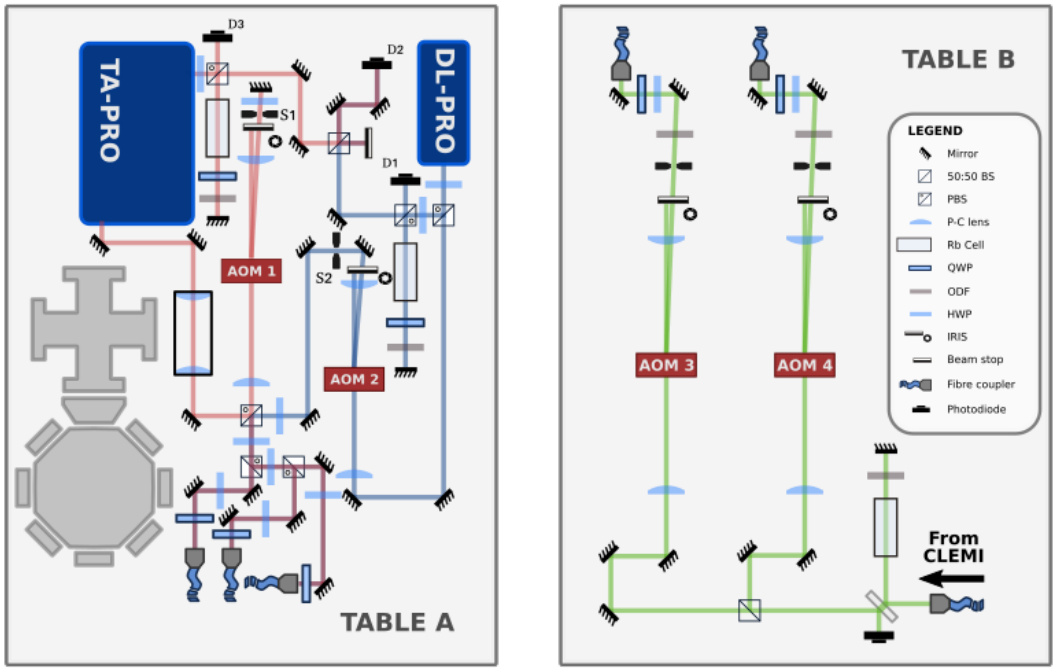


Figure 5.8.: Optical tables Table A and TableB in Figure–5.2. On the legend are listed the following acronyms; BS: Beam Splitter; PBS: Polarizing BS; P–C: Plano–convex; QWP: Quarter Wave Plate; ODF: Optical Density Filter; HWP: Half Wave Plate.

distributed among a Doppler free spectroscopy stage onto which the frequency stabilization of the laser is set to, and to a second beam overlapped with light coming form the TA–pro seed beam, directed to a fast photo detector for beat lock purpose. The locking point of the DL-pro is set to the crossover peak between the $F' = 1$ and $F' = 2$ of the $5^2P_{3/2}$ level using a lock–in amplifier [94].

From the seed beam of the TA–pro part of the light is extracted towards a Doppler free spectroscopy stage [77], whose role is to provide a diagnostic tool in case of misbehaviour of the laser; the remaining portion is overlapped with the beam derived from the DL–pro directed to the fast photo detector mentioned above.

The overlap of the two beams is used for the frequency stabilization of the amplified laser. Once locked onto the desired frequency, the DL–pro provides a reference frequency. The frequency of the TA–pro is then stabilized keeping the beat frequency of the overlapped beam of the two lasers to a constant desired value. For the specific case, this approximately equals the Hyperfine splitting, i.e. $\sim 6.8\,GHz$.

The remaining power from the DL–pro is sent through a single pass AOM stage changing its frequency to the re–pumping transition. Then, the light is overlapped with the light coming from the amplified output of the TA–pro and distributed into polarization maintaining single mode optical fibres to be shone into the vacuum chamber through the lateral view ports. Before overlapping with the re-pumping light, the amplified output of the TA–pro is sent to a double pass AOM stage to move the frequency of the beam to a frequency de–tuned from the $F = 2 \rightarrow F' = 3$ transition of about $20\,MHz$ to $80\,MHz$ obtaining the cooling light.

The overlapped cooling and re-pumping light needs to enter the fibres with the same polarization. This is because before being shone into the vacuum chamber the light is sent through a polarizing beam splitter for polarization cleaning. Thus, mutually orthogonal polarizations of the cooling and re-pumping lasers, result in excluding one of the two beams from being shone onto the atoms.

5.4.2. On chamber optics

The output light from the CLEMI laser is brought from Rack 1 to Table B using a polarization maintaining optical fibre. The light is then sent to a Doppler–free spectroscopy stage for the frequency stabilization by means of a lock–in amplifier

scheme and successively split into two beams. Each beam is sent to a single pass AOM stage to obtain the desired frequencies for the imaging and optical pumping light. Then the light is coupled into two optical fibres and brought to the vacuum chamber area. We observed that, while the optical power from the CLEMI laser is stable in time, the out coming polarization is subject to fluctuations depending on temperature fluctuations. For this reason, the optical element used in table B are chosen to be polarization independent, where possible.

To form a MOT and perform operations such as absorption imaging and optical pumping of the atomic clouds, it is necessary to shine laser beams with specific frequencies, polarizations and directions inside the vacuum chamber. This is achieved with optics mounted directly on the chamber and on neighbouring supports as illustrated in the schematics of Figure–5.9.

The MOT requires, beside the magnetic fields provided by the external coils, light coming from three linearly independent axes to cool down the atomic motion in the three axes. In each axis the light needs to come from both directions with opposite handedness circular polarization. For the horizontal axes, the light transported with a polarization maintaining single mode optical fibre, is shone from an out-coupler as a collimated beam with a waist of about $2\,cm$ in a polarizing beam splitter, to filter out spurious ellipticity. The cleaned beam passes through a quarter wave plate, oriented such that the polarization axis forms an angle of $\pm 45\,deg$ with its fast axis to obtain right(left) handed circular polarization. The circular polarized light then crosses the main vacuum chamber, and at the opposite end a second quarter wave plate changes the polarization of the beam in linear polarization again, oscillating along an axis $\pm 45\,deg$ from its fast axis direction. Then a coated mirror retro–reflects the light in the same axis. The orientation of the second wave plate is not crucial, as the light reflected from the mirror forms automatically an angle of $\mp 45\,deg$ with the quarter wave plate's fast axis, resulting in circularly polarized light in the chamber with opposite handedness with respect to the forward beam. The vertical axis differs from the other two by a polarizing beam splitter placed between the mirror and the second wave plate. This allows to integrate a vertical absorption imaging setup explained later on. In this case the second wave plate plays a role, since it is required that all the optical power is transmitted, through the polarizing beam splitter, towards the mirror for retro–reflection.

To image the atoms and estimate the number of trapped atoms, absorption

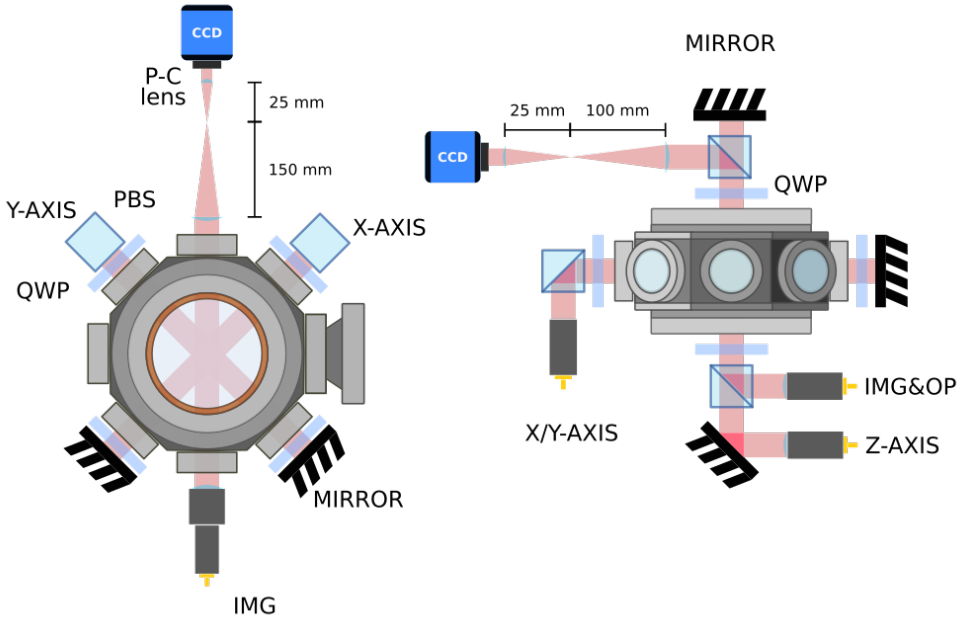


Figure 5.9.: Schematics of the optics in the vacuum chamber area. On the left: horizontal MOT axes and imaging system are illustrated. On the right vertical MOT and imaging axis, together with a lateral view of a horizontal MOT-axis. The abbreviations used are PBS for Polarizing Beam Splitter, QWP for Quarter Wave Plate and P-C lens for Plano-Convex lens.

imaging is used. This consists of shining a beam of laser light resonant to a specific transition in the atomic cloud (in our case the targeted transition is $F = 2 \rightarrow F' = 3$ as illustrated in Figure–5.7); part of this light will be absorbed by the atoms and scattered in random direction, while the rest will be collected into a CCD camera. The obtained image is then compared to one in the absence of atoms [95, 96]. The intensity I of the resonant light reaching the camera is ruled by the Beer law

$$\frac{I}{I_0} = e^{-n\sigma_0}$$

where σ_0 is the absorption cross section for resonant light, n is the column density of atoms and I_0 is the incoming light intensity. The column density can be expressed as $n = N/\Sigma$ with N the number of atoms in the column and Σ the column section surface. This means that knowing the CCD's pixel size and the magnification of the optics (i.e. knowing the section area of the column covered by every pixel) it is possible to determine the number of atoms in the column as a function of the ratio of light intensity collected by the pixel in the presence and

absence of atoms.

The absorption imaging system is formed by a collimated beam shone on an atomic cloud and successively re–sized by means of a telescope with a magnifying factor M and collected on a CCD camera. The telescope is formed by two lenses separated by a distance equal to the sum $\Delta l = f_1 + f_2$ of their focal lengths f_1 and f_2. The magnification factor is then given by the ratio $M = f_1/f_2$ between the two focal lengths. Each pixel of the camera detects the light corresponding to a column of section area $\Sigma_c = M\Sigma_p$where Σ_p is the area section of each pixel. On the chamber are mounted two imaging systems, a horizontal one with magnification $M_h = 6$ and a vertical one with magnification $M_v = 4$. The CCD camera used in both of the axes is a black and white sensor with an array of 640×480 square pixels of $5.6\,\mu m$ side length. While the horizontal imaging system can be applied directly, the vertical axis shares the propagation trajectory with the z-axis MOT light and requires further optics. Practically, the light is injected from the other port of the first polarizing beam splitter, causing the light to have opposite circular polarization handedness of the light with respect to the MOT light in the chamber. After the second wave plate, the imaging light presents linear polarization orthogonal to the MOT light one and can be separated from the latter by means of the second polarizer, opportunely orientating the second wave plate. Successively the light passes through the telescope and ultimately illuminates the CCD camera.

5.5. Chip Design

The static and oscillating magnetic fields required to perform magnetic trapping and radio–frequency dressing, following the scheme illustrated in Section–4.2.1, are generated using atom chip technology. The usage of micro fabricated wires on isolating substrates is a technique of growing importance among the cold atoms community. The main advantage is to provide high field gradients using low currents, reducing the power consumption of the experimental setup as well as its physical size.

The set of micro fabricated devices consists of two chips with copper conductive tracks on silicon substrates, gold plated where required. These two chips have been designed in Nottingham, and manufactured in the University of Ben Gurion,

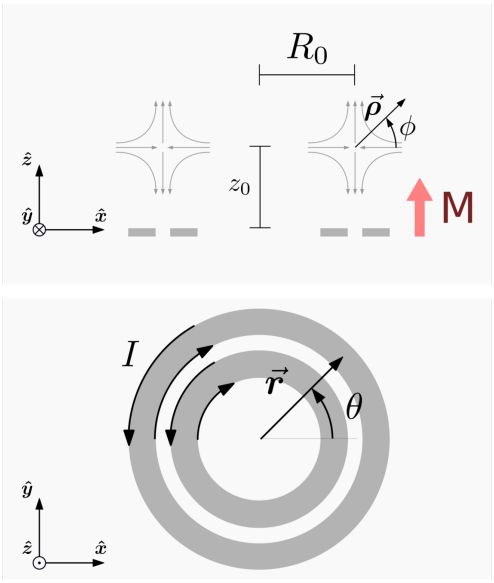
both tailored to be used with the trappable hyper-fine states in the $5^2S_{1/2}$ electronic level of ^{87}Rb. The set is completed by a Printed Circuit Board consisting of five nested coils plus two smaller circular features designed to ease the loading of the atoms in the micro fabricated chips.

5.5.1. Ring quadrupole electro–magnet

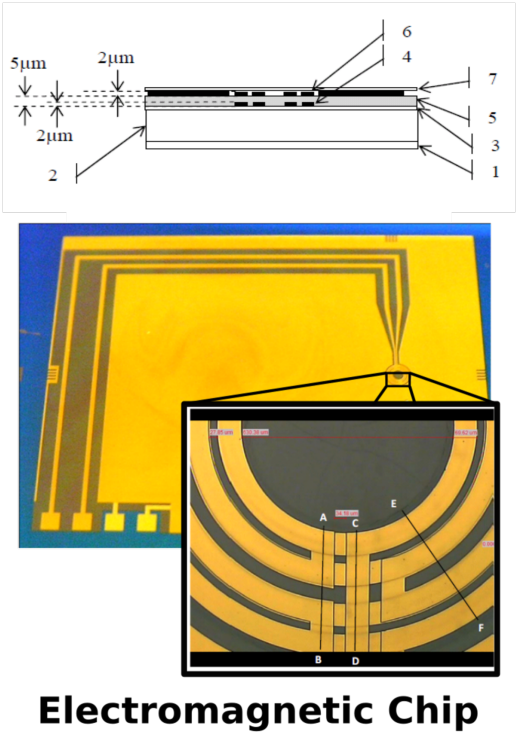
The first element required is the static ring quadrupole magnetic field, producing a magnetic trap with circular geometry. As previously illustrated in Section–4.2.1, this can be achieved with four current carrying loops spatially placed on the edges of a square section ring. Despite being a simple structure, this presents obstructed optical access in the region of trapping. Moreover, its micro fabrication would require high precision in the alignment of each single loop that becomes cumbersome in the three–dimensional space.

A feasible alternative consists in arranging four concentric conductive loops radially separated by a distance d and having a conductor size w , running the same current I in opposite directions as illustrated in Figure–5.10a. This structure forms a magnetic field that well approximates a ring quadrupole field at a fixed height $z_0 = \sqrt{d(2w+d)}/2$, whose gradient is proportional to the current running in the structure. The same field can be produced using two concentric ring magnets presenting a magnetization in the vertical direction of magnitude $M = I/h_T$ (indicating with h_T the thickness of the magnets), whose edges coincide with the current loops [51].

The critical requirement for this design is that it must produce a high field–gradient in the vertical direction, as explained in the previous section, to overcome gravity. Moreover, this field requirement needs to be met running a current below the maximum current density that the wire can withstand. Specifically, for the trappable Zeeman sub-levels of the $5^2S_{1/2}$ manifold with $|m_F| = 1$ the gradient must be greater than $30G/cm$. Measured current densities for micro fabricated gold wires are reported to hold current densities in the order of $> 4 \times 10^{10}\, A/m^2$ in contact with air [97, 44]. This would allow the designed chip, presenting gold tracks of $70 \times 2\,\mu m^2$, to sustain a current of up to $5.6\,A$ when in contact with air. Since the chip is required to function in Ultra high vacuum conditions, at approximately $10^{-10}\, mbar$ for which heat dissipation through air convection is suppressed, the maximum allowed current density is expected to



(a) Working principle of atom chip design.

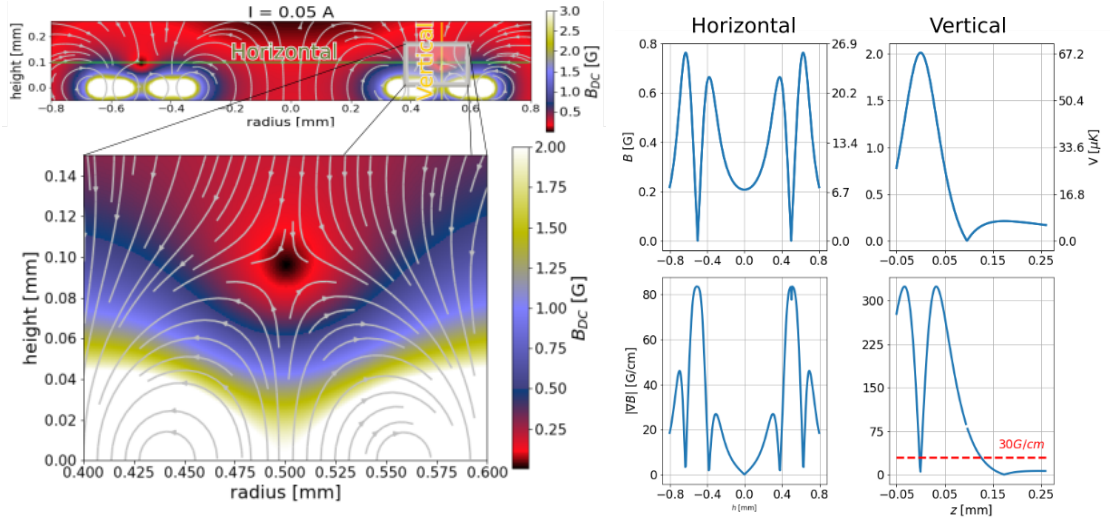


(b) Top: layer scheme of the chip. Bottom: Image of the electromagnetic chip fabricated in Ben Gurion University.

Figure 5.10.: On the left 5.10a: principle of operation of the atom chip design for a ring quadrupole. The coordinates described refer to the notation used in Section–4.2.1. On the right 5.10b: a picture of the manufactured chip and layer label scheme. The insulating and protective SiO_2 layers 1, 3, 5 and 7; the Si wafer 2, and the gold layers 6 and 4.

be lower with values depending on conductive heat dissipation. Nonetheless, the reported maximum current densities were measured in conditions for which the conductive heat dissipation dominates air convection dissipation (i.e. in thermal contact with a metal heat sink), thus providing values compatible with in–vacuum conditions.

The design sees four current loops with diameters 1300 μm, 1108 μm, 852 μm and 700 μm [84]. A representation of the strength and direction of the field produced on a sectioning plane can be seen in Figure–5.11 together with the field strength and its space derivative along the axis crossing one of the minima for both the horizontal and vertical direction. The minimum is found at a height of 0.1 mm and 0.5 mm away from the centre. It is shown that the gradient in the



(a) Cross section view of the magnetic field produced by the chip.

(b) Field strength and potential (top) and gradient (bottom) along the the vertical and horizontal directions indicated as the green and yellow lines in panel (a).

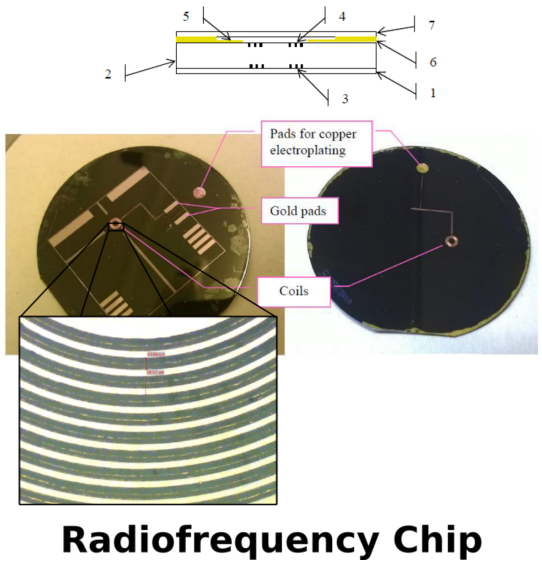
Figure 5.11.: In (a) the magnetic field strength and direction on the plane orthogonal to the chip is shown for a current of 50 mA running in the gold tracks (well below the maximum current limit of 5.6 A). In the lower panel, a zoom in view in proximity of the minimum (whose position is independent from the used current) situated at a radial distance of 0.5 mm and at a vertical distance of 0.1 mm from the chip surface. In (b) the field strength, potential profile (in terms of the temperature) and field gradient along the horizontal and vertical directions in correspondence of the coordinates of the minimum are shown. The critical value of the minimum gradient of 30 G/cm required to magnetically hold atoms against gravity is indicated as the dashed red line for the vertical direction.

vertical direction in the region of the minimum is well above the required gradient (indicated by the red dashed line), when the loops are running a current of 0.05 A. Because of manufacturing reasons, a single layer would produce a discontinuity in the axial symmetry, due to the wires feeding the electromagnet. Therefore two layers are required, in which the feeding connections are on opposite sites of the chip. In this way it is possible to switch between the two layers depending on the position of the atomic clouds. This chip has been electroplated on a 280 μm Silicon substrate with both top and bottom surfaces covered by an insulating layer of SiO_2 (respectively (2) and (1,3) in Figure-5.10). Between the two conductive layers there is a planarization stage and the top a gold coating covers all the

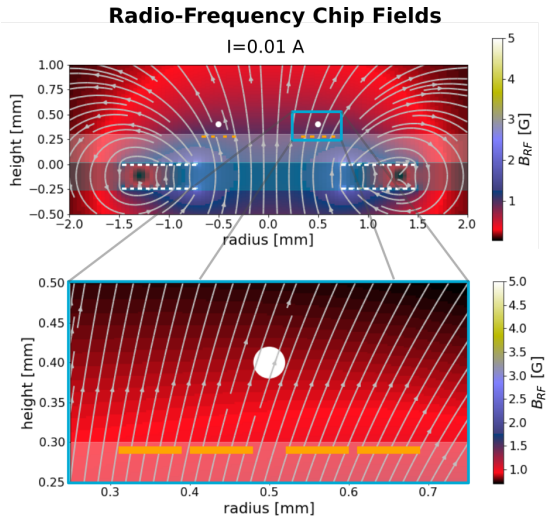
available surface to function as a mirror to be used for reflective imaging; a final layer of silicon dioxide SiO_2 is deposited to protect the structure underneath ((5) and (7) in Figure-5.10).

5.5.2. Radio–frequency chip

The second element required to implement the trapping scheme in Section–4.2.1 is an elliptically polarized oscillating magnetic field in the radio–frequency regime. To achieve this it is necessary to have a non–zero radial component of the magnetic field in the plane of the quadrupole ring field minimum. Then, a uniform field oscillating in the vertical direction with the same frequency as the radial field can be used to form elliptical polarization changing the relative phase with respect to the radial field.



(a) Image of the radio–frequency chip fabricated in Ben Gurion University.



(b) Fields produced by the chip.

Figure 5.12.: On the left 5.12a pictures of the radio frequency chip and layer label scheme are shown. On the right 5.12b the fields produced by the chip when running a current of 0.01 A is shown; the substrates of the ring–quadrupole chip and its own are shown with transparent white and grey rectangles together with the positions of their wires; the approximate positions of the quadrupole ring minimum are indicated with white circles.

To have a non–negligible radial component it is necessary to have a coil geometry with size comparable to the ring–trap size. Since the radius of the quadrupole

ring trap is equal to $0.5\,mm$, the radio–frequency coil needs to be manufactured with micro fabrication techniques.

The design, described with detail in the doctoral thesis of Tom Bishop [84], consists of two copper spirals ((3) and (4) in Figure–5.12a bottom) electroplated in trenches etched on a silicon wafer ((2) in Figure–5.12a). The spirals present 10 turns each, with radii regularly spanning the interval between $750\,\mu m$ and $1450\,\mu m$ and conductive tracks of about $40 \times 40\,\mu m^2$. Since copper presents higher electrical and thermal conductivity than gold, the maximum allowed current density is expected to be (in a pessimistic scenario) in the same order as for gold, i.e. at $10^{11} A/m^2$ according to [97, 44]. Hence, under these assumptions it is reasonable to assume the coil to withstand currents up to $\sim 16\,A$. In any case, the field amplitude require for the radio frequency dressing scheme is in the order of a few Gauss in the area around the location of the quadrupole minimum.

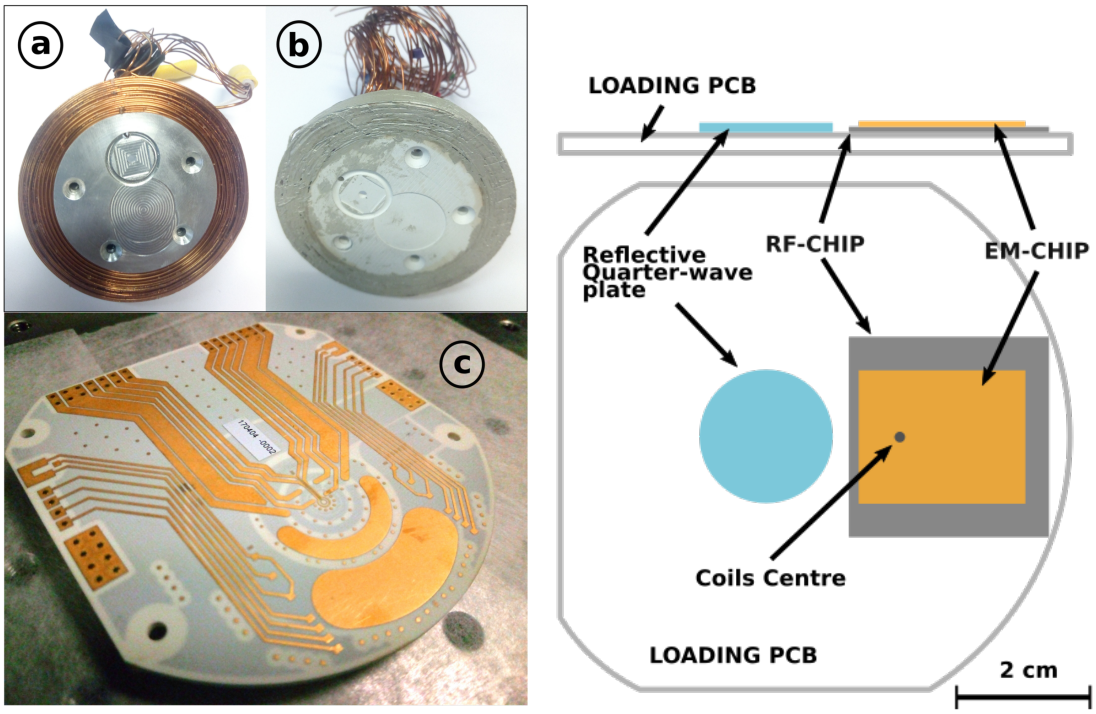
As it can be seen in Figure–5.12b, with a current of $10\,mA$ a field amplitude of about $1\,G$ is achieved in proximity of the quadrupole minimum (whose location is indicated with a white circle in the figure). Furthermore, the radial component of the magnetic field produced by this chip in the region where the ring–quadrupole minimum is expected is non–negligible, allowing for the desired polarization of the magnetic field.

The lower surface is insulated with a SiO_2layer while at the top gold pads are present for connections with the electromagnetic chip and a protective layer of SiO_2 ((1), (5,6) and (7) in Figure–5.12a).

5.5.3. Printed Circuit Board for loading atoms in the chip

The two chips illustrated in the previous sections correspond to the core apparatus for the implementation of the trapping scheme. The remaining fields required can be easily generated with coils external to the vacuum chamber. The only remaining issue is to succeed in loading the atoms from an initial trap (MOT or magnetic trap) produced with coils placed outside the vacuum chamber into the final trap provided by the atom-chips previously described.

To perform this task it is possible to insert an intermediate in-vacuum structure of nested coils providing intermediate field–gradients to size ratios. The first design attempt saw a structure made out of aluminium and MACOR ceramics, in order to hold a set of three non–coaxial nested coils, plus the possibility of a fourth coil



(a) Loading structures (a–b) and PCB (c).

(b) Chips, reflective quarter wave plate and PCB scheme of assembly.

Figure 5.13.: On the left 5.13a structures and PCB built for loading of the atoms in the chip; (a) non–vacuum prototype; (b) vacuum–compatible version; (c) PCB. On the right 5.13b the assembly and relative positions of PCB, chips and reflective quarter wave plate is shown.

for additional radio–frequency fields (e.g. for the generation of the vertical component of the elliptically polarized field or for cooling techniques as evaporative cooling). Two prototypes of this structure have been manufactured in the workshops facility of the Physics department. The first sample produced was built in aluminium and the coils assembled with non–vacuum compatible materials. Its purpose was to test coil winding techniques and manufacture feasibility with the workshop facility.

The assembly of the first sample resulted in a working prototype. Therefore, a second sample produced using UHV-compatible materials such as Kapton insulated strand wires and conductive glue for heat dissipation has been produced. Unfortunately, the assembly of this second prototype resulted in a faulty device. Most of the coils shorted because of the low mechanical resistance of the insulating Kapton layer of the wires and the conductivity of the used glue.

As an alternative a PCB structure has been designed here in Nottingham (see

Figure-5.13a(c)). Its manufacture has been outsourced to Hughes Circuits, Inc. This structure is a ten-layer PCB with copper strips on Rogers 4350/4450 laminate material (a ceramic based laminate for PCBs) except the two external layers whose finish is gold plated. It presents five co-axial nested coils plus two circular features on the top layer that could be used for field gradient adjustments. The maximum current that can run in each coil varies between $15A$ for the external (largest) coil to about $5A$ for the smallest coil[1] [84]. On the top layer are visible the electrical connections towards the area in which the chips discussed in Section– 5.5.1 a pagina 70 and Section– 5.5.2 a pagina 73 are to be glued on this PCB.

The manufactured product has been delivered to us but during testing we realized that the manufacturer drilled holes for pin connectors (visible in the image on the sides of the PCBs) of a different diameter with respect to the one indicated by us. After a long search on the market for suitable pins, it has been attempted to mount pins of similar size whose installation resulted in the partial damaging of the board. As a result, the commission of a second set of samples, complete with pin installation, was necessary. At the present moment the second generation of PCB has been manufactured and shipped to our collaborators in Ben Gurion University for the assembly of the PCB with the atom chips previously described.

5.5.4. Assembly

Misalignment of the radial radio–frequency field with respect to the ring quadrupole can lead to deformed elliptical polarization, causing major defects of the dressed potential. Hence the alignment of the radio–frequency chip and the electromagnetic chip requires micro metric precision.

The alignment of the PCB with the other two elements is still important, but minor adjustments with fields produced externally to the vacuum chamber can be performed. For the time being, the procedures of alignment and gluing of these three devices are being carried out in the University of Ben Gurion. Once the assembly procedure is complete, the resulting product will be shipped back to the University of Nottingham, where electrical connections between the PCB and the two chips will be effectuated with a gold wire bonding technique.

[1] For the extra two internal loops we expect to be able to run currents up to 3 A.

Once this operation is terminated, a reflective quarter–wave plate will be glued $2\,cm$ away from the centre of the ring trap location, on the surface of the PCB using vacuum compatible UV–cured glue to be used in the MOT phase. Successively, the assembled device will be mounted on a holding structure (that will sit inside the vacuum chamber once fully assembled), and the electrical connections to the feedthroughs performed. Note that the flange on which the feedthroughs are present will be mounted on the top port of the main chamber. As a result, in the fully mounted vacuum setup, the chips and PCB face downwards.

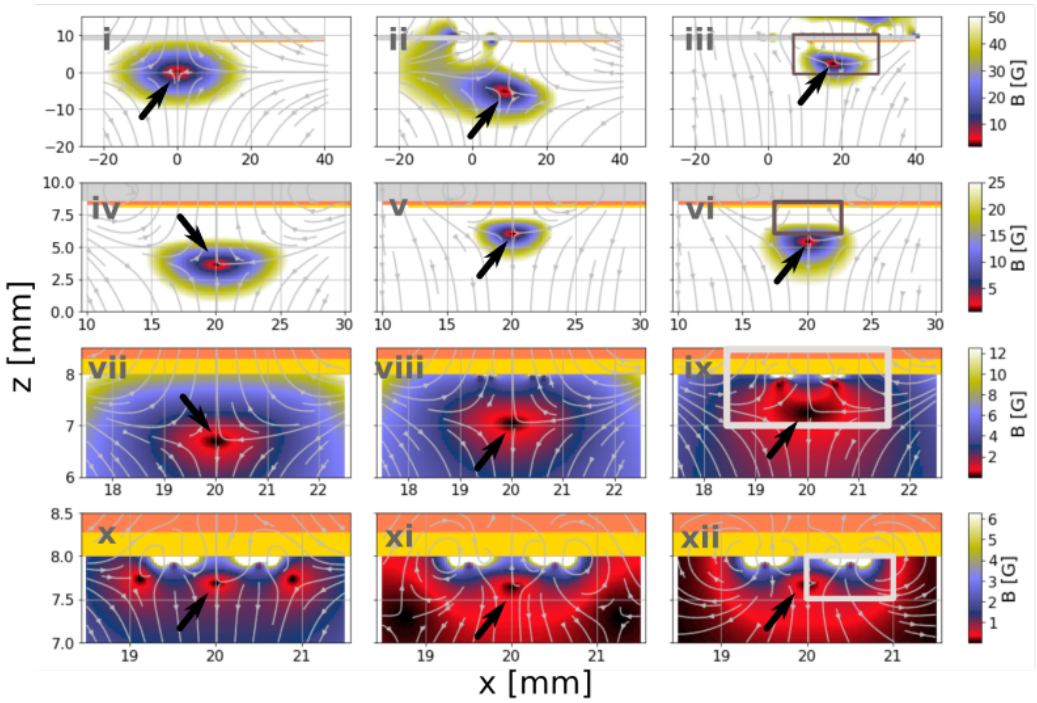


Figure 5.14.: Loading sequence of atoms from an initial magnetic trap formed by the combined action of the external coils and the larger coil in the PCB (i) to the central minimum of the electromagnetic chip (xii). The grey, orange and yellow regions represent the volumes occupied by the PCB, radio frequency chip and electromagnetic chip respectively. In each row the last figure (iii, vi, ix and xii) a box representing the field of view of the next row is shown; for the last row the box represents the field of view for the sequence in Figure–5.16. The position of the minimum containing atoms is indicated by a black arrow.

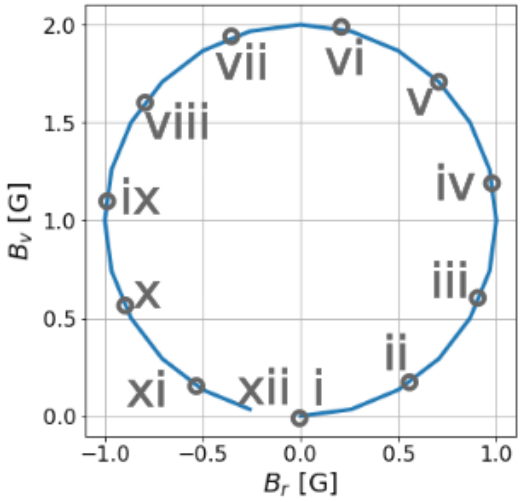


Figure 5.15.: Radial (B_r) and vertical (B_v) magnetic fields diagram of the second part of the loading sequence. Trajectory going anti–clockwise. The points i–xii mark the different moments of the quadrupole ring loading sequence shown in Figure–5.16.

5.5.5. Loading Sequence

In a typical experimental sequence, the atoms are initially accumulated in a MOT using the two external coils and the MOT light (cooling and re-pumping light), then the laser light is turned off and the current running in the external coils ramped up to achieve a vertical magnetic gradient suitable for magnetic trapping of all the trappable states of the $5^2S_{1/2}$ level (i.e. greater than $30\,G/cm$, as explained in Section–5.1.4). The trapped atoms now need to be transferred into the ring quadrupole trapping potential generated by the electromagnetic chip. This is performed in two steps, first the atoms are transferred from the initial magnetic trap into a minimum formed by the electromagnetic chip, visible in Figure–5.14 (panel xii) at coordinates $x = 20\,mm$ and $y \simeq 7.7\,mm$. This step sees the coordinated action of the coils of the PCB (its physical position is represented by the grey line at $y = 10\,mm$) together with initial contribution of the external coils, a possible sequence is illustrated Figure–5.14(i–xii).

The magnetic field forming the initial magnetic trap Figure–5.14(i) is situated $10\,mm$ below the PCB centred with the main chamber symmetry axis; in steps Figure–5.14(i–iii) using the external coils and the PCB tracks the magnetic trap is moved laterally to align with the axis of symmetry of the electromagnetic and

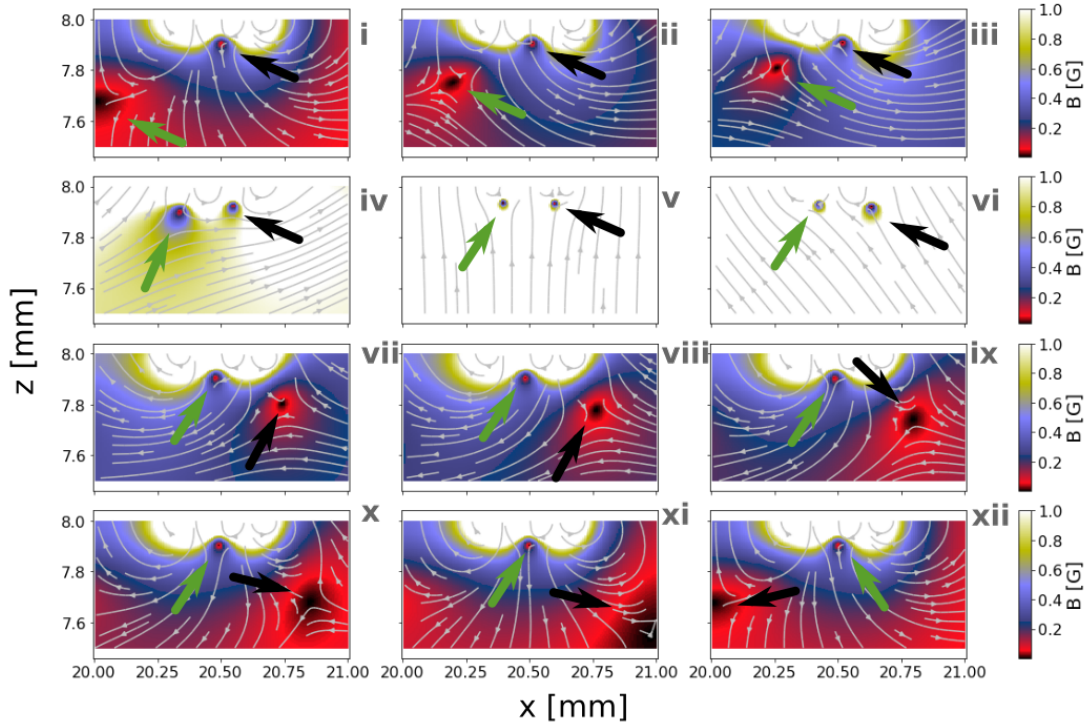


Figure 5.16.: Field magnitude and lines of the magnetic field in proximity of the electromagnetic chip during the second part of the loading sequence. The panel label refer to the points marked in the external field diagram trajectory shown in Figure–5.15. The position of the minimum containing atoms is indicated by the green arrow, while the black arrow marks the position of the empty minimum. Initially the empty minimum corresponds to the ring quadrupole, while the one containing atoms is located on the axis of symmetry of the ring further away from the surface of the chip. At the end of the sequence the positions of the two minima are exchanged.

radio–frequency chips. In steps Figure–5.14(iv–viii) the magnetic trap is formed using only coils sitting in the PCB, progressively compressing and approaching the electromagnetic chip (pictured as the yellow region, easily visible in insets Figure–5.14(vii–xii)); from stage Figure–5.14(xi) the electromagnetic chip is run at a current of $0.5A$, forming four other minima (two of which are visible in the region about its surface, while the other two are too small to be seen). Pushing the minima containing the atoms closer to the electromagnetic chip Figure–5.14(x–xi) causes two of the four additional minima to move laterally towards infinity; finally, in inset Figure–5.14(xii) only the electromagnetic chip runs a non zero current, the atoms are loaded into the central minimum.

In the second step the atoms loaded in the central minimum need to be loaded into the ring quadrupole. This is achieved using a series of combinations of radial and vertical fields to cancel the field produced by the electromagnetic chip along the desired trajectory. This must end up with both the external applied fields being zero. A possible solution is to follow circular curves in the radial and vertical field diagram, starting and ending with zero fields as shown in Figure–5.16. This procedure causes the central field minimum filled with atoms and the ring quadrupole initially empty to swap roles without merging as shown in Figure–5.16(i–xii).

The only element in the setup able to produce radial field in the region of interest is the radio–frequency chip that will be used with continuous current at this stage. The vertical component of the field can be easily generated by a single or a pair of coils of the PCB.

5.6. Rate Table

To imprint a rotation on the sensor, for both setting a rotation to be measured and being able to compensate for the Earth rotation, a rate table has been built. This consists of a spindle mounted on an air bearing Loadpoint–Bearings–D09820 moved by a tri–phase brush-less motor Aerotech S-180-44-A.

The rotary unit contains a high precision optical encoder formed by a double scale ring[2] $103\,mm$ large and a read head[3]. The optical encoder is interfaced to a

[2]Model RESM–20U–S–A–103 from Renishaw.
[3] Model SiGNUM–SR–010–L from Renishaw.

Soloist–ML controller that can be programmed remotely through the Local Area Network (LAN) using Soloist proprietary software on a Windows machine. This software uses a proprietary scripting language based on BASIC to program the motion of the axis. Furthermore, it presents a scope–tool that allows to monitor parameters such as position and speed, as read from the encoder, and to compare the measured parameter with the programmed motion.

The combination of the single scale version of the encoder ring associated with the read head would allow for a digital resolution of $2\,arcsec \simeq 5.56 \times 10^{-4} deg$ according to technical specifications of the producer. The configuration used in our setup presents a double scale ring encoder, allowing resolutions down to fractions of arcoseconds. Moreover, the encoders value is read by a low noise analogue encoder interface Si–NN–0001, allowing for higher precision, using quadrature interpolation techniques. More detailed specifications were not provided by the producer, but in the following section typical performances recorded over two hours of observation at constant rotation speed are reported.

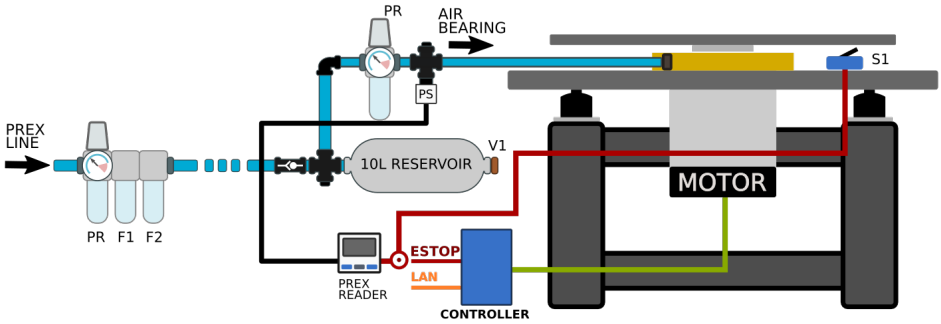
The motor is fixed to a steel plate of dimension $80 \times 40 \times 120\,cm^3$ placed on top of a standard optical table frame mounting PWA074 passive mechanical isolators from Thorlabs efficiently damping frequencies above $10\,Hz$.

On the spindle of the motor an aluminium circular breadboard with diameter $70\,cm$ and $10\,mm$ thick is mounted to host the vacuum chamber and necessary optics. An image of the rate table under construction, showing also the state of the lab before re-arrangement in the configuration illustrated in Figure–5.2, is shown in Figure–5.17b.

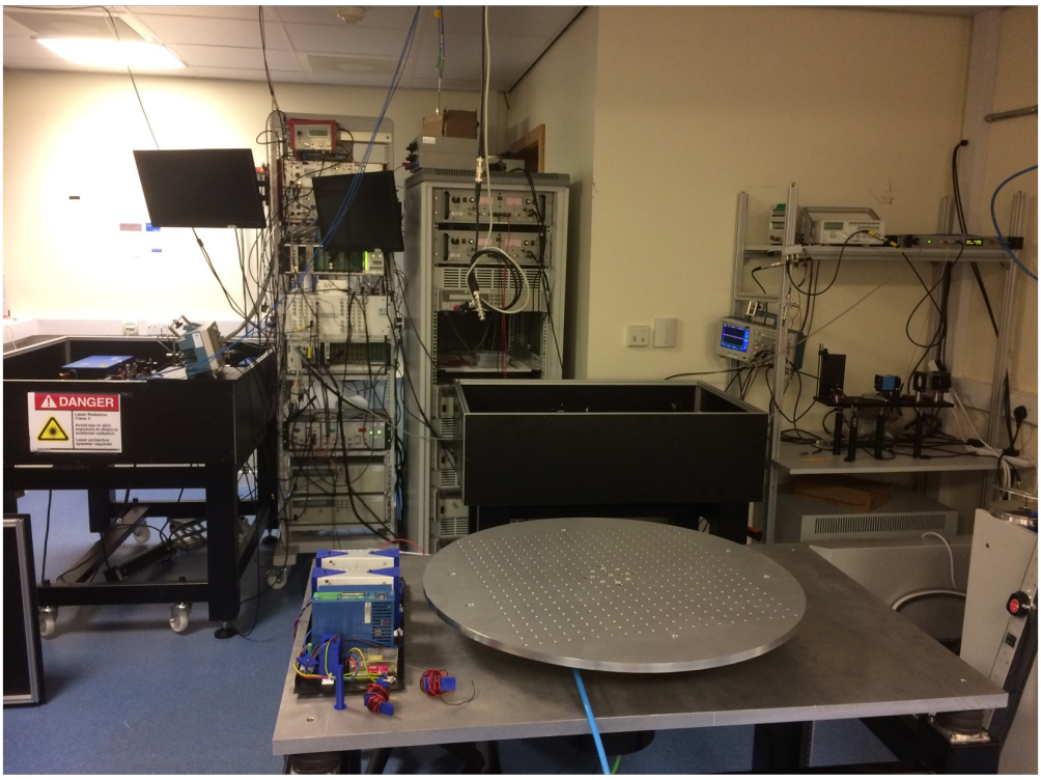
5.6.1. Rate table protection

The air bearing allows for high precision and smooth motion of the rotary axis. It is formed by a spindle, connected to the motor, and a drum to be mounted on the desired frame. When the system is fed with pressurized air, the spindle is allowed to rotate freely (if the motor is disabled) around its axis.

The pressure of operation is centred at $5.5\,bar$ with minimum and maximum limits at $5\,bar$ and $6\,bar$. The used air compressor is required by the producer to be oil–free and equipped with a desiccant air dryer, to prevent impurities to damage the bearing. The pressurized air needs to be filtered in three stages, with



(a) Scheme of the pressurized air system and protection of the rate table. List of used acronyms follows; PR: Pressure Regulator with filter 5 μm ; F1: Filter of 0.3 μm; F2: Filter of 0.01 μm; S: mechanical Switch; V: exhaust safe Valve; PS: Pressure Sensor.



(b) Picture of the laboratory showing the rate table, nearly completed in the foreground with its controller and power supply being assembled (blue and grey electronics placed on the left side of the table). In the background from left to right are visible: optical table A, rack A, rack B and optical table B as labelled in Figure–5.2. The position of the equipment has been successively re-arranged in the configuration according to Figure–5.2, after the completion of the rate table. The optical chamber is not present in the picture as it was momentarily placed on a side table out of the field of view on the left.

filter densities of $5\,\mu m$, $0.3\,\mu m$ and $0.01\,\mu m$ respectively. Also, a $10\,l$ air reservoir is required to be in the vicinity of the bearing to account for pressure fluctuations.

To satisfy these requirements, the system has been installed as described in Figure–5.17a. The pressurized air source is taken from the University pressure line, delivering desiccated air at a pressure up to $8\,bar$. The line is then fed to a first pressure–regulator and filtering stage installed on the walls of the laboratory area.

The filtered air is sent through a one–way valve isolating the pressure line from the pressure system installed directly on the table frame. The pressure system is composed of a $10\,l$ bottle, a second pressure regulator installed directly on the table and a digital pressure sensor placed just before the access to the bearing.

The pressure injected on to the on–table system is set to be at the maximum that the pressure line can provide. In this way, in case of pressure line fail, the system can benefit from the air reserve stocked in the reservoir to activate emergency routines. The pressure at the bearing is then set to specification requirements by the second pressure regulator.

The reservoir presents two ports, one of which is used for the input of the pressure line, while on the second a security valve is installed, releasing air when the pressure in the system exceeds $15\,bar$. This last precaution is anyway redundant, as each single element of the system is rated for pressures exceeding $20\,bar$ and the maximum pressure deliverable from the university line is $8\,bar$.

The spindle needs to be at rest in case the pressure drops below the specification requirements as friction might damage the internal finish of the bearing compromising its performance. Furthermore, on the rate table is mounted delicate equipment, such as optics and the vacuum chamber, connected with other appliances with cables and optical fibres. Therefore, it is necessary to make sure that a high speed of the motor is not accidentally commanded by a script and that the motor is not allowed to rotate for more than a revolution around its axis to avoid entanglement and breakage of wires and optical fibres.

The Soloist–ML controller presents an emergency stop (ESTOP) port that can be used to start a deactivating routine in case this channel is triggered. The logic of the port is fail safe, meaning that it is triggered when the voltage of the channel is zero, the ESTOP deactivating routine is started. The deactivating routine is defined through the soloist software, and it has been defined to decelerate the

rate speed down to zero and then disable the motor.

This feature is been used to make sure that the table is smoothly disabled when the pressure drops below requirements. A digital pressure sensor PSE540A-R06 is installed just before the input of the table. This is read by a SMC–PSE–300 controller presenting programmable output switch functionality. This has been set to output an ON signal only when the pressure read by the sensor is within the required limits. This signal is then connected to the ESTOP port through two mechanical switches placed on the table. These are always closed unless the table rotates out of a set interval for which the switches are pressed and opened. The switches have been placed such that the table is allowed a rotation range of about $270\,deg$.

5.6.2. Performances

To test the performances of the rate table, it has been programmed to run for two hours at the angular speed of $0.24\,deg/min$ and monitored at intervals of $1\,s$ for the entire period with the software Soloist scope–tool. This with fully mounted setup consisting of the vacuum chamber and necessary optics mounted on the chamber and on the circular breadboard. The difference between the commanded position and velocity and the corresponding values as measured from the encoder can be seen on Figure–5.17. The series of collected data see discrepancies between desired and measured values centred to zero, with two major disruptions and smaller perturbations occurring at almost regular intervals presenting similar recurring features. The two major disturbances at about $500\,s$ and $6.000\,s$ respectively, correspond to known accidental collisions with the table caused laboratory users. The smaller pseudo–regular disturbances last about $100\,s$ each and are suspected to be caused by pressure fluctuations occurring when the compressor activates to maintain the pressure of the line above specified levels. This possibility needs to be verified; unfortunately, the SMC–PSE–300 sensor reader does not provide a not Boolean output for the monitoring of the pressure other than the digital display, therefore this test is still to be done.

For experimental purposes, it is still possible to synchronize the monitoring of the table's motion with the experimental sequence. This would allow comparison of the rotations as measured by the encoder and the atomic gyroscope.

The count of points of irregular behaviour of the axis amount to the $14.67\,\%$ of

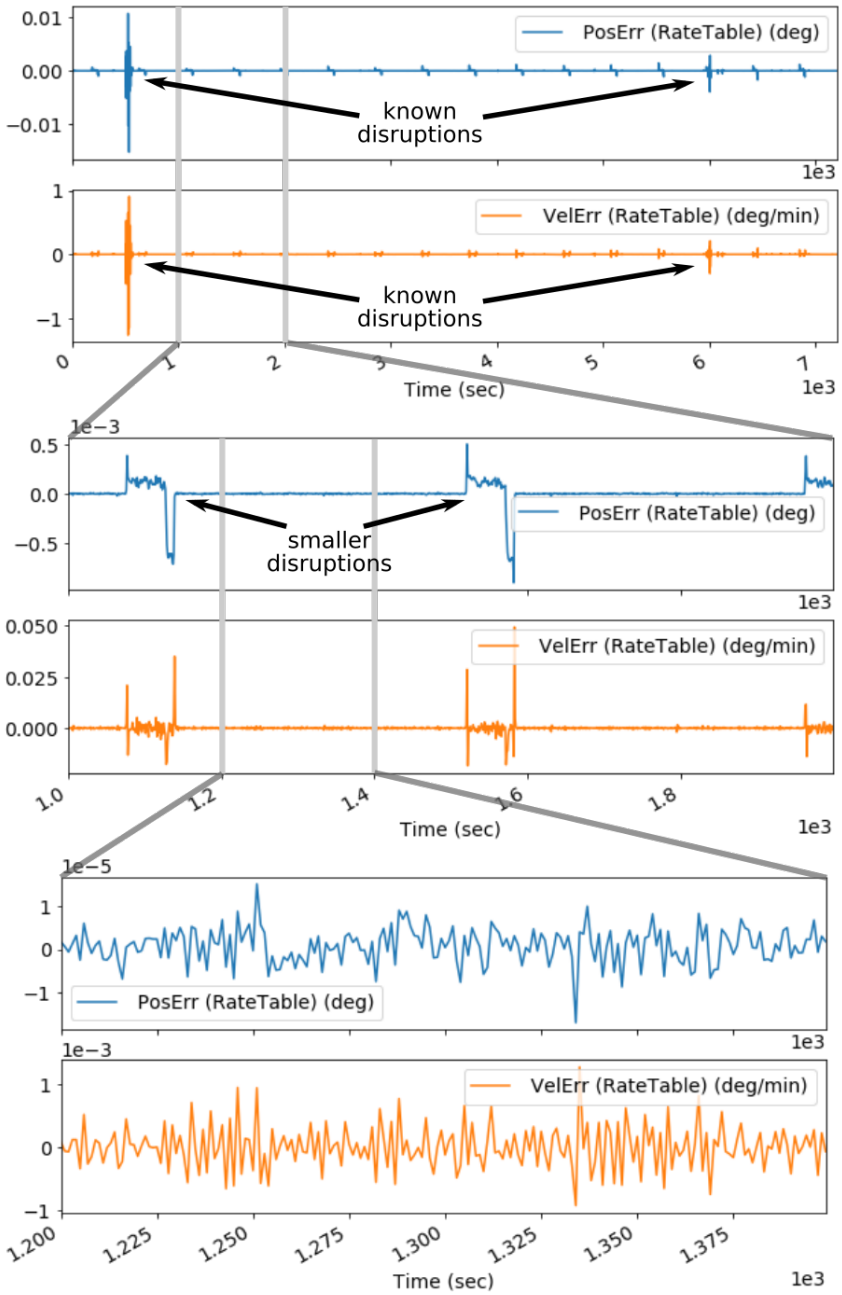


Figure 5.17.: Recording of the discrepancies between commanded and measured positions and speeds of the rate table over a period of about $2\,h$. On the top two graphs: two big discontinuities due to accidental shaking of the table are indicated with black arrows as "known disruptions". On the middle graphs: close–up on a period of $1000\,s$; smaller disruptions with similar features are evident. On the bottom two graphs, typical performance of the system when perturbations do not occur.

the sample. The remaining portion of recorded data see a mean position error of $7.5 \times 10^{-7}\,deg$ with a standard deviation of $3.92 \times 10^{-6}\,deg$, while the rotation rate sees an average discrepancy of $2 \times 10^{-6}\,deg/min$ with a standard deviation of $3.5 \times 10^{-4}\,deg/min$.

6. Experiments

The experimental setup described in the previous chapter has been used in an early stage experiment to load atoms in a ring trap formed using a permanent magnet situated on top of the vacuum chamber[1], assembled with a view port instead of the feed through flange on the upper port. This experiment had been carried out with the main purpose of demonstrating that it is possible to load atoms from an initial quadrupole magnetic trap into a ring shaped wave guide, i.e. validating the experimental feasibility of the starting point of the rf dressing scheme illustrated in Section–4.2.1. Furthermore, this allowed the tuning of the experimental setup, in preparation for the final configuration with the delivery of the atom–chip.

A second experiment, investigating a three–pulse Ramsey sequence, formally equivalent to the interferometric protocol described in Section–4.1.1, has been carried out. The experimental procedure utilizes a magnetic field oscillating in the microwave spectrum to perform π and $\pi/2$ pulses on radio–frequency dressed atoms. This experiment has been performed in another laboratory within the research group, equipped for investigation of microwave spectroscopy of ^{87}Rb. Details of the experimental apparatus can be found in [86] and [85].

6.1. Early stage experiment

The manufacturing of the chip designs and loading PCB described in Section–5.5 took longer than initially expected[2]. To make good use of the time and of the laboratory equipment, a preliminary experiment has been developed. This choice

[1] As it will be explained in the following section.

[2] The design of the chips were submitted for fabrication were submitted previous to the starting of my PhD in January 2015. At the time of writing, the assembled system described in Section–5.5.4 has not been delivered yet.

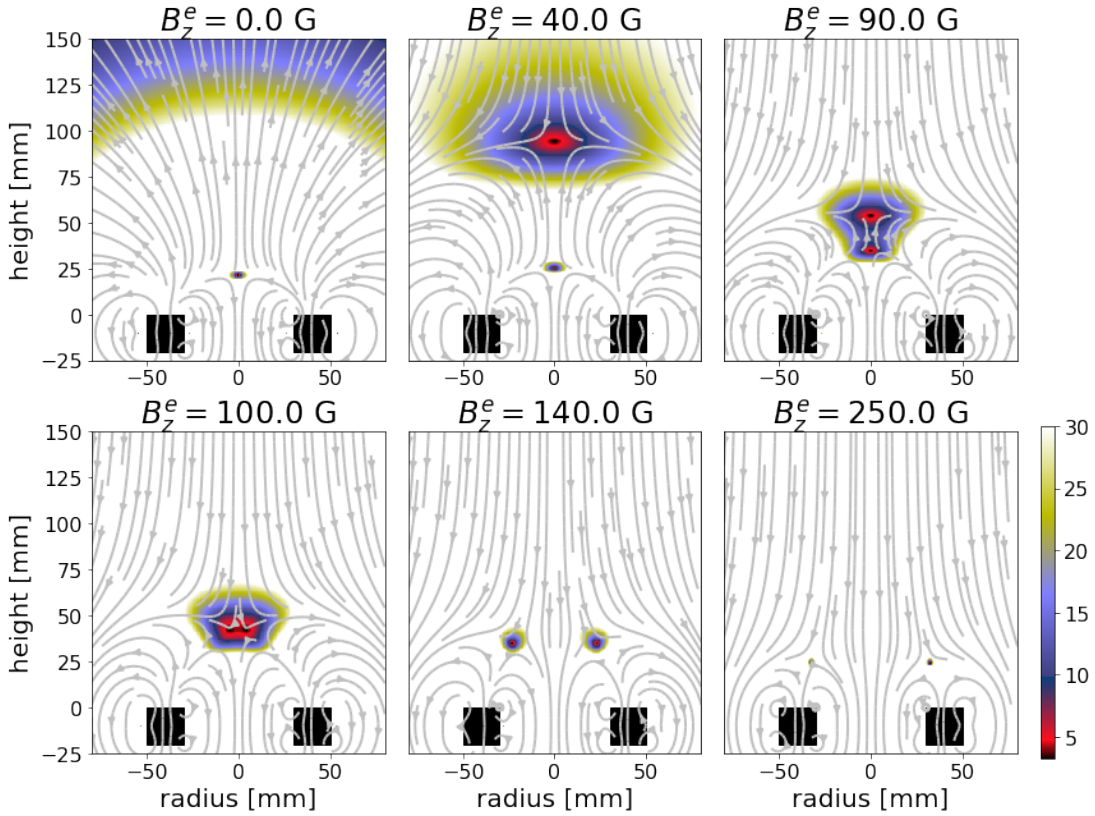


Figure 6.1.: Magnetic field of the permanent magnet (it section on the plane is represented by the two black squares) in presence of an external vertical magnetic field B_z^e pointing downwards with intensities in the range 0-250 G.

presented multiple benefits. First of all, it demonstrates the feasibility of changing the trap geometry from a simple quadrupole to the non trivial geometrical configuration, i.e. a ring trap, required for our guided interferometric protocol whilst maintaining the atoms confined during the entire process. Furthermore, it allowed me and other two PhD students (Thomas Bishop and later on Jamie Johnson) to acquire experimental expertise with the subject, it helped to optimize most of the experimental equipment and foresee technical issues.

The principal aim is to produce a ring-shaped magnetic trap using a circular permanent magnet and the two external coils at the top and bottom of the vacuum chamber. To understand how this is used to form a ring quadrupole consider the transverse section of the ring magnet used for this experiment, embedded in a uniform vertical field opposing it as in Figure-6.1.

When no external field is applied, a single high-gradient quadrupole is present on

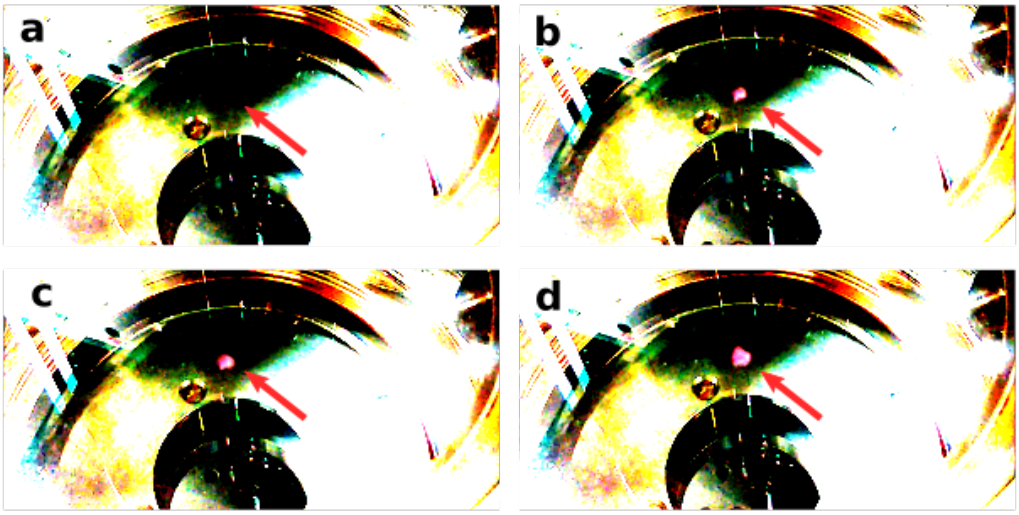


Figure 6.2.: Formation of a MOT (indicated by the red arrow) using the fields configuration depicted in Figure–6.1. The images were taken with a common smart-phone from the top window of the chamber (contrast and color saturation are augmented to enhance the visibility of the fluorescing atoms). In the background it is visible the aluminum structure holding the ring magnet. In figure (a) the MOT light is turned on and, in the remaining figures (b-d), the progressive accumulation of atoms for a total time of about $5\,s$ is clearly visible with the increasing size and brightness of the cloud.

the axis of symmetry of the magnet at a distance of $25\,mm$ from it. For weak vertical fields, a second quadrupole with lower gradient is formed along the same axis, at a further distance. Notice that the vertical optical access is granted by the shape of the magnet allowing to illuminate the quadrupole region with the cooler beam and re-pumping light for the formation of a MOT.

Increasing the amplitude of the vertical field causes these two minima to get closer to each other. Further increasing of the field magnitude results in the merging of the two minima and their splitting in the horizontal direction. This last scenario corresponds to a ring quadrupole, due to the cylindrical symmetry of the geometry. Ramping up to even higher magnitudes progressively increases the size of the ring, up to the limit case in which the quadrupole ring sits immediately above the ring magnet.

This shows that placing the magnet above or below the main chamber on the same axis of symmetry of the external coils can be used to generate all the magnetic fields necessary for the experiment, from the formation of a MOT to a magnetic

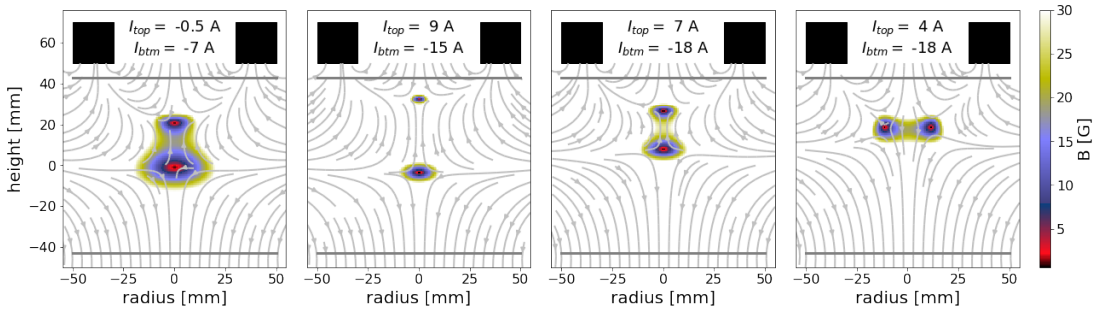
ring trap. With this configuration it has been possible to produce a MOT as documented in Figure–6.2. Successively, this has been modified for a design seeing the permanent magnet placed above the chamber instead, as there is a critical difference between placing the magnet above or below the chamber, because of the vertical merging of the two zeros in presence of gravity. When the magnet is placed below the chamber the merging of the two minima causes the atoms to fall from the upper minimum to the lower one. This results in an increase of the kinetic energy and high level of sloshing of the atomic cloud in the vertical direction compromising the capture of the atoms in the desired trap.

This effect is simply avoided, placing the ring magnet above the chamber. Indeed in this way the atoms are initially collected in the lowest potential minimum formed, merging at later times with a minimum placed above it, eliminating spillage of atoms from one minimum to the other one.

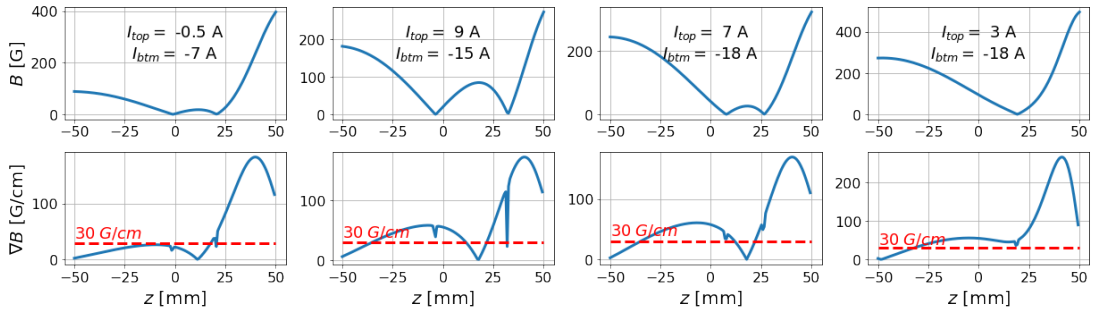
A typical experimental sequence comprises of the following steps:

1. The cooling and re-pumping transitions (also referred as MOT light) are turned on and the external coils are activated in an a–symmetric anti–Helmholtz configuration (i.e. running current in opposite direction with different amplitude). The resultant magnetic field corresponds to a weak quadrupole, that together with the laser light forms a MOT.
2. The MOT light is turned off (by means of mechanical shutters, followed by switching off the AOMs) and the current in the coils is configured such that a uniform magnetic field is formed in the location of the MOT. Simultaneously, an optical pumping pulse is shone on the cloud. This allows to accumulate atoms in the $|F = 2, m_F = 2\rangle$ state, requiring lower gradients for magnetic trapping ($15\,G/cm$ instead of the $30\,G/cm$ for the other trappable states) .
3. Atoms are recaptured into a magnetic trap in two stages, suppressing kinematic excitations due to the free fall of the atoms in the previous step.
4. The desired experiment is performed. This corresponds to each of the previous points in the list when optimizing the system or performing side measurements for the characterization of the trap. Ultimately, this consists of ramping up the external coils forming the desired ring trap.
5. An absorption imaging procedure is applied and the results stored.

Each of these step will be described with more detail in the next sections.



(a) Magnetic field amplitude and direction. The grey horizontal lines at a height of about $\pm 40\,mm$ represent the surfaces of the top and bottom view ports on the vacuum side, representing the geometrical constraint.



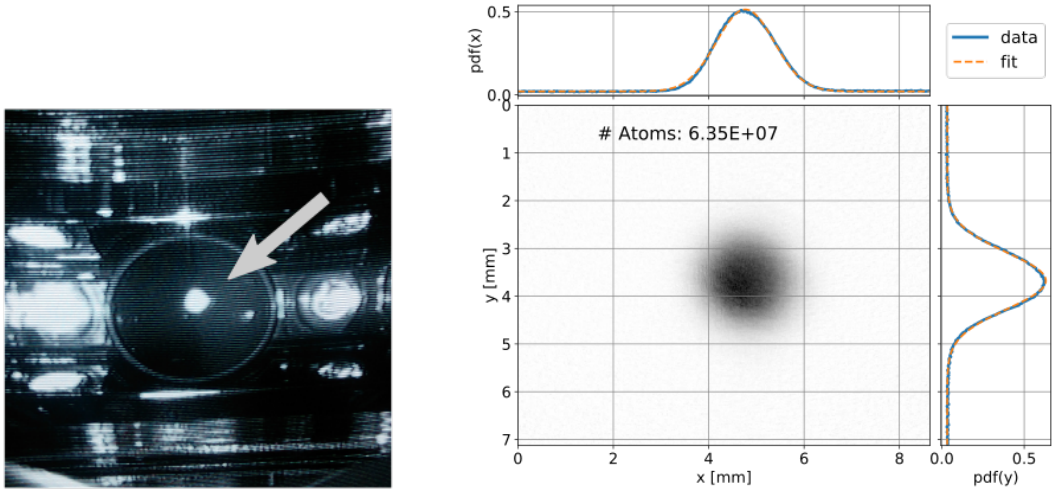
(b) Magnetic field amplitude and gradient along the axis of the minima, along the vertical direction. The red line on the lower panels marks the threshold of $30\,G/cm$ required to hold rubidium atoms in the $|F = 1, m_F = -1\rangle$ state against gravity (see Section–5.1.4 for further details).

Figure 6.3.: Magnetic field inside the vacuum chamber for different external coils' current configurations.

6.1.1. Magnetic fields: from MOT to ring

As mentioned in the introduction to this section, the magnetic fields produced by a ring magnet in combination with strong external magnetic fields can be used to produce all the necessary trapping fields for the experiment; from the formation of an initial MOT to a final quadrupole ring trap. Albeit, it is necessary to understand if all of the necessary physical configurations can be produced with the geometrical constraints of the experimental apparatus. Moreover, it is necessary to clarify if all of the field configurations can achieve the required gradients to overcome gravity.

In Figure–6.3, the field simulation inserting geometrical parameters of the setup are shown. It consists of the field provided by the two external coils, together with the loudspeaker magnet placed on top of the chamber, just above the top view port. The position of the magnet is hard to estimate with precision since



(a) Atoms fluorescing in a MOT (indicated by the light grey arrow) as imaged by a black and white camera from one of the side windows of the vacuum chamber.

(b) Absorption image of 6.35×10^7 atoms in a magnetic trap. On the side (top) graph the distribution of the sum by rows (columns) of the pixels of the image with corresponding Gaussian fit is presented.

Figure 6.4.: Atoms trapped in a MOT (a) and absorption image of atoms in a quadrupole magnetic trap (b) formed using a permanent ring magnet and the external coils.

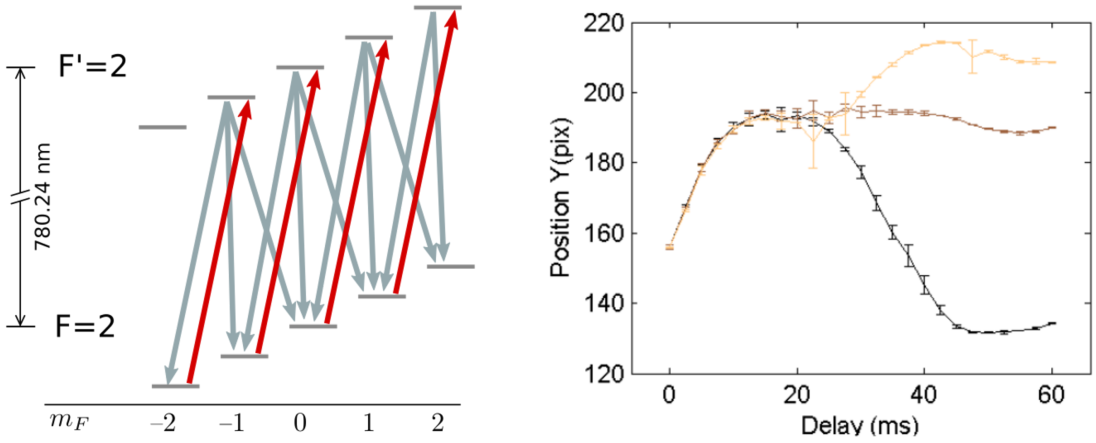
the glass–metal sealing of the view port presents a thickness and shape that is not specified from the producer and represents the limitation for the vertical placing of the magnet. A verisimilar distance of about $7\,mm$ between the lower face of the magnet and the in vacuum surface of the glass of the view port has been considered. The currents running in the top (bottom) coil is indicated in the figures as $I_{top(btm)}$, where positive values mean current circulating in anti-clockwise direction when seen from the top.

In Figure–6.3a, field intensity map and field lines are shown for different current configurations of the external coils. The position and dimension of the magnet is indicated by the black squares in place of its vertical section. The estimated positions of the in vacuum surfaces of the view ports are also indicated, as horizontal grey lines. The indicated current configurations show that it is possible to produce (from left to right): a MOT , a high gradient magnetic trap, merging of the two minima and ring trap; within the geometrical limits of the vacuum chamber. The fluorescing light scattered by atoms accumulated in a MOT formed with this scheme is presented in Figure–6.4a, while the absorption image of a magnetic trap is shown in Figure–6.4b. Figure–6.3b, illustrating the amplitudes and gradients

of the magnetic fields in the vertical direction aligned with the minima, shows that all of these configurations are compatible with magnetic trapping of all of the trappable states of the $5^2S_{1/2}$ level, requiring 30 G/cm to overcome gravity. Note that for the formation of a MOT this requirement is not necessary, as the presence of the light introduces further trapping forces that depend on the intensity and detuning of the cooling beam (see Appendix–A.3.1). Moreover, the usage of an optical pumping procedure accumulates atoms in the $|F = 2, m_F = 2\rangle$ state, requiring half of the gradient.

6.1.2. Optical pumping

At the end of the MOT stage an optical pumping procedure is operated, in order to obtain most of the atoms in the internal state $|F = 2, m_F = 2\rangle$. This is because the potential scales linearly with m_F (see equation (A.1)) and therefore atoms in the targeted states see potentials twice as high and twice as steep w.r.t. the other two trappable states, for equal fields.



(a) Optical pumping process.

(b) Recapture data.

Figure 6.5.: 6.5a A beam of light with the correct polarization drives σ^+transitions (red arrows) pumping atoms to states with higher m_F, spontaneous emission transitions are indicated with grey arrows. 6.5b: Graph of the vertical position (in pixel-counts from top to bottom, i.e. higher value means lower physical position) of the atomic cloud during recapture. The entire vertical scale (100 pixel at 33.6 $\mu m/pxl$) corresponds to 3.36 mm.

The optical pumping procedure, in ^{87}Rb, consists of applying a homogeneous mag-

netic field on the atoms together with a circularly polarized laser field propagating along the same axis of the magnetic field, resonant with the $F = 2 \rightarrow F' = 2$. The handedness of the laser depends on the mutual directions of the magnetic field and optical pumping, being right(left) handed if they are (anti–)parallel. The magnetic field defines the quantization axis and causes Zeeman splitting of the levels, both presenting positive Landé factors.

With the correct polarization, the laser radiation drives σ^+ transitions between the $|F = 2, m_F = m\rangle$ and the $|F' = 2, m_F = m + 1\rangle$ states, with $m \in [-2, 1] \cap \mathbb{Z}$. The atoms driven into the excited states $|F' = 2, m_F = m'\rangle$ decay, due to spontaneous emission, into the $|F = 2, m_F = m' \pm l\rangle$ $l \in \{0, 1\}$; apart from the $|F' = 2, m_F = 2\rangle$ that can only decay into the states $|F = 2, m_F = m' - l\rangle$. This generates a cascade of transitions accumulating atoms into the state $|F = 2, m_F = 2\rangle$ as illustrated in Figure–6.5a. To make the process effective, the re-pumper frequency is also shone on the atoms, making sure that all the atoms are pushed in the $F = 2$ manifold.

Normally, in cold atoms experiments, this procedure is performed releasing the atoms from the MOT and running the external coils in Helmholtz configuration. Simultaneously, the required laser light is shone on the atoms to initiate the cascade process. Then a re–capture procedure is performed, to collect the atoms in a magnetic trap.

In this particular experimental setup, this procedure becomes more complicated, since it is not possible to "turn–off" the permanent magnet and inserting a pulling or nulling coil would reduce if not completely obstruct the already reduced optical access.

The presence of the permanent magnet impedes the application of a highly uniform magnetic field. This causes the quantization axis not to be defined in a single direction. Also, the inductance of the solenoids limits the speed at which the magnetic field can be configured. Thus presenting small variations during the optical pumping. Experimentally, best results have been obtained switching off both of the external coils, obtaining a region of homogeneity of the fields in the centre of the chamber as visible in the leftmost diagram in Figure–6.6. The typical total duration is about 1 ms with an observed increase of atom number up to three times, after a holding time of 300 ms in a $15\,G/cm < |\nabla B| < 30\,G/cm$ magnetic trap.

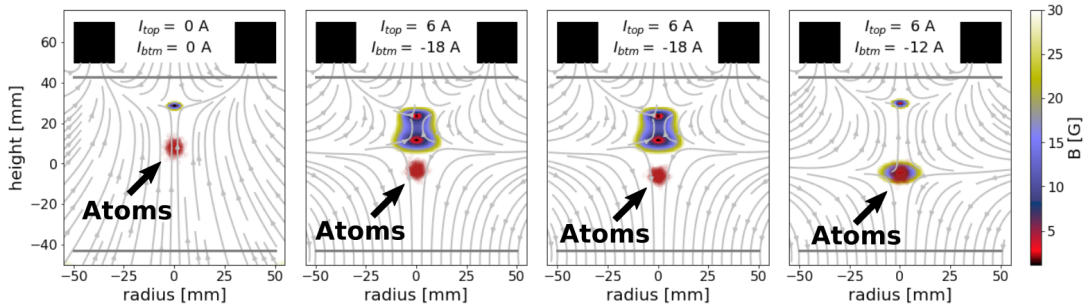


Figure 6.6.: Recapture procedure (from left to right): the position of the atoms, indicated by the red cloud, in free fall during optical pumping; a magnetic trap is formed just above the atomic cloud, decelerating its fall; the atoms reach the lowest point in the trajectory, presenting reduced speed in the vertical direction; the center of the quadrupole is moved in correspondence with the atoms.

6.1.3. Recapture

During the optical pumping stage atoms are in free fall, it's therefore necessary to implement a sequence that recaptures atoms into a quadrupole trap without exciting breathing modes. This is done in three sub-steps as illustrated in Figure–6.6: first a quadrupole is formed such that its zero sits above the atomic cloud, decelerating the fall of the atoms. Successively, this configuration is kept for a period of time at the end of which the atoms stop falling and start accelerating towards the center of the quadrupole. At this moment the center of the quadrupole is shifted onto the position of the atoms.

This procedure is tuned experimentally. A magnetic trap is formed, after the optical pumping sequence, at the position of the original MOT. Experimental collections, see Figure–6.5b, show that after a period of about $18 \div 20\,ms$ the cloud fall reaches the lowest point, being fully decelerated. Then, the position of the quadrupole is changed at different heights and the position of the cloud imaged at different times to reconstruct its trajectory.

In Figure–6.5b, cloud trajectories using three different quadrupole positions are shown. The black curve shows the trajectory for a final quadrupole higher than the cloud's position. After the deceleration the atoms accelerate again towards the center of the quadrupole. The yellow curve shows cloud trajectory for a final trap at a lower position w.r.t. the position of the atoms. The atoms keep accelerating towards lower positions. Finally, in the brown curve the final trap is

correctly placed at the location of the atoms, resulting in a successful recapture.

6.1.4. Temperature estimation

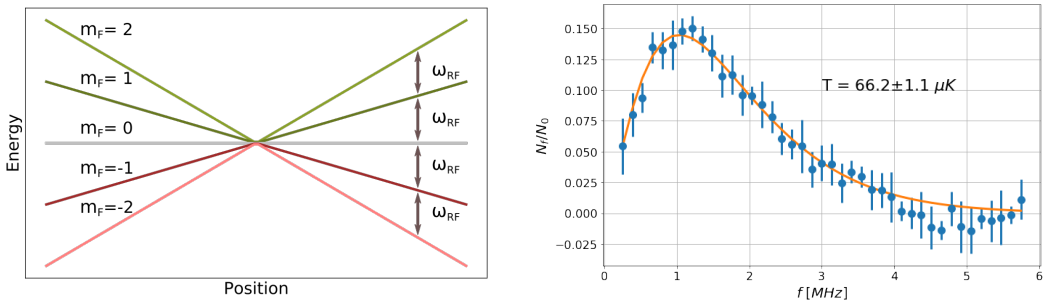
In cold atom experiments, a widely used technique to measure the temperature of the cloud is using the time of flight expansion of the cloud. Atoms are released from the trap and imaged at different times. The rate of expansion of the cloud is then related to the medium kinetic energy of the atoms and consequently, to its temperature.

In this experimental configuration free expansion is not feasible, due to the presence of the permanent magnet. Instead, a radio frequency spectroscopy technique is used. Similarly to radio-frequency evaporative cooling techniques, a field oscillating at the radio frequency regime is radiated on the atoms, causing a cascade of couplings from the $|F = 2, m_F = 2\rangle$ to non-trappable states as shown in Figure–6.7a. Depending on the frequency ω_{RF} of the field, the different Zeeman sub-levels are coupled at different static field values B according to $\hbar\omega_{RF} = g_F\mu_B B$. Note that this is independent of the state of the trapped atom, as for selection rules only transitions with $\Delta m_F = 1$ are allowed.

In a magnetic trap, for which the magnetic field B varies with the distance from the centre, each frequency ω_{RF} couples a specific surface of resonance corresponding to a certain trap depth. As for evaporative cooling, only the atoms presenting kinetic energy equal to or higher than $E_k = m_F\hbar\omega_{RF}$ can reach that resonant surface. Moreover, atoms with kinetic energy equal to E_k are expected to spend most of the time on the resonant surface. As all the kinetic energy has been spent to reach that specific potential energy.

Conversely to evaporative cooling, where the objective is to remove atoms with energy equal or higher than $\hbar\omega_{RF}$, it is of interest to remove only the atoms with energy equal to $\hbar\omega_{RF}$. For this to be valid, the power of the radio frequency is chosen to be very small, such that the atoms with sufficient kinetic energy can pass through the resonant surface. It can then be assumed that the atom loss for a specific frequency is proportional to the number of atoms having equivalent kinetic energy.

In this way, measuring the portion of atoms lost N_f/N_0 (where N_0 is the number of atoms detected when no radio frequency field is shone) at a specific frequency $\omega_{RF} = 2\pi f$ and repeating the measurement for different frequencies within a



(a) Radio frequency coupling in a linear trap.

(b) Measured and fitted rf–spectrum.

Figure 6.7.: On the left: the potential energies for states with different m_F in a linear trap. At any position the energy of the state is equal to $E = m_F \hbar \omega_{RF}$. On the right: an example of measured energy distribution of atoms fit with a Maxwell–Boltzmann distribution.

certain range, it is possible to reconstruct the energy distribution of the atoms. The measured distribution of atoms lost can then be compared to the Maxwell–Boltzmann distribution,

$$\rho_E\left(\hbar\omega_{RF}\right) = \left(\frac{m_F \hbar \omega_{RF}}{\pi k_B T}\right)^{d/2} e^{-\frac{m_F \hbar \omega_{RF}}{k_B T}}$$

where d is the dimensionality of the trap. This is only valid for thermal atoms, with temperatures well above the critical temperature of condensation, which is the case for this experiment where no cooling other than the MOT is applied.

In the experimental setup, the radio frequency is added using a home coil antenna, composed by two wires twisted together forming a coil presenting 5 pair of loops in a one-to–one transformer configuration. One of the circuits is terminated by a $50\,\Omega$ resistor , while the other is driven by a programmable function generator. The antenna is then placed on top of the chamber, as close as possible to the view port and on the same axis of the ring magnet. Experimental measurements have been carried out spanning $\omega_{RF} = 2\pi f$ between $2\pi \times (0 \div 6)\, MHz$ in a magnetic trap previous to the loading in the ring. Typical measured spectra suggested temperatures in the range of $60 \div 70\,\mu K$, as showed in Figure–6.7b.

6.1.5. Results

As initially stated, the ultimate objective of this experiment is to be able to image a ring–shaped atomic cloud. The trap is gradually modified in a ring trap

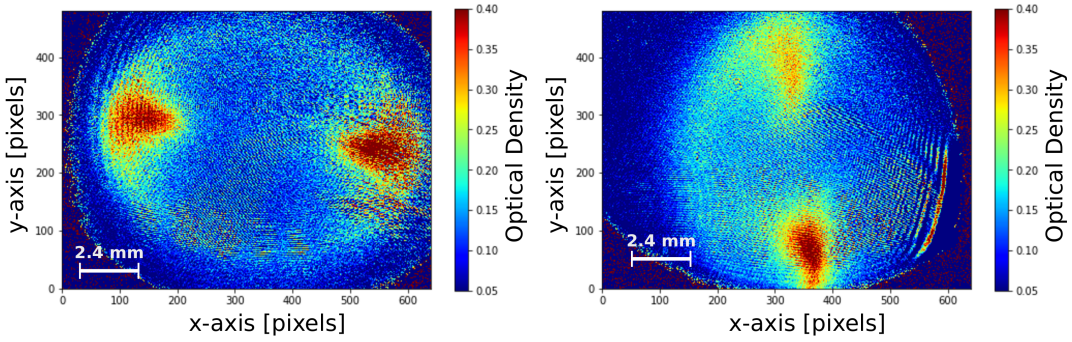


Figure 6.8.: Images of atoms trapped in a permanent magnet ring trap. A shallow (low atom density) ring shaped feature appears, but most of the atoms are collected on two main lobes. A rotation of the magnet results in rotated position of the lobes, indicating non homogeneous magnetization of the magnet.

as previously discussed and the atoms are detected through absorption imaging.

Data collected with this procedure led to imaging ring shaped clouds (Figure-6.8). Unfortunately all the images collected show low optical density on the quadrupole ring trap and present two pronounced lobes. The low density is due to the fact that for small radii (up to few millimetres) the energy difference between the central maximum and the surrounding minima is not high enough to observe a definite shape, while for larger radii (roughly a centimetre) the energy difference is sufficient, but the volume of the trap is very large reducing therefore the density of the cloud.

The two lobes where atoms tend to accumulate depend on non-homogeneity of the ring magnet magnetization. Rotating the magnet of an angle, corresponded with the rotation of the two lobes. We confirmed this performing field measurement around the magnet with a Hall magnetometer. The symmetric position suggests that they are due to fabrication processes therefore changing the magnet would probably not eliminate them. Indeed, performing the same measurement on various magnets showed the same non-homogeneity of the field. The presence of these two lobes affects also the cloud density in other regions. Tilting the table and correcting the inclination of the ring using external compensation coils can allow some other regions to be populated, but imaging of the full ring was unsuccessful.

In case a uniform ring was to be imaged, further investigation could have been explored. As, for instance, going to the next step of the scheme in Section–4.2.1

dressing the ring potential into a toroidal surface, using a second radio–frequency coil. Even if ultimately being unsuccessful, this experiment allowed to build the experimental setup with hands–on experience and spot few weakness that were present in the original design.

6.2. Three pulse Ramsey sequence

One of the issues that will need to be addressed for the implementation of the interferometric scheme illustrated in Section–4.1.1 is how to drive π and $\pi/2$ pulses on the atoms to implement the three pulse Ramsey sequence ($\pi/2$–π–$\pi/2$) forming the interferometric protocol. As illustrated in Chapter–3, various techniques have been used to this scope, from mechanical gratings to Bragg counter propagating beams, but all involving magnetic insensitive clock states (i.e. states presenting $m_F = 0$) that are not trappable. While, the interferometric protocol at the basis of this project involves the trappable states $|F = 1, m_F = -1\rangle$ and $|F = 2, m_F = 1\rangle$ of the $5^2S_{1/2}$ level of ^{87}Rb that are indeed trappable.

This experiment demonstrates a three–pulse Ramsey sequence between the two trappable states mentioned above. Meaning a sequence of three pulses of area $\pi/2$, π and $\pi/2$ respectively, separated by a free evolution period of duration T (see Fifure–6.9). This can be seen as a simulation of the interferometer, as it will be pointed out later on.

6.2.1. Theoretical model

The sequence addresses only two states at different energies, it is then meaningful to build the theoretical model on the two level atom scheme. The two states involved can be indicated with $|0\rangle$ for the ground state and $|1\rangle$ for the excited state, i.e. $|F = 1, m_F = -1\rangle$ and $|F = 2, m_F = 1\rangle$ respectively. These are separated by an energy $\hbar\omega_0$ corresponding, in the bare (non radio–frequency dressed) spectrum, with the hyperfine splitting $\hbar\omega_{hfs}$.

The Hamiltonian (in units of $\hbar$) describing a two level atom in presence of a driving field with Rabi frequency Ω_R, phase α and detuning $\Delta = \omega - \omega_0$ much smaller than the resonant frequency $\Delta \ll \omega_0$, can be written as [77]

$$\mathcal{H}_R^{\alpha} = \Omega_R \left(\cos\alpha\sigma_x + \sin\alpha\sigma_y\right) - \sigma_z\Delta$$

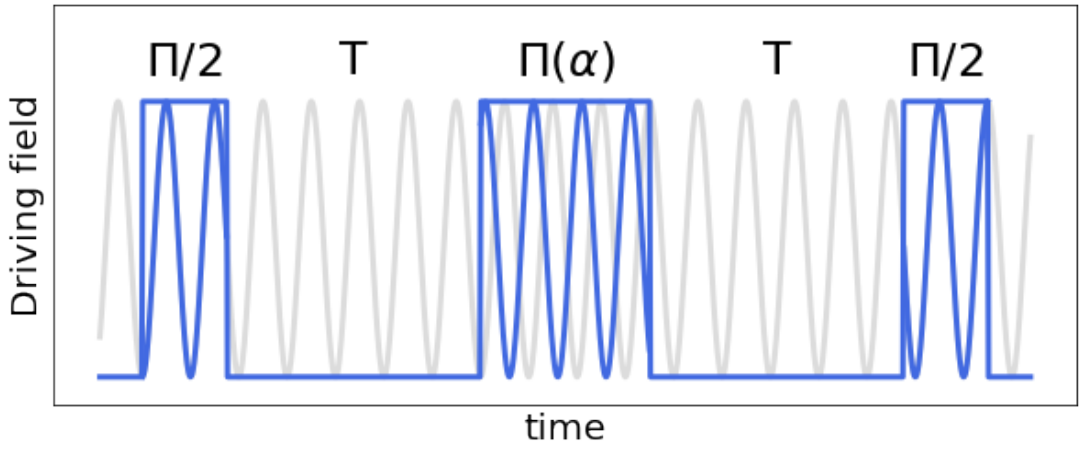


Figure 6.9.: Diagram of a three pulses Ramsey sequence with a free evolution period T and the central π–pulse presenting a phase α.

The evolution of an initial state for a time interval τ can then be easily computed using the evolution operator:

$$U^{\alpha}(\tau) = e^{-i\mathcal{H}_R^{\alpha}\tau}$$

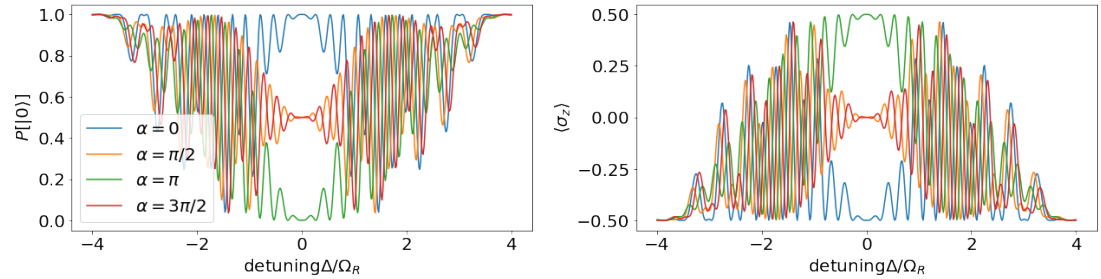
For a time interval $\tau_{\pi(\pi/2)}$ satisfying $\tau_{\pi(\pi/2)} \times \Omega_R = \pi(\pi/2)$ the evolution operator describes a $\pi(\pi/2)$–pulse with phase α; which, for shortness, will be abbreviated as $U^{\alpha}_{\pi(\pi/2)}$. An other case of interest is when no radiation is shone on the atoms, i.e. when $\Omega_R = 0$, corresponding to free evolution of the state, indicated as $U(\tau)$.

The effect of a three pulses Ramsey sequence $(\pi/2) \rightarrow (\pi) \rightarrow (\pi/2)_{\alpha}$on an initial state $|\Psi_0\rangle$ can then be calculated with

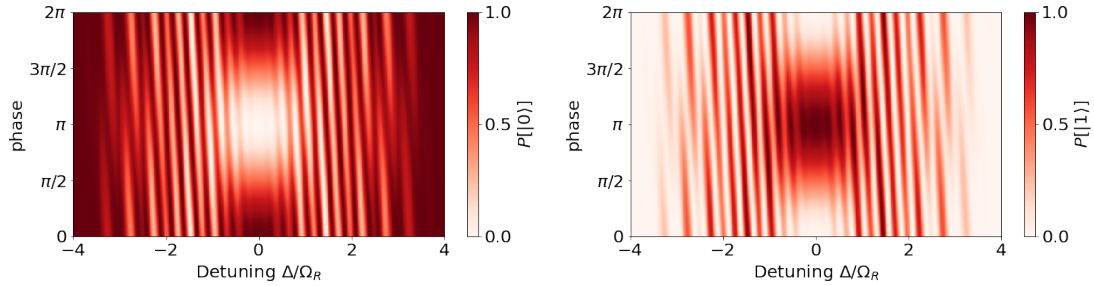
$$|\Psi^{\alpha}_{RS}\rangle = U^{\alpha}_{\pi/2} U\,(T)\, U^{0}_{\pi} U\,(T)\, U^{0}_{\pi/2} |\Psi_0\rangle$$

For a free evolution period $\tau = T$ separating the pulses. The introduction of a non–zero phase in the last term simulates an interferometer accumulating a phase α during the interrogation sequence.

Numerical solution of the model has been effectuated using the python library QuTiP (Quantum Toolbox in Python [98, 99]), expressing all the frequencies involved and time periods in units of Rabi frequency Ω_R and Rabi periods $1/\Omega_R$, with a free propagation time $T = 10/\Omega_R$, scanning the detuning in the interval $\Delta \in [-4\Omega_R, 4\Omega_R]$. The expectation values of measurables like the projection operator on one of the two states (i.e. the probability $\mathbb{P}[|0(1)\rangle]$ of observing an



(a) Three–pulses Ramsey fringes in the relative population of the state $|0\rangle$ and third component of the anguular momentum $\hat{\sigma}_z$.



(b) Probability of occupation for the states $|0\rangle$ and $|1\rangle$ in fuction of detuning and phase.

Figure 6.10.: Fringes in the three pulses Ramsey sequence for a free evolution period of $T = 10/\Omega_R$.

atom in the state $|0(1)\rangle$) and of the third component of the angular momentum $\hat{\sigma}_z = (|1\rangle\langle 1| - |0\rangle\langle 0|)/2$ present interference fringe patterns analogously to the two pulse case. The fringe patterns present null derivative region in the surroundings of $\Delta = 0$, with symmetric or anti–symmetric behaviour depending on the accumulated phase, as shown in Figure–6.10a. Computations for several values of the phase in the interval $\alpha \in [0, 2\pi]$ have been performed, producing the results illustrated in Figure–6.10b.

6.2.2. Microwave and radio-frequency dressing

As previosly stated, this work focuses on transitions between the $|F = 1, m_F = -1\rangle$ and $|F = 2, m_F = 1\rangle$ of the $5^2S_{1/2}$ level of ^{87}Rb. In [85] and [86] radio frequency dressed microwave spectroscopy techniques have been studied, both theoretically and experimentally, addressing this transition. Here, a brief summary of this technique is provided.

Consider ^{87}Rb atoms in a static field $\boldsymbol{B}^{(DC)} = B_0^{(DC)}\hat{\boldsymbol{e}}_0$. The presence of the static field breaks the degeneracy of the Zeeman sub-levels and defines a quantization

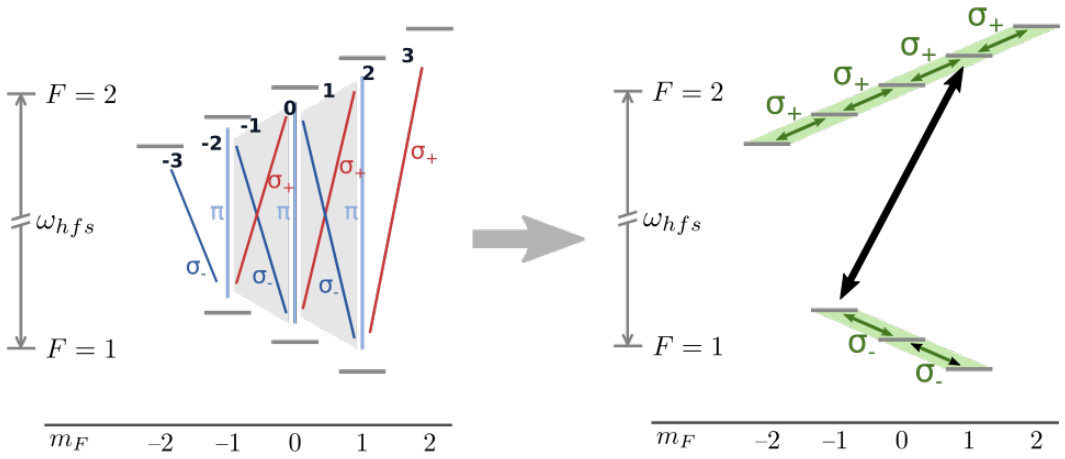


Figure 6.11.: Radiofrequency coupling allows transition between states of different manifolds otherwise forbidden. On the left allowed microwave transitions in the bare spectrum and their polarizations. Couples of degenerate transitions are highlighted with a shaded background and the labels l_{bare} are indicated with numbers in bold.

axis $\hat{\boldsymbol{e}}_0$. The energy difference between any of the sub–states of the $F = 2$ manifold and one in the $F = 1$ manifold following an allowed transition (i.e. satisfying the selection rule $\Delta m_F = m_F^{(F=2)} - m_F^{(F=1)} \in \{0, \pm 1\}$) is then given by

$$\begin{aligned} \Delta E_{bare}\left(m_F^{(1)}, \Delta m_F\right) &= \hbar\omega_{hfs} + \left(2m_F^{(1)} + \Delta m_F\right)\omega_L \\ &= \hbar\omega_{hfs} + \left(m_F^{(1)} + m_F^{(2)}\right)\omega_L \end{aligned}$$

where the Larmor frequency is defined as $\omega_L = \mu_B |g_F B_0^{(DC)}|/\hbar$, with $\Delta m = 0, \pm 1$ defining the polarization[3] of the transition as π, $\sigma_\pm$ respectively. The subscript "bare" indicates that this energy difference is relative to non radio frequency dressed atom energies.

Since there are three possible values for both the $m_F^{(1)} \in \{0, \pm 1\}$ and Δm_F, there are nine allowed transitions between the ground and excited manifold. Albeit, these correspond to only seven possible values of ΔE_{bare}, as $\Delta E_{bare}(-1, 1) = \Delta E_{bare}(0, -1)$ and $\Delta E_{bare}(0, 1) = \Delta E_{bare}(1, -1)$ (see Figure–6.11).

Hence, the resulting energy spectrum of the bare states presents seven equally spaced levels, centred on the hyperfine splitting $\hbar\omega_{hfs}$, with separation between

[3]It is formally incorrect to refer to π and $\sigma_\pm$ polarization, as this depends on the propagation direction of the wave. However, the concepts of $\pi, \sigma_\pm$–transition and linear, right(left) handed circular polarization are commonly confused in literature.

the lines corresponding to the Zeeman splitting $\hbar\omega_L$. In [85, 86] the levels are labelled according to their distance from the hyperfine splitting, i.e. using the label $l_{bare} = (\Delta E_{bare} - \hbar\omega_{hfs})/\hbar\omega_L$.

It is now possible to consider the effects of a magnetic field oscillating at the Larmor frequency on the bare spectrum. As pointed out in Section–4.2, only the field polarizations associated with $\sigma_\pm$ transitions contribute to the eigenenergies in the dressed picture, according to the sign of the Landé factor g_F. Specifically, for the states in the $F = 1\,(2)$ manifold, only the $\sigma_{-(+)}$component gives a contribution as they present positive (negative) g_F–factor (see Figure–6.11).

The resulting dressed energy can be written as $E^{1(2)}_{m_F^{1(2)}} = m_F^{1(2)} g_F \mu_B \sqrt{|B_{-(+)}|^2/2}$, or in terms of the Rabi frequency as $E^{1(2)}_{m_F^{1(2)}} = m_F^{1(2)} \hbar\Omega_{-(+)}/2$, with $m_F^{1(2)} \in \{0, \pm 1(, \pm 2)\}$. The value of the Rabi frequency, albeit being very close, differs in the two manifolds even for equal magnitude of the field in the case in which $|B_+| = |B_-|$. This is due to the fact that the g_F factors in the two different manifolds present a difference of $|\Delta g_F| \simeq \hbar/\mu_B \times 2\pi \times 2.75\,kHz/G$ in the first order in terms of static magnetic field, for fields smaller than $0.1\,G$, see Section–4.3 for further details. While these differences are not really significant in the bare spectrum, as they rise energy differences compared to the hyperfine splitting in the order of $\Delta E/\hbar\omega_{hfs} \approx 10^{-6}$ for low fields, they result in measurable effects in the dressed spectrum.

Notice that the associated eigenvectors are not the bare states of the manifold, but a superposition of them. Consequently, in the dressed picture, for any of the states of the $F = 1$ manifold there exists an allowed transition to any of the sub-states of the $F = 2$ manifold. The energy difference between two states in different manifolds amounts to

$$\begin{aligned}\Delta E_{dress}(m_F^1, m_F^2, l_{bare}) &= \Delta E_{bare} + m_F^1 \frac{\hbar\Omega_-}{2} + m_F^2 \frac{\hbar\Omega_+}{2} \\ &= \hbar\left(\omega_{hfs} + l_{bare}\omega_L + m_F^1 \frac{\Omega_-}{2} + m_F^2 \frac{\Omega_+}{2}\right)\end{aligned}$$

Since the possible values for m_F^1 and m_F^2 are three and five respectively, the number of possible energy differences amounts to 15 for each bare level. It is then convenient to divide the spectrum in seven different groups labelled accordingly to the bare spectrum, each of which contains 15 levels.

Experimental observations [85, 86] showed that in each of the groups, differ-

ent transitions are sharper then others and also the transition strength varies depending on the combinations of the parameters. The experiment has been performed using microwave transition in the first group, i.e. using $\sigma_{\pm}$ transitions, between the $m_F^1 = -1$ and the $m_F^2 = 1$ (identifiable with the triplet $(l_{bare}, m_F^1, m_F^2) = (1, -1, 1)$). This because, as observed in [85, 86] in this specific group the desired transition presents a sharp and pronounced peak. It is also worth mentioning that this technique is very convenient for the trapping scheme described in Section–4.2.1, as it is based on radio frequency dressing of the potential with atoms being accumulated on the resonant surface.

The energy of the chosen peak is almost coincident with the energy difference of the $(l_{bare}, m_F^1, m_F^2) = (1, 0, 0)$ and $(l_{bare}, m_F^1, m_F^2) = (1, 1, -1)$ transitions, observing that $\Omega_+ \simeq \Omega_-$. However, preparing the atoms in one single state is sufficient to select the desired transition. Specifically, in this experiment atoms are initially prepared in the $|F, m_F\rangle = |1, -1\rangle$ with a procedure described later on in the text. The static field amplitude is set to about $B_0 \simeq 260\, mG$ corresponding to a resonant Larmor frequency of $\omega_L \simeq 180\, kHz$ with a field amplitude of about $|B_{\pm}| \simeq 11\, mG$ corresponding to a Rabi frequency of $\Omega_{\pm} \simeq 8\, kHz$ the polarizations of the microwave field and of the radio frequency fields depend on their relative orientations with respect to the static field as will be discussed with more detail in the following section.

6.2.3. Sequence

This experiment has not been performed in the setup previously described in Chapter–5, but in another laboratory within the research group already equipped and calibrated for the study of interactions between matter and fields oscillating at microwave and radio frequency regimes. Detailed description of the apparatus can be found in [86]. Here, only the essential elements will be discussed.

As in the setup previously described, this apparatus is based on ^{87}Rb atoms. In addition, it presents an optical setup that provides also frequencies in the D_1 line range at about $795\, nm$. The vacuum chamber presents similar features of the one previously described when in use with the ring magnet, i.e. presents a view port on the upper port of the octagon providing full vertical access. Similarly, the static magnetic fields are provided by coils external to the chamber in the three spatial directions.

The oscillating magnetic fields in the radio frequency regime are provided by a coil antenna placed on top of the vacuum chamber, thus providing oscillations of the magnetic field in the vertical direction. The microwave magnetic field is provided by a horn antenna placed underneath the vacuum chamber, orientated such that the oscillation happens in the horizontal direction, perpendicular to the radio frequency field. To ease the description in the following text, the directions are defined such that: $\hat{\boldsymbol{z}}$ is parallel to the oscillation direction of the radio frequency field, i.e. the vertical direction; $\hat{\boldsymbol{x}}$ is parallel to the oscillation of the microwave field, in the horizontal plane; the $\hat{\boldsymbol{y}}$ direction is consequently defined such that $\hat{\boldsymbol{z}} = \hat{\boldsymbol{x}} \times \hat{\boldsymbol{y}}$.

Polarizations of the transitions The quantization axis, defined by the external coils, is always kept in the horizontal plane. In this way the radio frequency field is always linearly polarized perpendicularly to the quantization axis. As a consequence, it can always be decomposed in equal parts of right and left handed circular polarizations, hence providing $\Omega_+ \approx \Omega_-$. Also, this allows to have the microwave field parallel to the quantization axis (when only π transitions are required) as well as orthogonal (exciting exclusively σ_+ and σ_- transitions in equal parts) or intermediate direction (for which all the π and $\sigma_\pm$ are simultaneously excited).

To change the polarization of the transition driven by the microwave field within the same sequence (as required for this experiment), the following procedure is followed:

1. The horizontal static field is initially set accordingly to the desired microwave polarization, at a field magnitude of $B_0 \simeq 260\,mG$. The resonant radio frequency field is turned on at the frequency $\omega_L \simeq 180\,kHz$ and amplitude $|B_\pm| \simeq 11\,mG$ and the microwave field active at the desired frequency and amplitude.
2. The microwave field is turned off. The magnitude of the magnetic field is increased, breaking the resonant condition and re–oriented as desired, maintaining a field amplitude greater than B_0.
3. The field amplitude is decreased to the resonant amplitude B_0 and the microwave field turned on, accordingly to the desired operation.

A visual example of this procedure is illustrated in Figure–6.12a, changing the

microwave polarization from $\sigma_{\pm}$ to π as used in the experimental sequence, requiring π polarization for the state preparation and $\sigma\pm$ polarization for the Ramsey sequence.

State preparation As previously stated, the atoms need to be prepared in the correct state, to select the desired transition. The protocol used accumulates atoms in the $|F = 1, m_F = -1\rangle$ state at the beginning of the sequence as described below and illustrated in Figure–6.12b.

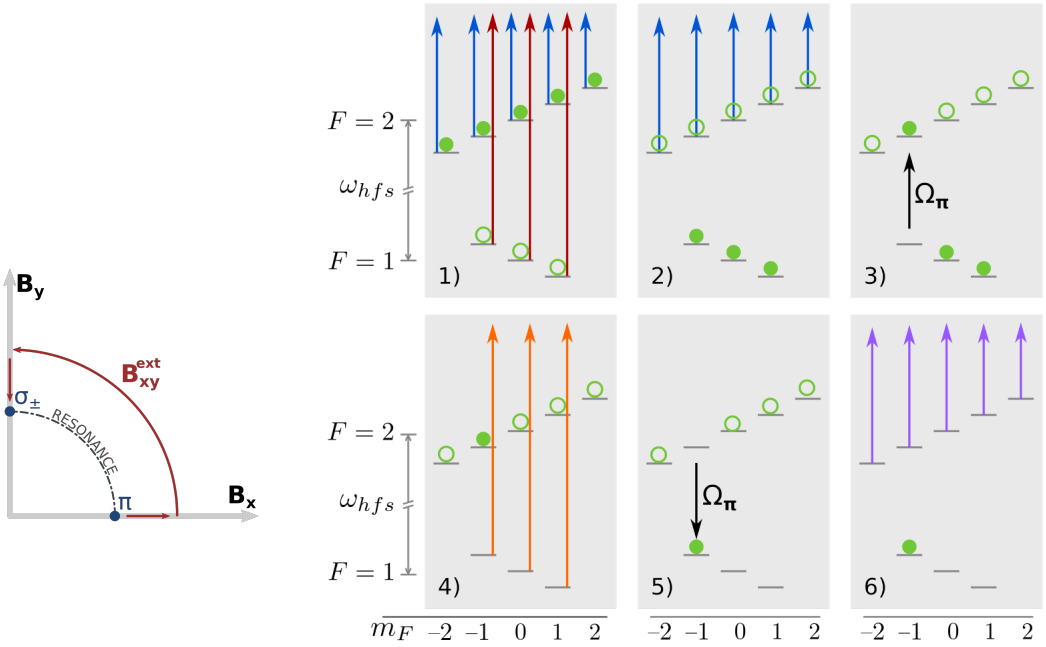
At the end of the MOT stage, most of the atoms will be accumulated among the sub-states of the $F = 2$ manifold. At this point the re-pumper light is switched off, causing the atoms in the cooling cycle to eventually fall from excited into the $F = 1$ manifold.

Successively, a first microwave π–polarized radiation illuminates the atoms for a duration of a π–pulse, causing the atoms present in the $|F = 1, m_F = -1\rangle$ to be raised into the $|F = 2, m_F = -1\rangle$ state. At this stage, a pulse of light resonant to the $F = 1 \rightarrow F' = 1$ transition of the D_1–line blows away the atoms remaining in the ground state of the $5^2S_{1/2}$ level. Another π polarized microwave π–pulse shifts the population of atoms in the $|F = 2, m_F = -1\rangle$ back into the $|F = 1, m_F = -1\rangle$ state and finally a light pulse resonant with the $F = 2 \rightarrow F' = 2$ of the D_2 line blows away the remaining atoms in the $F = 2$ manifold.

Once this operation terminates, the only atoms remaining are in the desired $|F = 1, m_F = -1\rangle$ state.

Microwave phase using I/Q modulation The microwave generator used (Rohde&Schwarz SMW200A) allows for I/Q modulation to introduce arbitrary control over the phase. This modulation technique utilizes two sinusoidal oscillators at the same frequency, presenting a phase difference $\pi/2$ between the two, representing the "In–phase" and the $\pi/2$ out of phase "Quadrature" signals. These are then summed together with desired intensity weights to generate a signal with desired arbitrary phase. A clear example is obtained considering the two signals as

$$I = A_I \sin \omega t$$
$$Q = A_Q \cos \omega t$$



(a) Change of the microwave transition polarization.

(b) State preparation.

Figure 6.12.: On the left: Change of the polarization of the microwave field from π to $\sigma_\pm$ re–orienting the quantization axis. On the right: illustration of the state selection protocol, starting with MOT phase(1); in (2) the repumper frequency is turned off; a first π–pulse (3) transfers atoms from $|F, m_F\rangle = |1, -1\rangle$ to $|2, -1\rangle$; a resonant beam cleans the $F = 1$ manifold (4); a second π–pulse (5) transfers atoms back into $|1, -1\rangle$ and a final resonant pulse cleans the $F = 2$ manifold.

which sum to $\Sigma_{I/Q} = A_I \sin\omega t + A_Q \cos\omega t$, representing the signal outputted by the device. An appropriate choice of the amplitudes of the two signals introduces an arbitrary phase $\phi_{I/Q}$. Indeed, selecting $A_I = A\cos\phi_{I/Q}$ and $A_Q = A\sin\phi_{I/Q}$ and using elementary trigonometric identities results in

$$\Sigma_{I/Q} = A\sin\left(\omega t + \phi_{I/Q}\right),$$

corresponding to the desired output with amplitude A and phase $\phi_{I/Q}$.

Detection scheme Two different beams, one blue–detuned with respect to the $F = 1 \to F' = 1$ and the second red detuned w.r.t. the $F = 2 \to F' = 2$ of the D_1 line. They are incident to a Wollaston prism at an angle of 30 *deg* such that

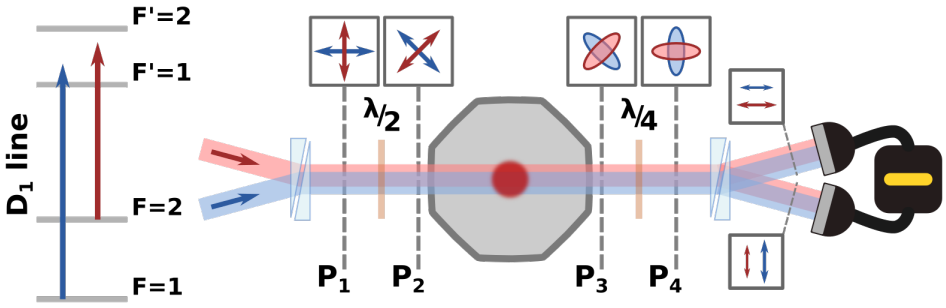


Figure 6.13.: Optical traces of the detection beams, with their respective frequencies in the D_1 line (color coded). Each of the beams traverses a Wollaston polarizer, a half wave plate, the atomic cloud in the vacuum chamber, a quarter wave plate, a second Wollaston prism splitting the orthogonal polarization towards the balanced photodetector. Their polarization at differenst stages is indicated in the square boxes ($P_1 \dots P_4$) and just before detection.

they are combined in the same direction with orthogonal linear polarizations (see Figure–6.13). A first half wave plate rotates the polarization, to form angles of $45\,deg$ with respect to their original polarization direction.

Each of the beams traverses the atomic cloud, embedded in a uniform field defining the quantization axis along one of the directions transversal to the propagation direction. This makes the atomic cloud a birefringent material for the incident beam, introducing an ellipticity in the polarization of the light. The light polarization is then analysed by means of a quarter wave plate, a second Wollaston prism and a balanced photodetector computing the difference of the signals.

If no atoms are present in the optical path, the linear polarization is converted into right or left handed circular polarization by the quarter wave plate. The beam intensity is then equally distributed in the two beams at the output of the second prism and the signals cancelled by the balanced photo detector. Conversely, when the light beam acquires ellipticity due to the presence of the atoms the right and left handed circular component are translated into horizontal and vertical components by the quarter wave plate causing an imbalance between the signals reaching the photo detector.

6.2.4. Results

The experiment has been carried out in the following way:

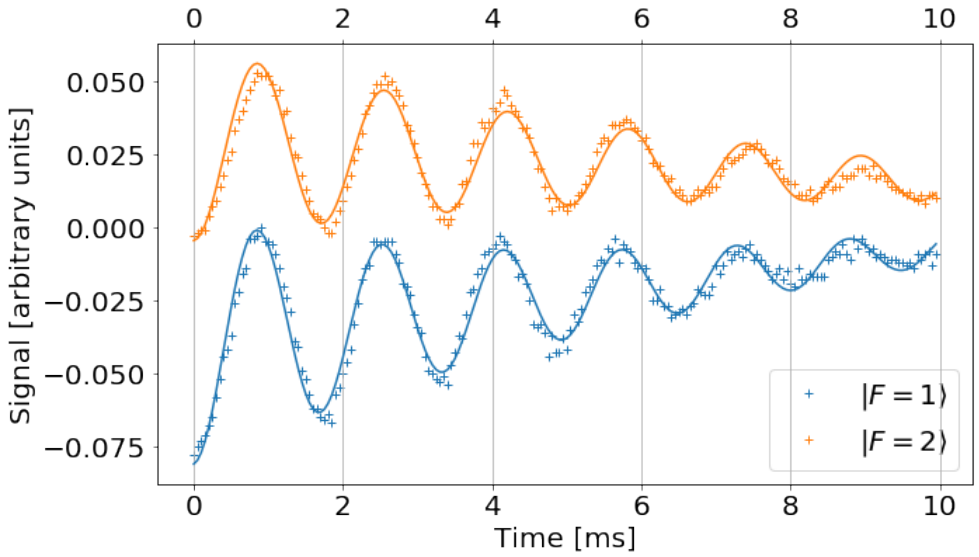


Figure 6.14.: Experimental observation of Rabi oscillations for the calibration of the duration of the pulses. Fitted curves are shown in solid lines.

An exploratory measurement is performed to estimate the Rabi frequency of the microwave radiation in the region of the atoms. Once the state preparation procedure has been carried out, the horizontal magnetic field is rotated to lie parallel to the y–axis, and the microwave field turned on.

This ensures that the linearly polarized microwave field is perceived by the atoms as an equal superposition of σ_+ and σ_- transition. The system is left in this configuration for a time interval $\tau \in [0, 10]\, ms$ after which the detection is performed. This sequence is then repeated for a different driving time in the interval.

Fitting of the data gives a Rabi frequency $\Omega_R^{|F=1\rangle} = 2\pi \times (543 \pm 3)\, Hz$ and $\Omega_R^{|F=2\rangle} = 2\pi \times (536 \pm 3)\, Hz$ for an average of $\Omega_R = 2\pi \times (540 \pm 4) Hz$, see Figure–6.14.

The measured points also show a liner increase of the frequency with time of $(\Omega_R^{|F=1\rangle})' = 2\pi \times (16.8 \pm 0.8)\, Hz/ms$ and $(\Omega_R^{|F=2\rangle})' = 2\pi \times (16.0 \pm 0.8)\, Hz/ms$ respectively for an average of $(\Omega_R)' = 2\pi \times (16.4 \pm 1.1)\, Hz/ms$. This might be caused by the trajectory of the atoms in free fall with respect to the horn antenna, i.e. the intensity microwave field might steadily increase along the trajectory. A possible alternative explanation consists of the presence of a magnetic field gradient along the trajectory of the atoms, increasing the effective Rabi frequency along the path.

From this it can be extracted that the Rabi period is about $\tau_{2\pi} = 1.85 \pm 0.01\, ms$

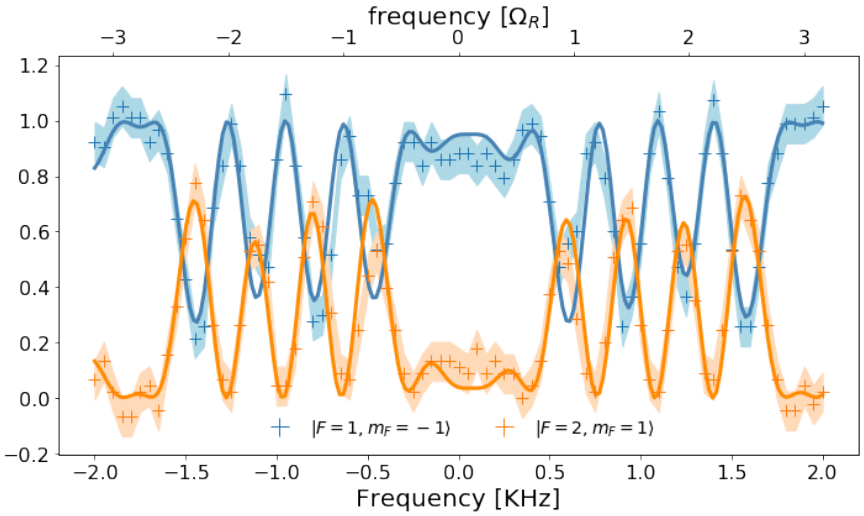


Figure 6.15.: State population in the $F = 1$ and $F = 2$ manifolds as a function of the frequency. The crosses indicate measured data with uncertainties indicated by the shaded region while the solid data indicates the fit of the model.

and consequently a duration of $\tau_\pi = 0.925 \pm 0.005\, ms$ for a π–pulse and half as much for a $\pi/2$–pulse. Also the signal presents damping with a halving time of about $t_{1/2} = 5.9 \pm 0.4\, ms$.

Once established the duration of the π and $\pi/2$ pulses, it is possible to set a free propagation interval. This is chosen to be $T = 1.5\, ms$ such that the entire sequence $T_{Ramsey} = 2T + \tau_{2\pi} = 4.85\, ms$ smaller than the halving time.

With this setting a three pulse Ramsey sequence has been performed. The frequency of the microwave field is scanned in the interval $\Delta \in [-2, 2]\, kHz$ around the resonant frequency with the phase of the last $\pi/2$–pulse set to zero.

Experimental normalized data for the relative state populations of this sequence with the relative phase is presented in Figure–6.15. The fit of the model on the data is also presented as continuous lines for the relative population of the two states.

The same procedure has been repeated with a higher microwave power, obtaining a π–pulse duration of $\tau_\pi = 0.740 \pm 0.05\, ms$. The free propagation duration had been chosen to be $T = 1\, ms$, obtaining a total duration of $T_{tot} = 3.48\, ms$. Both the frequency of the microwave in the surroundings of the resonant frequency and the phase of the last $\pi/2$–pulse have been scanned in the $\Delta \in [-2, 2]\, KHz$ and $\alpha \in [0, 2\pi]$ intervals, respectively.

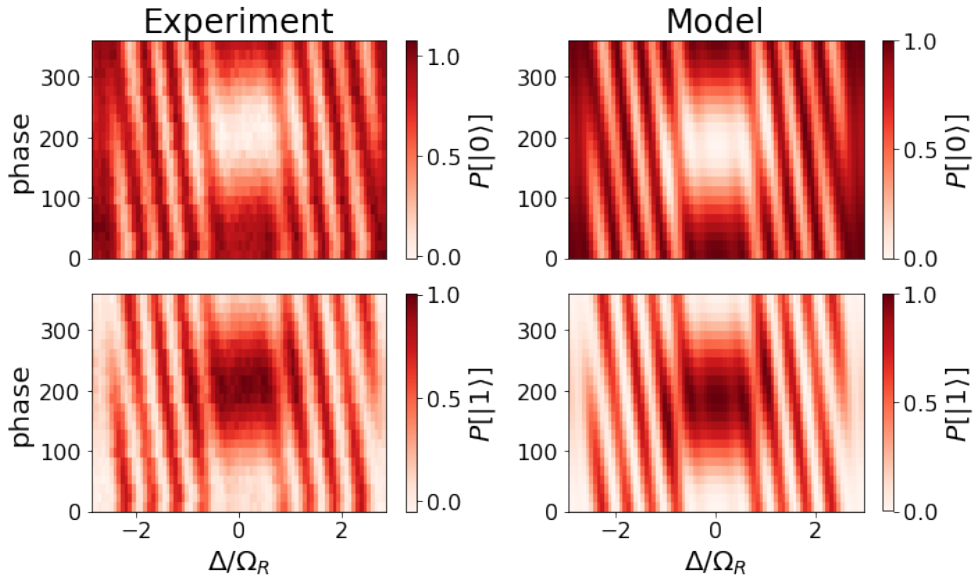


Figure 6.16.: Occupation probability for the ground and excited state as a function of the detuning Δ and phase as measured in the experiment (on the left) and predicted from the model (on the right). The model and the experimental data present the same features apart from a translational difference in both the phase and central frequency. The weak dependency on the detuning Δ for microwave frequencies near to resonance ($\Delta = 0$), makes this region particularly suitable for the estimation of the phase accumulated over the interferometric sequence, as small deviations of the driving field frequency will not present large deviations of the read-out phase.

The data collected and the theoretical model for the three pulses Ramsey sequence with the equivalent parameters is presented in Figure–6.16. The measured data has been fitted and compared to the model on the right "row-by-row", i.e. comparing the results with equal phases.

An offset of the frequency of about $\Delta f_0 = f_0^{exp} - f_0^{mod} = (0.08 \pm 0.01)\Omega_R$ has been observed. This is only due to the fact that the central frequency has not been set with high precision in the experimental sequence. Also an offset phase emerges, of about $\Delta\alpha = \alpha^{exp} - \alpha^{mod} = (-0.29 \pm 0.06)\, rad$. The origin of this phase offset could be related to the increasing Rabi frequency as observed during the calibration procedure, i.e. due to static field or microwave amplitude gradients. Indeed, this would introduce imperfections in the π and $\pi/2$ pulses, leading to an overall phase shift. Alternatively, it could be due to imperfection of the I/Q modulation electronics.

The validity of the model is confirmed also by the free propagation interval that is set experimentally in the sequence. This, given the selected τ_π results in an estimation of the non-dimensional product $(\Omega_R \times T)_{mod} = 4.3 \pm 0.2$. The uncertainty coming from the fact that the setting of the π–pulse duration is based on the calibration procedure. The same parameter from the experimental data reads as $(\Omega_R \times T)_{exp} = 4.31 \pm 0.01$, when averaging on all the fitted curves of the scans.

These results demonstrate that it is possible to implement a three pulse interferometric sequence as described in Section–4.1.1 acting on the trappable states with $|m_F| = 1$ of the $5^2S_{1/2}$ of rubidium with a combination of microwave and radio frequency fields. Also, it provides a way to detect the phase accumulated in the interferometer, because, for resonant pulses, the population of each state follows a sinusoidal behaviour as a function of the phase accumulated.

Further investigation is required to implement this scheme in the guided Sagnac interferometer. First of all it is necessary to investigate the performance of this sequence in the trapped scheme. As in a trap the magnetic field and the quantization axis is not uniform across the cloud, different strategies to provide the correct microwave polarization need to be developed.

7. Ring lattices with multi-pole radio-frequency dressing

For large rings, the scheme presented in Section–4.2.1 suffers from lack of confinement strength in the toroidal direction θ. In fact, for purely geometrical reasons, the energy gradient $\partial_\theta U$ decreases with the radius of the ring R_0 when maintaining the trap depth constant.

The straightforward solution to this problem is to increase the number of minima along the toroidal direction maintaining the same trap depth, leading to a ring lattice, i.e. a finite uni-dimensional lattice with periodic boundary conditions. A lattice with n sites is achieved modifying the scheme presented in Section–4.2.1 modulating the radio frequency field generating the toroidal trap geometry with a multi-pole of order n instead of a uniform field. As it will pointed out later on in this chapter, this can actually be interpreted as a generalization of the scheme in Section–4.2.1 since a uniform field can be modelled as a dipole, i.e. a multi-pole of order $n = 1$.

This, not only allows for designs with larger interferometric area (and consequently, larger sensitivity), but also opens for more fundamental studies in the field of lattice theory.

Cold and ultra-cold atoms are a versatile workbench for the study of quantum phenomena. Among various applications, emerge their use as quantum simulators, i.e. systems emulating the behaviour of computationally infeasible problems. In this, ultra-cold atoms in optical lattices excel as source of simulators in a variety of disciplines [100]. For example, condensed matter physics, where the dynamics of strongly correlated particles [101] and new topological phases of matter [102, 103] can be simulated in optical lattices. Furthermore, they set a platform for the study of the thermalisation of quantum systems and out of equilibrium dynamics in the many-body regime [104], which are of great interest in the field of statistical physics.

As an alternative to optical lattices, periodical potentials can also be obtained using purely magnetic traps [105] suitable for atom chip designs. A recent proposal [106] illustrated how purely magnetic lattices can be generated with radio frequency dressed potentials. Advantages of using atom chip technology lie in the intrinsic mechanical stability and miniaturisability of the devices together with their high versatility [107, 108].

Closed 1D optical lattices were theoretically and experimentally demonstrated by Amico and collaborators in [109] and [110], introducing an experimental tool for testing 1D systems with periodic conditions, frequently used in the theoretical literature.

As in [106] the scheme presented in this chapter uses a dressing technique, with two oscillating fields at identical frequencies but different geometries. These oscillating fields are superimposed to a static quadrupole ring resulting in an adjustable, dynamically controllable, state-dependent, ring-shaped atomic lattice.

The number of sites in the lattice corresponds to the order of the multi-pole used and it is unbounded in principle. Furthermore, the radio frequency dressed lattice allows for state-dependent manipulation of trapped atoms, enabling the creation of larger virtual dimensionality encoded in internal atomic states. It is evident that this corresponds to a generalization of the previous scheme [51] as the uniform magnetic field can be modelled as part of a magnetic dipole, i.e. a multi-pole with order one.

7.1. Multi-pole fields

A magnetic field presenting $2n$ poles is defined to be a multi-pole of order n, sometimes referred to as $2n$–pole. The Cartesian field components of a planar $2n$–pole field can be expressed in terms of the polar coordinates $r = \sqrt{x^2 + y^2}$ and $\theta = \arctan y/x$ as [111]

$$\boldsymbol{B}^{(m)}(r,\theta) = C(n)\left(\frac{r}{R_{ref}}\right)^{n-1}\begin{pmatrix}\sin\left((n-1)\,\theta - na_n\right)\\ \cos\left((n-1)\,\theta - na_n\right)\end{pmatrix} \tag{7.1}$$

Where $C(n)$ is the field amplitude, R_{ref} is some reference radius which sets the geometric scale and a_n is the angle at which the field is rotated with respect to the x-axis.

It is then possible to select two orthogonal multi-pole fields of order n to describe an arbitrary multi-pole of the same order. Specifically, it is possible to consider the unit vectors $\hat{\boldsymbol{e}}_1^{(m)}$ and $\hat{\boldsymbol{e}}_2^{(m)}$, corresponding to the directions of the multi-poles (m) with $a_n = 0$ and $a_n = \pi/2n$ respectively, to build an orthonormal basis. This can eventually be completed in the tri–dimensional space by the unit vector$\hat{\boldsymbol{e}}_0^{(m)} = \hat{\boldsymbol{e}}_1^{(m)} \times \hat{\boldsymbol{e}}_2^{(m)}$ coinciding with the vertical direction $\hat{\boldsymbol{z}}$ (for a graphical representation for $n = 2$, see Figure–7.1a). Moreover, it is possible to construct a spherical basis $\{\hat{\boldsymbol{e}}_\pm^{(m)} = (\hat{\boldsymbol{e}}_1^{(m)} \pm i\hat{\boldsymbol{e}}_2^{(m)})\sqrt{2}\,(, \hat{\boldsymbol{e}}_\pi^{(m)})\}$, reading explicitly (using $\theta_n = n\theta$)

$$\hat{\boldsymbol{e}}_\pm^{(m)} = \frac{1}{\sqrt{2}}\left[\begin{pmatrix}\sin\theta_{n-1}\\ \cos\theta_{n-1}\end{pmatrix} \pm i\begin{pmatrix}-\cos\theta_{n-1}\\ \sin\theta_{n-1}\end{pmatrix}\right], \quad \hat{\boldsymbol{e}}_\pi^{(m)} = \hat{\boldsymbol{e}}_0^{(m)}$$

Hence, an arbitrary multi-pole field $\boldsymbol{B}_m$ can be written in terms of its spherical components $u_\pm = \boldsymbol{B}^{(m)} \cdot \hat{\boldsymbol{e}}_\pm^{(m)}$ as $\boldsymbol{B}^{(m)} = u_+\hat{\boldsymbol{e}}_+^{(m)} + u_-\hat{\boldsymbol{e}}_-^{(m)}$.

7.1.1. Amplitude variation across the torus

The amplitude of an ideal multi-pole field depends strongly on the distance from the centre. It is then necessary to evaluate the limits for which the multi-pole field can be assumed to be constant across the torus, i.e. to estimate the field amplitude variation ΔA across the minor diameter $\varnothing = 2\rho$ of the torus. As from equation (7.1), the amplitude of the multi-pole field A follows the behaviour

$$A \propto r^{n-1}$$

The derivative of the amplitude at the centre point of the torus R_0 then reads as

$$\frac{dA}{dr}\Big|_{r=R_0} \propto (n-1)\,R_0^{n-1}.$$

For which the change in amplitude ΔA follows $\Delta A \propto 2\rho\,(n-1)\,R_0^{n-1}$ to first order in r. The relative field amplitude variation across the minor diameter is then given by

$$\frac{\Delta A}{A}\Big|_{r=R_0} = 2\frac{\rho}{R_0}\,(n-1)\,. \tag{7.2}$$

This sets the scale for which it is necessary to account for field amplitude variations in terms of the ratio between the minor and major radius of the torus

ρ/R_0.

7.2. Coupling terms

To extend the treatment of [51] and Section–4.2.1, consider the geometry of the in–plane time dependent field to be a multi-pole of order n as previously described.

The corresponding coupling components for the potential written in equation (4.14) can then be calculated computing the scalar product $B_{\pm}^{(m)} = \boldsymbol{B}_m \cdot \boldsymbol{e}_{\pm}^{(l)} = u_+ \boldsymbol{e}_+^{(m)} \cdot \boldsymbol{e}_{\pm}^{(l)} + u_- \boldsymbol{e}_-^{(m)} \cdot \boldsymbol{e}_{\pm}^{(l)}$. Being

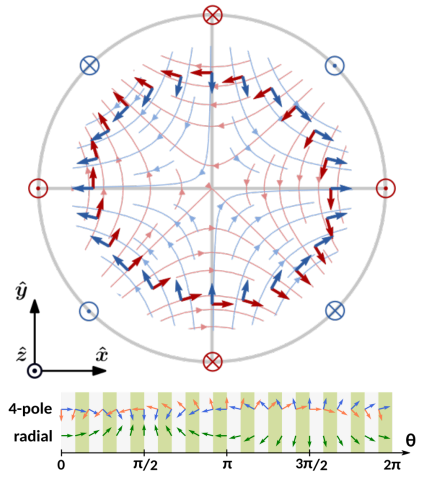
$$\begin{aligned}
\boldsymbol{e}_+^{(m)} \cdot \boldsymbol{e}_{\pm}^{(l)} =& \frac{1}{\sqrt{2}} \left[\begin{pmatrix} \sin\theta_{n-1} \\ \cos\theta_{n-1} \\ 0 \end{pmatrix} + i \begin{pmatrix} -\cos\theta_{n-1} \\ \sin\theta_{n-1} \\ 0 \end{pmatrix} \right] \cdot \boldsymbol{e}_{\pm}^{(l)} \\
=& \frac{1}{2} \left[\cos\theta_{n-1}\cos\theta - \sin\theta_{n-1}\sin\theta \right] (1 \pm \sin\phi) \\
&+ \frac{i}{2} \left[\sin\theta_{n-1}\cos\theta + \cos\theta_{n-1}\sin\theta \right] (1 \pm \sin\phi) \\
=& \frac{1}{2} \left(\cos\theta_n + i\sin\theta_n \right) (1 \pm \sin\phi) \\
=& \frac{1}{2} \left[\frac{e^{in\theta} + e^{-in\theta}}{2} + i\frac{e^{in\theta} - e^{-in\theta}}{2i} \right] (1 \pm \sin\phi) \\
=& \frac{1}{2} (1 \pm \sin\phi) e^{in\theta}
\end{aligned}$$

and similarly $\boldsymbol{e}_-^{(m)} \cdot \boldsymbol{e}_{\pm}^{(l)} = (1 \mp \sin\phi) e^{-in\theta}/2$, it is then possible to explicitly write

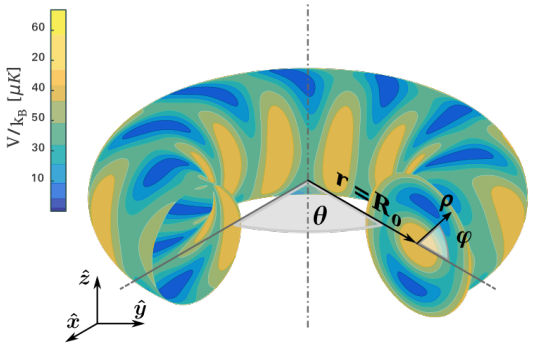
$$B_{\pm}^{(m)} = \frac{u_+}{2}(1 \pm \sin\phi) e^{in\theta} + \frac{u_-}{2}(1 \mp \sin\phi) e^{-in\theta}.$$

This term substitutes the term $B_{\pm}^{(p)}$ in equation (4.16) to generalize the treatment for the multi-pole case. The resulting potential using a toroidal $B_{\pm}^{(t)}$ coupling producing poloidal minima on top and bottom of the ring, i.e. using a phase between the circular components a and b of $\phi_{ab} = \pi/2$, and a multi-pole field with coupling field $B_{\pm}$ produces a toroidal potential analogous to the one illustrated in Figure–4.5 in Section–4.2.1, with the difference that the modulation produces n minima (i.e. equal to the order of the multi-pole) instead of only one, as seen in Figure–7.1b.

An interesting point of view for the understanding of this result comes from



(a) Orthonormal basis a quadrupole (top). Field windings for a quadrupole and a radial field (bottom).



(b) Potential landscape obtained using a modulating multi-pole of order $n = 10$. In this case, 10 sites are formed (dark blue regions). On the right, in the transverse plane the inset highlights the two regions of low potential at the top and bottom of the torus.

Figure 7.1.: On the left: two concentric quadrupole fields rotated one from each other of $\pi/4$. Each quadrupole is produced with four infinitely long wires parallel to $\hat{\boldsymbol{z}}$ carrying current directed out of (in to) the page at positions indicated by $\odot\,(\otimes)$. The set of arrows disposed along a circumference highlights the orientations of the two fields along a closed circular path. This is compared to the field direction of a field oriented along the radial direction in the bottom panel. On the right: the potential landscape for the coupling B_+ with poloidal minima at the top and bottom of the ring is shown, together with a representation of the coordinates.

comparison of the multi-pole field $\boldsymbol{B}_{TD}^{(m)}$ with the toroidal field $\boldsymbol{B}_{TD}^{(t)}$. The number of minima stems from the number of constructive and destructive contributions of these two fields, and since multi-pole fields present non–zero contribution only on the horizontal plane, we are only interested on the projection of the toroidal field on the same plane. Specifically, it is interesting to focus on the winding number w of these two fields, i.e. the number of anti-clockwise rotations windings of the field direction when following a closed anti–clockwise trajectory around the origin.

The winding number is easily understood when representing the magnetic field on a plane in terms of complex numbers as explained in Appendix–B. The expression

of a multi-pole field of order n in the complex number representation can be written as equation (B.9)

$$B^{2n}(\boldsymbol{z}) \simeq -ni\mu_0 \frac{I}{\pi R^n} \left(\boldsymbol{z}^\star\right)^{n-1}$$

were $\boldsymbol{z} \in \mathbb{C}$ corresponds to a Cartesian coordinate and $R \in \mathbb{R}^+$ is a geometric factor setting the size of the multi-pole antenna (see Appendix–B for details). In the same representation, the projection of the toroidal field is oriented radially and can be represented as $B^0(\boldsymbol{z}) \propto -i\mu_0 \frac{I}{\pi} \left(\boldsymbol{z}^\star\right)^{-1}$. Choosing a circular trajectory $\gamma(t) = R_0 e^{it}, t \in [0, 2\pi]$ with a fixed radius $R_0 \in \mathbb{R}^+$ the multi-pole field winds $-w_n = n - 1$ times clock wise, while the radial field rotates one time anti–clockwise, for a global winding number difference of $\Delta w_n = -n$, i.e. the two fields rotate n times clockwise with respect to each other. This means that the number of times that they point in opposite (equal) directions is equal to n, hence interfering destructively (constructively) n times along the closed trajectory. A scheme illustrating the effects of differences in winding number can be seen for $n = 2$ in Figure–7.1a.

7.2.1. Toroidal confinement

It is of interest to understand the effects of the multi-pole on the potential, in the toroidal direction θ. Recalling from equation (4.14) in Section–(4.2), the potential energy in the region where the resonant condition $B_0 = \hbar\omega / g_F \mu_B$ is met, reads as

$$E^{\pm}_{m_F}(\phi, \theta) = \frac{m_F g_F \mu_B}{\sqrt{2}} \left| B_{\pm}(\phi, \theta) \right|, \tag{7.3}$$

where $B_{\pm}(\phi, \theta) = B^{(t)}_{\pm}(\phi) + B^{(m)}_{\pm}(\phi, \theta)$, highlighting that the term $B^{(t)}_{\pm}(\phi)$ depends solely on the poloidal coordinate ϕ . As the force F in direction x is related to the potential U by $F = -\partial_x U$, the confinement force on the toroidal direction is given by (using $\partial_x |x|^2 = 2|x|\partial_x |x|$):

$$F_\theta = -\frac{m_F g_F \mu_B}{2\sqrt{2}\left| B_{\pm}(\phi_{\pm}, \theta) \right|} \partial_\theta \left| B_{\pm}(\phi, \theta) \right|^2 .$$

The modulus of the coupling strength can be written as

$$\begin{aligned}
|B_{\pm}(\phi,\theta)|^2 = \frac{1}{4}\left(|a|^2+|b|^2-2|a||b|\cos 2\left(\phi-\phi_{ab}\right)\right) \\
+\frac{1}{2}\left[\mp|a|\,|u_+|\cos\left(n\theta+\phi+\phi_{au_+}\right)(1\pm\sin\phi)\right. \\
\pm|b|\,|u_+|\cos\left(n\theta-\phi+\phi_{bu_+}\right)(1\pm\sin\phi) \\
\mp|a|\,|u_-|\cos\left(n\theta-\phi-\phi_{au_-}\right)(1\mp\sin\phi) \\
\left.\pm|b|\,|u_-|\cos\left(n\theta+\phi-\phi_{bu_-}\right)(1\mp\sin\phi)\right] \\
+\frac{1}{4}\left(|u_+|^2(1\pm\sin\phi)^2+|u_-|^2(1\mp\sin\phi)^2\right. \\
\left.2\,|u_+|\,|u_-|\cos\left(2n\theta+\phi_{u_+u_-}\right)\left(1-\sin^2\phi\right)\right)
\end{aligned}$$

Where the phase difference between two complex numbers z_1 and z_2 is indicated as $\phi_{z_1z_2} = \arg z_1 - \arg z_2$. The derivative along θ is then:

$$\begin{aligned}
\partial_\theta|B_{\pm}(\phi,\theta)|^2 = -\frac{n}{2}\left[\mp|a|\,|u_+|\sin\left(n\theta+\phi+\phi_{au_+}\right)(1\pm\sin\phi)\right. \\
\pm|b|\,|u_+|\sin\left(n\theta-\phi+\phi_{bu_+}\right)(1\pm\sin\phi) \\
\mp|a|\,|u_-|\sin\left(n\theta-\phi-\phi_{au_-}\right)(1\mp\sin\phi) \\
\left.\pm|b|\,|u_-|\sin\left(n\theta+\phi-\phi_{bu_-}\right)(1\mp\sin\phi)\right] \\
-n\,|u_+|\,|u_-|\sin\left(2n\theta+\phi_{u_+u_-}\right)\left(1-\sin^2\phi\right)
\end{aligned}$$

which clearly shows that the forces along the toroidal direction linearly increase with the order n of the multi-pole.

The derivative gives also the occasion to observe where the positions of the minima and maxima take place and appreciate how they depend on the relative phases between the fields. To simplify, consider the case in which the poloidal minima form at position $\phi_\pm = \pm\pi/2$, hence with $\phi_{ab} = \pi$. First of all, note that at the top (bottom) of the ring, i.e. $\phi = \phi_{+(-)}$, only the multi-pole amplitude $u_{+(-)}$ contributes to the formation of maxima and minima. Also notice that the relative phases between the toroidal and multi-pole radio frequency fields determine the positions at which the minima and maxima take place along the toroidal coordinate θ.

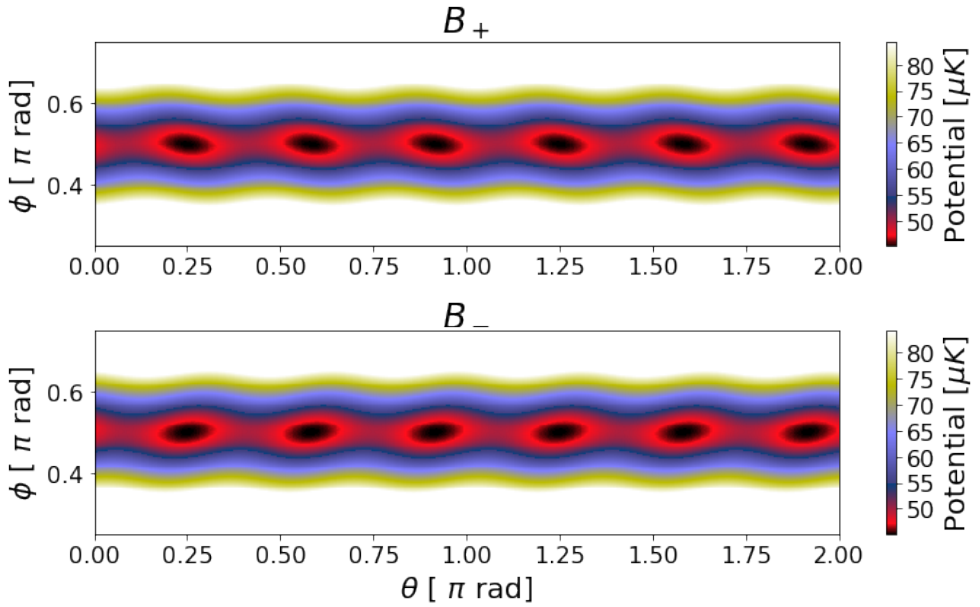


Figure 7.2.: Potential landscape for B_+ and B_- couplings, with $n = 6$ around $\phi = \pi/2$. The traps are not isotropic and present an angle with respect to the θ axis. Also the inclination of the traps is opposite for the two different couplings.

7.3. Geometrical considerations

As is evident from the the plot in Figure–7.2, the orientation of the traps presents a tilt. Moreover, the traps present opposite inclination for the B_+ and B_- couplings. This becomes an issue when operating an interferometer or whenever the overlap between states with opposite g_F factors is required.

Geometrically, two possible strategies can be followed to overcome this issue. The first one is to find sets of parameters for which the anisotropic wells are oriented along one of the two angular axes. While the second strategy is to find a combination of parameters for which the wells are isotropic. This second one also depends on geometrical parameters of the static field, such as the radius of the static quadrupole ring that sets the major radius of the torus, and its gradient g_q that, together with the frequency of the dressing fields, sets the minor radius ρ of the torus by means of the resonance condition $g_q\rho = B_0 = \hbar\omega/g_F\mu_B$.

This has been performed looking at the Hessian matrix (also known as curvature

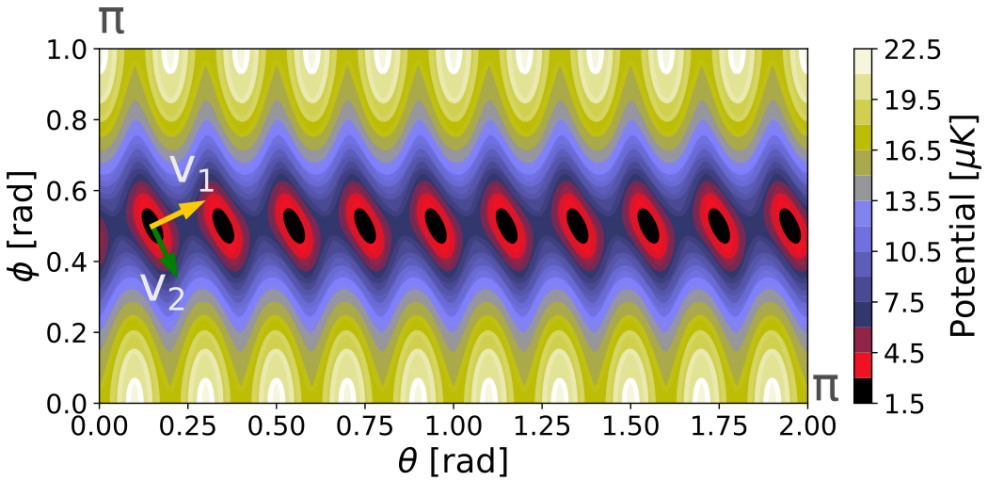


Figure 7.3.: The directions of the eigenvectors of the Hessian matrix, $\boldsymbol{v}_1$ and $\boldsymbol{v}_2$, indicate the orientation of the trap.

matrix) of $|B_\pm|^2$ in the two angular coordinates

$$H = \begin{pmatrix} \partial_\theta^2 |B_\pm|^2 & \partial_\theta \partial_\phi |B_\pm|^2 \\ \partial_\theta \partial_\phi |B_\pm|^2 & \partial_\phi^2 |B_\pm|^2 \end{pmatrix}$$

In the locations of the minima. Indeed, the eigenvectors of the curvature matrix point along the curvature extremes of the surface, allowing to identify the directions of the "long" and "short" axes of the wells. Also, since the gradient at the centre of the wells is null, the ratio between the eigenvalues of the Hessian matrix gives information about the isotropy of the minima. Albeit, this last parameter requires re-scaling in terms of the geometry of the torus, i.e. the minor and major radii of the torus[1].

As the number of tunable parameters is relatively high (formed by four amplitudes for the dressing fields plus the minor and major radius of the torus and the order of the multi-pole), here only a descriptive analysis will be presented.

Specific attention needs to be addressed in the choice of parameter sets, as they need to satisfy validity conditions for the model. In reference to equations (4.15) and (4.16), the naming of the parameters will be set as a and b for the circular components of the toroidal field $\boldsymbol{B}_{TD}^{(t)}$, in analogy to Section–4.2.1.

[1]In the small angle limit, the distances in the toroidal and poloidal direction can be approximated as $(\Delta L)_\theta = R_0 \Delta\theta$ and $(\Delta L)_\phi = \rho_0 \Delta\phi$ respectively, where R_0 and ρ_0 are the major and minor radii of the torus.

To begin with, it will be considered only the case for which there are two poloidal minima, respectively at the top and bottom of the ring. This restricts the region of interest to $\phi = \pm\pi/2$ setting also a condition of relation between a and b. As illustrated in Figure–(4.4) this poloidal orientation of the minima restricts the phase of the two amplitudes to be opposed to each other, i.e. restricting the ratio of the two amplitudes to be a negative real number $a/b \in \mathbb{R}^-$ and imposing $a, b \neq 0$.

Moreover, the amplitude of the multi-pole dressing is required to be smaller than the toroidal contribution $|B_\pm^{(m)}| < |B_\pm^{(t)}|$. As otherwise, regions $|B_\pm| = 0$ would be allowed, causing degeneracy of the eigenvalues $E_{m_F}^\pm$and consequently allowing for Majorana spin flips. For this reason, $u_+ = u_- = u \in \mathbb{R}$ is required to be smaller than $\max\{a, b\}$.

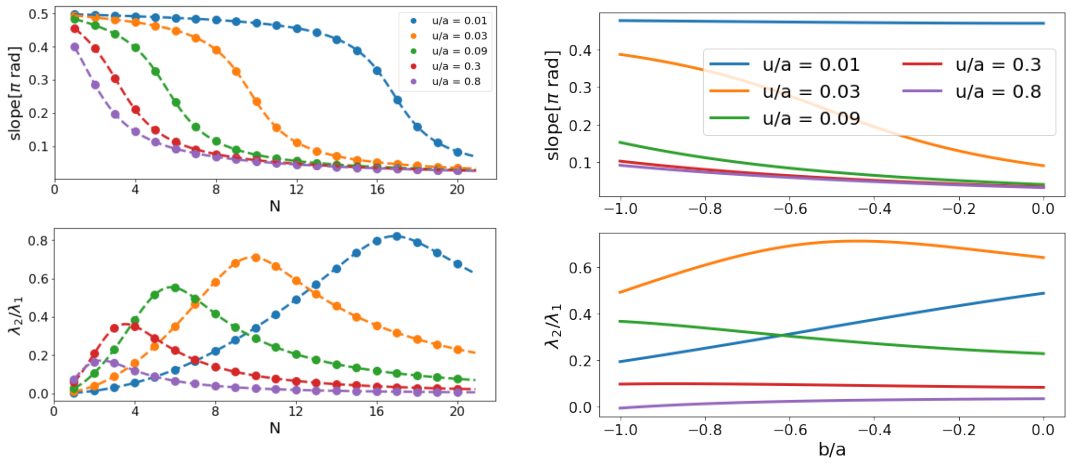
To fulfil the above considerations the value for the component a is arbitrarily set and the values of the other amplitudes are obtained setting the ratios b/a and u/a in the ranges $-1 < b/a < 0$ and $0 < u/a < 1$.

With the above condition the elements of the Hessian for $\phi = \pi/2$ result:

$$\begin{aligned}
\partial_\theta^2 \left(|B_\pm|^2\right)\big|_{\phi=\pi/2} &= -n^2 u(a+b)\sin(n\theta) \\
\partial_\phi^2 \left(|B_\pm|^2\right)\big|_{\phi=\pi/2} &= -2\,u^2 \sin(n\theta)^2 - 2\,(a+b)\,u \sin(n\theta) - 2\,ab \\
\partial_\theta \partial_\phi \left(|B_\pm|^2\right)\big|_{\phi=\pi/2} &= \pm n u(b-a)\sin(n\theta)
\end{aligned}$$

Diagonalization of the Hessian matrix lead to the plots in Figure–7.4. The eigenvalues of the Hessian are written as λ_1, λ_2 with $\lambda_1 > \lambda_2$, with unit eigenvectors labelled as $\hat{\boldsymbol{v}}_{1,2}$ as illustrated in Figure–7.3. Since the eigenvectors of a symmetric matrix are orthogonal to each other, only the angle $\cos^{-1}(\hat{\boldsymbol{v}}_1 \cdot \hat{\boldsymbol{v}}_\theta)$ that $\hat{\boldsymbol{v}}_1$ forms with the θ–axis is taken into consideration, as the other will be pointing in the orthogonal direction. To give an estimate of the isotropy of the minimum, the ratio between the eigenvalues of the Hessian is considered. When the ratio λ_2/λ_1 is unitary, the minimum presents the same curvature along the two orthogonal axes, indicating that the trap is isotropic in its centre. Conversely, when $\lambda_2/\lambda_1 \simeq 0$ the minimum presents a high anisotropy. Again, it is to be highlighted that this parameter is an indicator of the isotropy of the trap only in the angular coordinates and needs to be re-scaled to the geometric properties of the torus used.

In Figure–7.4a, fixing the ratio $b/a = -0.5$, the slope of the $\boldsymbol{v}_1$ and the ratio



(a) Inclination of $\boldsymbol{v}_1$ and λ_2/λ_1 for different values of u/a as a function of the multi-pole order n (indicated in the figure as N) for a fixed ratio $b/a = -0.5$.

(b) Inclination of $\boldsymbol{v}_1$ and λ_2/λ_1 for different values of u/a as a function of b/a for a fixed number of traps $N = 10$.

Figure 7.4.: Orientation of the traps (i.e. the slope or angle $\cos^{-1}(\hat{\boldsymbol{v}}_1 \cdot \hat{\boldsymbol{v}}_\theta)$ that the eigenvector $\hat{\boldsymbol{v}}_1$forms with the toroidal direction $\hat{\boldsymbol{v}}_\theta$) and isotropy (measured as the ratio λ_2/λ_1between the two eigenvalues of the curvature matrix) of the traps, in terms of the complex amplitudes of the toroidal (a and b) and multi-pole (u and v, with $u = v$) dressing fields.

λ_2/λ_1 is shown as a function of the number of traps N in the ring, for different ratios u/a. For small N the eigenvector $\boldsymbol{v}_1$ is closely orthogonal to the θ–axis, presenting high anisotropy. For high number of minima, the same vector is found to be parallel to the θ–axis and presenting high anisotropy. The smoothness of the behaviour for intermediate values of N is clearly dependent on the ratio u/a. The level of isotropy of the trap reaches a maximum in the region for which $\boldsymbol{v}_1$ forms an angle of $\pi/4$ with the θ–axis. Also, an increased maximum isotropy is found for smaller values of the ratio u/a.

Similarly, in Figure–7.4b the number of traps is fixed to $N = 10$ and the inclination of $\boldsymbol{v}_1$ and the isotropy of the minima is observed as a function of the ratio b/a for different values of u/a. The inclination of $\boldsymbol{v}_1$ presents small variability for all the values of u/a except for $u/a = 0.03$. For the same value of u/a the inclination of the Hessian's eigenvector presents a change of concavity and a broad maximum of the isotropy around $b/a \simeq -0.5$. This relates to the plot of Figure–7.4a (where it was imposed the ratio $b/a = -0.5$) for which the curve for $u/a = 0.03$ present a peak in λ_2/λ_1 and a change of concavity of the slope of $\boldsymbol{\nu}_1$.

This analysis is merely explorative, as it needs to be adapted to the geometrical proportions of the torus, but gives an idea of how the shape of the minima changes, when varying the order and the amplitude of the multi-pole field.

7.4. Overlap of wave functions

Finite element numerical methods can be used to estimate how different parameters affect the overlap of the stationary wave functions on superimposed minima of $E^+_{m_f}$ and $E^-_{m_f}$. A region of interest in the (θ, ϕ)–plane is selected, isolating a single minimum for the two different potentials, and re-scaled to match the physical dimension of the desired torus as $x = R_0\theta$ and $y = \rho_0\phi$, where R_0 and ρ_0 are the major radius and minor radius of the torus. Then, the region of interest is discretised in rectangular elements according to its aspect ratio.

The wave functions are then computed using the Matrix Numerov's Method [112]. Each pixel represents a localized basis function $|j\rangle$ null everywhere except for the internal area of the pixel for which it presents a constant value $1/(\delta_x\delta_y)$, with δ_x, δ_y being the pixel size along the two axes. The approximated kinetic energy,

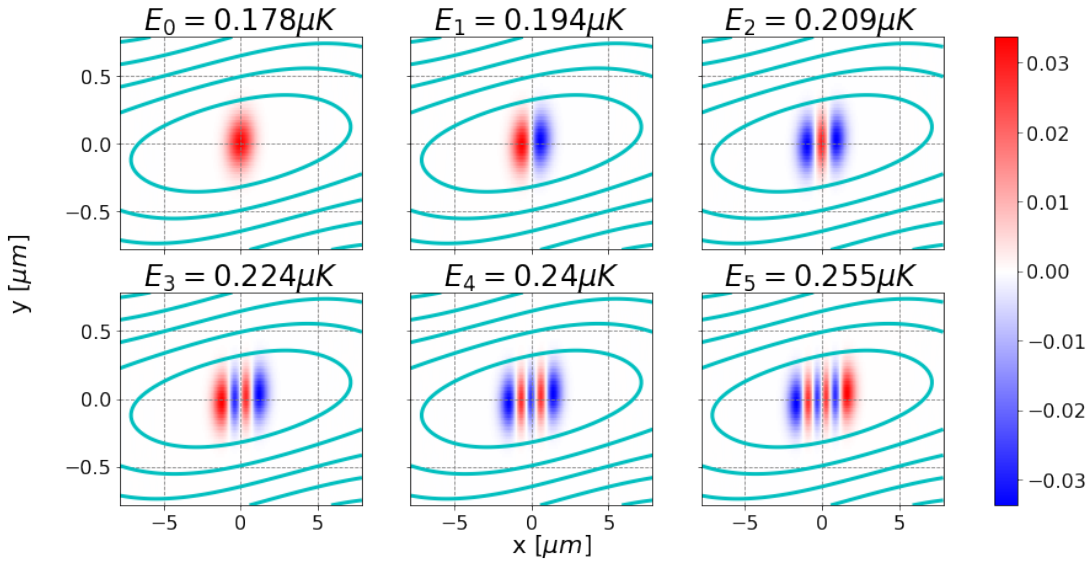


Figure 7.5.: Eigenstates for the $R_0 = 0.5\,mm$, $\rho_0 = 1\,\mu m$ and $n = 100$ torus. Wave functions relative to the first 6 levels, together with contour lines of the potential with $1.2\,\mu K$ per iso-line.

with corrections in the order of $O(\delta_i^6)$, $i = x, y$, can then be written as:

$$-\frac{\hbar^2}{2m}\nabla^2 = -\frac{\hbar^2}{2m}(\frac{1}{\delta_x^2}\sum_{\{j\}_x}|\{j\}_x\rangle + \frac{1}{\delta_y^2}\sum_{\{j\}_y}|\{j\}_y\rangle - \frac{2}{\delta_x^2}|j\rangle - \frac{2}{\delta_y^2}|j\rangle)$$

where $\{\cdot\}_{x(y)}$ indicates the horizontal (vertical) neighbours and m indicates the mass. This corresponds to a symmetric matrix null every where, but in two non principal diagonals. The potential energy then corresponds to a diagonal operator $\hat{V}_j = V_j|j\rangle\langle j|$, where V_j is the value of the potential energy at the pixel j. Standard numerical diagonalization algorithms is then used to compute the eigenenergies ϵ_i and relative eigenvectors $|\psi_i\rangle$.

Once the wave functions are evaluated for the thermal states $\hat{\rho}_\pm = \sum_i e^{\frac{-\epsilon_i}{k_B T}}|\psi_i^\pm\rangle\langle\psi_i^\pm|$ specific case, the Canonical Ensemble allows to compute the density operator for a temperature T. Hence, considering a closed system, the weight of each eigenstate $|\psi_i\rangle$ is obtained as

$$p_i = e^{\frac{-\epsilon_i}{k_B T}},$$

to build the density operator

$$\hat{\rho} = \sum_i p_i|\psi_i\rangle\langle\psi_i|.$$

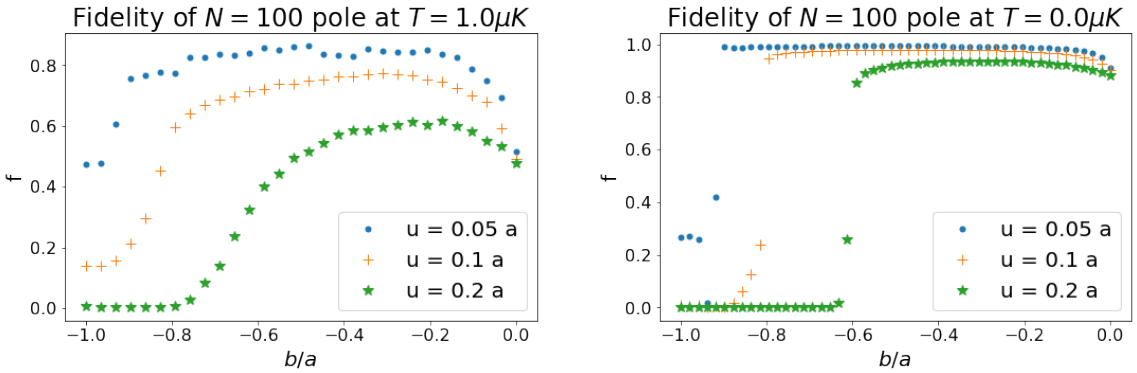
This operation is repeated for both of the potentials and the overlap between the two density operators (indicated as $\hat{\rho}^\pm$) evaluated using the fidelity of quantum states defined between the two states ρ_+ and ρ_- as

$$\mathsf{f}(\rho_+, \rho_-) = \|\sqrt{\rho_+}\sqrt{\rho_-}\|_{tr},$$

with $\|M\|_{tr} = \mathrm{Tr}(\sqrt{M^\star M})$ and $\sqrt{M} = U\sqrt{\Sigma}V^\star$ where $M = U\Sigma V^\star$ is the singular value decomposition of M.

This method has been applied on two different geometries.

The first one sees a major radius of $R_0 = 0.5\,mm$ and a minor radius of $\rho_0 = 1\,\mu m$ for $n = 100$ traps. It is a bad example: For an ideal multi-pole this would mean an amplitude variation across the minor diameter of the torus of about $\Delta A/A \simeq 40\%$, which is definitely not negligible, leading to severe potential deformation. Nonetheless, as stressed in Section–7.2, the geometry of the potential is determined by the mutual winding of the two dressing fields on the horizontal plane. Thus this does not exclude that there might exist a multi-pole–like mag-



(a) Fidelity $\mathsf{f}(\rho_+, \rho_-) = \|\sqrt{\rho_+}\sqrt{\rho_-}\|_{tr}$ between the thermal states $\hat{\rho}_\pm = \sum_i e^{\frac{-\epsilon_i}{k_B T}} |\psi_i^\pm\rangle\langle\psi_i^\pm|$ of the potential of equation (7.3) for a temperature $T = 1\,\mu K$ as a function of the potential parameter b for different values of the radio frequency amplitude u fixing the value of $a = 1G$.

(b) Fidelity $\mathsf{f}(|\psi_0^+\rangle, |\psi_0^-\rangle) = |\langle\psi_0^+|\psi_0^-\rangle|$ between the fundamental states $|\psi_0^\pm\rangle$ for the potential in (7.3) (i.e. equivalent in considering a temperature of $0\,K$) the potential parameter b for different values of the radio frequency amplitude u fixing the value of $a = 1G$.

Figure 7.6.: Fidelity between the eigenfunctions for the potential of equation (7.3) for the $R_0 = 0.5\,mm$, $\rho_0 = 1\,\mu m$ and $n = 100$ torus: for a thermal state at a temperature of $T = 1\,\mu K$ (a) and for the fundamental state (b).

netic field source which provides the correct mutual winding of the fields and a reasonable amplitude uniformity.

After computing the wave functions for several values of the ratio b/a (see example for $a = 1\,G$, $b/a = 0.25$ and $u/a = 0.05$ in Figure–7.5) and different values of u, the fidelity is evaluated for a temperature of $T = 1\,\mu K$ and for the fundamental state. The behaviour versus b/a is illustrated in Figure–7.6a and presents low overlap for lower values of b/a with a rapid increase towards a plateau for intermediate values and slight decrease towards $b/a = 0$. Higher fidelity plateaus are achieved with higher values of u, with the best performances observed for $u = 0.5$ presenting fidelity over $\mathsf{f} = 0.8$. The results for the fundamental state are similar (see Figure–7.6b), with sharper initial increase to higher values of fidelity that reaches values close to unity.

The second case sees a major radius of $R_0 = 1\,cm$, a minor radius of $\rho_0 = 5\,\mu m$ with $n = 50$ minima, resulting in a relative field variation across the cell of about $\Delta A/A \simeq 5\%$. This potential produces highly non isotropic traps, due to geometrical construction.

As shown in Figure–7.7, the horizontal size of the traps is about 200 times larger

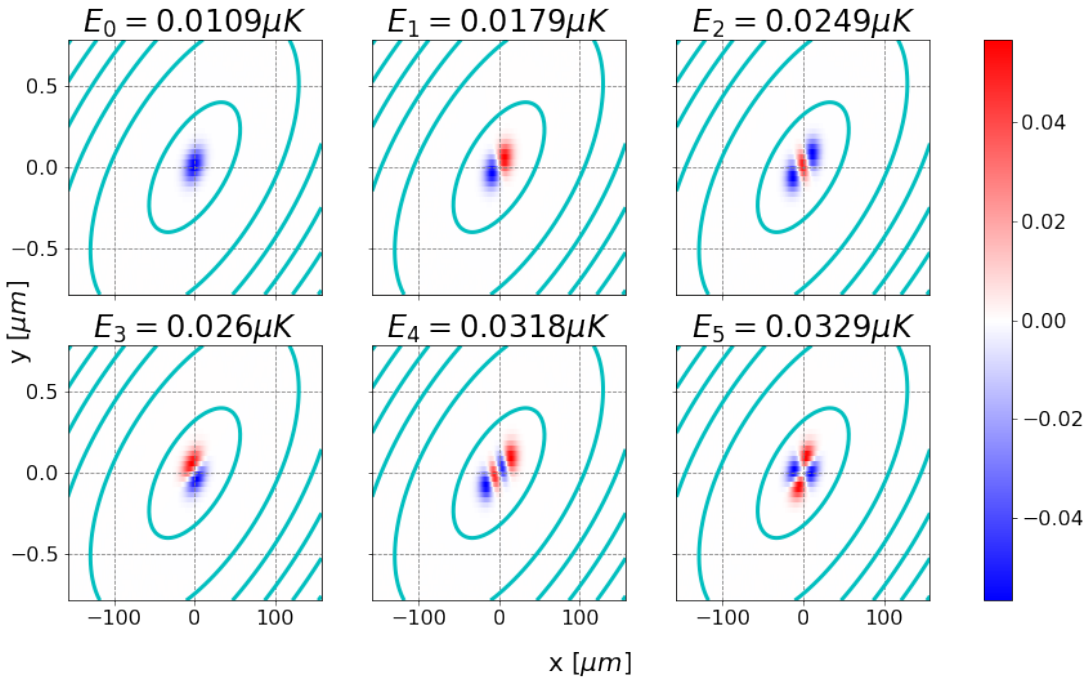


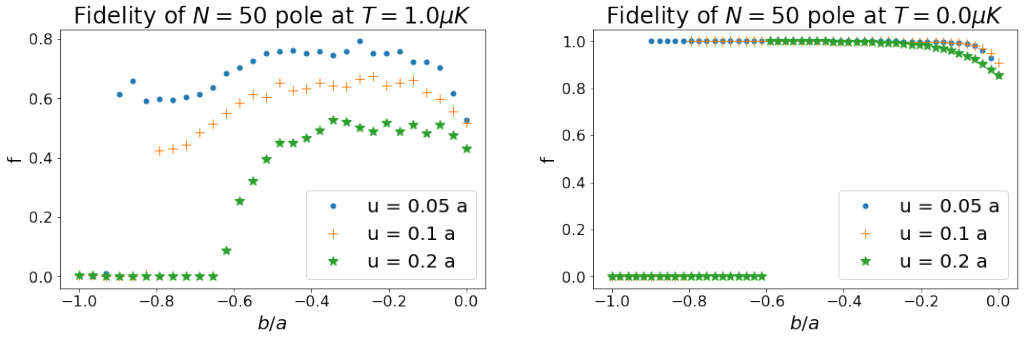
Figure 7.7.: Eigenstates for the $R_0 = 10\,mm$, $\rho_0 = 5\,\mu m$ and $n = 50$ torus, with $a = 2\,G$. Wave functions relative to the first 6 levels, together with contour lines of the potential with $0.83\,\mu K$ per iso-line.

than the vertical one. On the other hand this means that the traps highly aligned along the centre of the poloidal minimum. Even though the extremes of the two minima do not align, resulting in regions of non overlapping of the two wave functions, there might be a large section in the centre of the trap where the wave functions do overlap constructively.

The increase of the minor radius causes a decrease in the trap frequency for the higher confinement axis with respect to the previous case. Indeed in Figure–7.7 excitation in both of the axes are visible in the lowest energy eigenstate, conversely to Figure–7.5 where excitation is seen for only the elongated axis.

Evaluation of the fidelity for this case, shown in Figure–7.8 presents similar results, compared to the previous case. The variability of the fidelity of the thermal case is higher with respect to the previous case, this is due to the very unbalanced aspect ratio of the region of interest, that makes it harder to get proportionate discretising cells and therefore introducing uncertainties in the evaluation of the wave functions. Differently from the $N = 100$-pole case, the rise of the fidelity is much sharper and reaches unity for all the values of u considered.

Overall, the best results are obtained when the field amplitude of the toroidal



(a) Fidelity $\mathsf{f}(|\psi_0^+\rangle, |\psi_0^-\rangle) = |\langle\psi_0^+|\psi_0^-\rangle|$ between the fundamental states $|\psi_0^\pm\rangle$ for the potential in (7.3) (i.e. equivalent in considering a temperature of $0\,K$) the potential parameter b for different values of the radio frequency amplitude u fixing the value of $a = 1G$.

(b) Fidelity $\mathsf{f}(|\psi_0^+\rangle, |\psi_0^-\rangle) = |\langle\psi_0^+|\psi_0^-\rangle|$ between the fundamental states $|\psi_0^\pm\rangle$ for the potential in (7.3) (i.e. equivalent in considering a temperature of $0\,K$) the potential parameter b for different values of the radio frequency amplitude u fixing the value of $a = 1G$.

Figure 7.8.: Fidelity between the eigenfunctions for the potential of equation (7.3) for the $R_0 = 10\,mm$, $\rho_0 = 5\,\mu m$ and $n = 50$ torus: for a thermal state at a temperature of $T = 1\,\mu K$ (a) and for the fundamental state (b).

radio frequency dressing is much smaller than the multi-pole one. This is fortified by the results from the previous Section, suggesting that for lower values of u more regular trap shapes can be achieved, reaching higher isotropy levels as shown in Figure–7.4a. On the other hand, lower amplitudes for the toroidal field mean lower trap depths between neighbouring minima, hence introducing a trade off that might result in different solutions depending on the desired application.

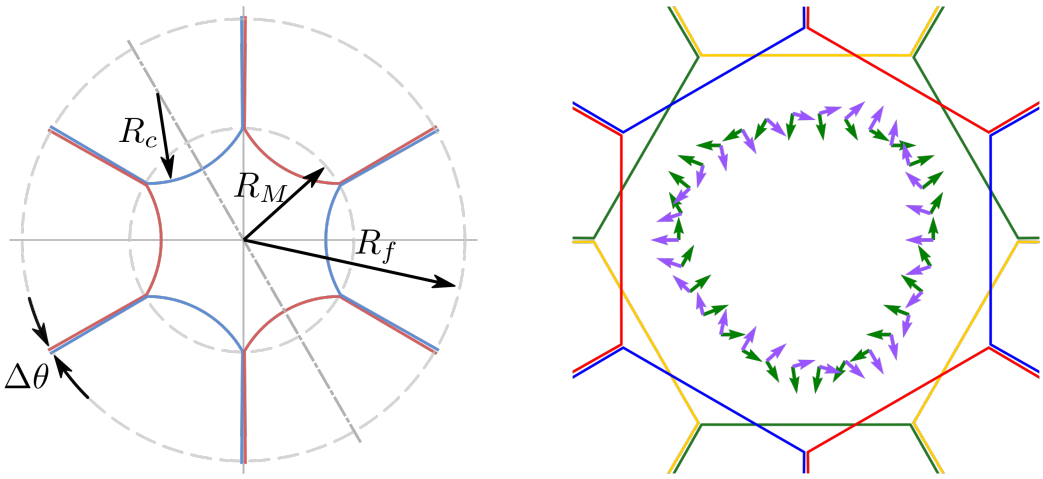
7.5. Multi-pole fields using planar wire structures

An interesting possibility, is to use planar wire structures producing multi-pole–like fields on parallel planes. This extends from the idea of atom chips, producing stronger magnetic fields and magnetic field gradients in the trapping region with reduced current consumption. This is due to the increased proximity of the current carrying wires generating the trapping fields to the trapped atomic clouds. Thus, using "planar multi-pole antennas" would enhance the performance of the multi-pole dressing field due to the same reasons.

Here a possible planar wire structure design producing multi-pole–like fields of

order n is presented. This design is composed by $2n$ wires running currents in opposite directions. As described in Figure–7.9a (for the case $n = 3$) it can be parametrized using three radii; namely: the radius R_f at which the wires are connected to a function generator, R_M at which the feeding wires connect to the structure generating the multi-pole field and the radius of curvature R_c and an angular distance between two neighbouring wires $\Delta\theta$. The curvature radius defines an arc of circumference with origin along the feeding wires' bisector. Its sign is defined positive (negative) if the arrow connecting the origin to the arc along the bisector is pointing outwards (inwards). The distance between two feeding wires within the same structure is $L = 2\sin((\pi/n - \Delta\theta)/2)$ constraining the absolute value of the curvature radius $\|R_c\|$ to be greater than $L/2$. Alternatively, it is possible to define a curvature parameter $\tau_c = \frac{L}{2R_c} \in [-1, 1]$, independent from the multi-pole order and size.

In Figure–7.9b the directions of the projection of the field produced on a plane parallel to the wires is shown for two orthogonal wire structures with $\tau_c = 0$.



(a) Definition of the design parameters.

(b) The field directions produced along a circle by two orthogonal antennas are shown. The purple (green) arrows indicate the direction of the field produced by the red and blue (green and yellow) structures.

Figure 7.9.: Planar wire structures antennas for multipole-like fields. In panel (a) the geometric parameters are indicated for a $n = 3$ antenna are illustrated. In panel (b) the field directions produced by two orthogonal $n = 3$ antennas with $R_c = \pm\infty$ (i.e. with curvature parameter $\tau_c = 0$) along a circumference co-axial with the antenna are shown.

Conversely to the straight and normal to the plane wire case in Figure–7.1a, the planar wire structure presents, in principle, non negligible field components along the $\hat{\boldsymbol{z}}$ direction. Moreover, the field only resembles the behaviour of the multi-pole field. Thus, there might be regions for which the field amplitude is not homogeneous around a closed circular path, or others in which the orthogonality between the two fields generated by two orthogonal structures is not met. Even the previous conditions are both met in some specific area, it is possible that this area corresponds to a very bad ratio of field amplitude over current consumption. It is then necessary to identify a set of properties to be satisfied and establish a hierarchy between them and ultimately select a region for which a good compromise of properties is met.

The properties that one would require to be met, verbally described above, require formal definition to formulate a method of evaluation.

To simplify the task of defining property estimators, a structure with curvature τ_c and order n is represented by the symbol $\Sigma^n_{\tau_c}$ and its orthogonal counterpart with $\Sigma^{n\perp}_{\tau_c}$. Similarly, the field produced by a structure $\Sigma^n_{\tau_c}$ ($\Sigma^{n\perp}_{\tau_c}$) is referred to as $\boldsymbol{B}^n_{\tau_c}(\boldsymbol{B}^{n\perp}_{\tau_c})$

Due to the symmetry of the geometry, it is helpful to define properties along equidistant points in a circular trajectory, at a defined height from the planar wire structure. Hence, given a structure $\Sigma^n_{\tau_c}$, a number $\eta = 2\kappa n, \kappa \in \mathbb{N}$ of points p_i equally distributed along a circumference of radius r placed at a height z from the wire structure.

The orthogonality condition at a point p_i requires that the angle formed by the projection on the horizontal plane of $\boldsymbol{B}^n_{\tau_c}(p_i)$ and $\boldsymbol{B}^{n\perp}_{\tau_c}(p_i)$ equals π. Thus, taking $\boldsymbol{b}_i = \boldsymbol{B}^n_{\tau_c}(p_i) - (\boldsymbol{B}^n_{\tau_c}(p_i)\cdot\hat{\boldsymbol{z}})\hat{\boldsymbol{z}}$ and similarly $\boldsymbol{b}^\perp_i$, the comprised angle is found as $\theta_i = \cos^{-1}(\boldsymbol{b}_i\cdot\boldsymbol{b}^\perp_i/(b_i b^\perp_i))$, and the orthogonality is defined as

$$\Theta(r,z) = \langle\theta\rangle - \pi\left(= \frac{1}{\eta}\sum_{i=1}^{\eta}\theta_i - \pi\right)$$

Then, to evaluate the undesired vertical field component the following quantity is used

$$\zeta(r,\theta) = \frac{\left\langle \boldsymbol{B}^n_{\tau_c}(p_i)\cdot\hat{\boldsymbol{z}}\right\rangle}{\langle b_i\rangle},$$

and to estimate the field amplitude and its fluctuations, $\langle b_i\rangle$ and $\beta = \sigma\langle b_i\rangle / \langle b_i\rangle$ is used.

These quantities have been evaluated for different curvatures $\tau_c = \{-1, -0.5, 0, 0.5, 1\}$ for the $n = 8$ case. The geometry is normalized, defining $R_M = 1$ and $R_f = 2$ in arbitrary units and similarly, a unit measurement system for which the magnetic permeability constant equals unity is chosen, and the current amplitude set to unit. For each structure, the field has been simulated using a Biot-Savart field simulation, discretising the wire in segments of length $\delta l = 0.05$ and using $\kappa = 5$.

In Figure–7.10, the obtained results are shown, apart from the orthogonality condition that resulted to be $\Theta(r, z) < 10^{-4}\, deg$ for the entire r, θ–region in each case. Each row corresponds to a curvature parameter, the left column showing the ratio between vertical and horizontal field, in the central column the in plane field amplitude is shown and on the right columns the relative fluctuations of the in plane field amplitude are shown. For the two external columns the white line and the black line mark the 10% and 5% respectively, while each of the black lines in the central column marks a decrease in amplitude of an order of magnitude.

As expected, the main issue for planar wire structures is the non negligible field in the vertical direction. The diagrams present optimal curves, on which the ratio between the vertical and horizontal components is negligible. But, except for a tight region in the neighbourhood of these curves, this ratio becomes even higher than one. Albeit, this can be improved inserting, for instance, an identical structure on a higher level, cancelling out the vertical field in the region between them, this spoils the whole point of working with planar structures.

The field amplitude still presents high dependency on the distance from the centre, dropping by several orders of magnitude when approaching the symmetry axis $r = 0$. On the other hand, in the regions just above the wires, the field amplitude shows low variation as a function of the radius. This is particularly evident in the cases for $\tau_c < 0.5$.

The amplitude field fluctuations presents an optimum curve, not overlapping with the low vertical field amplitude region. Conversely to the first column, it presents a wide region for which the relative field fluctuations are significantly low.

This, represents a first guess scenario for a planar design with many different strategies that could possibly be used for improvement. For instance, given a certain radius of interest r_0, using two concentric structures, one being larger and the other one being smaller than r_0 can help to achieve better field amplitude uniformity in the region of interest. Also, using pairs of loops in place of each circumference arc can lead to similar results.

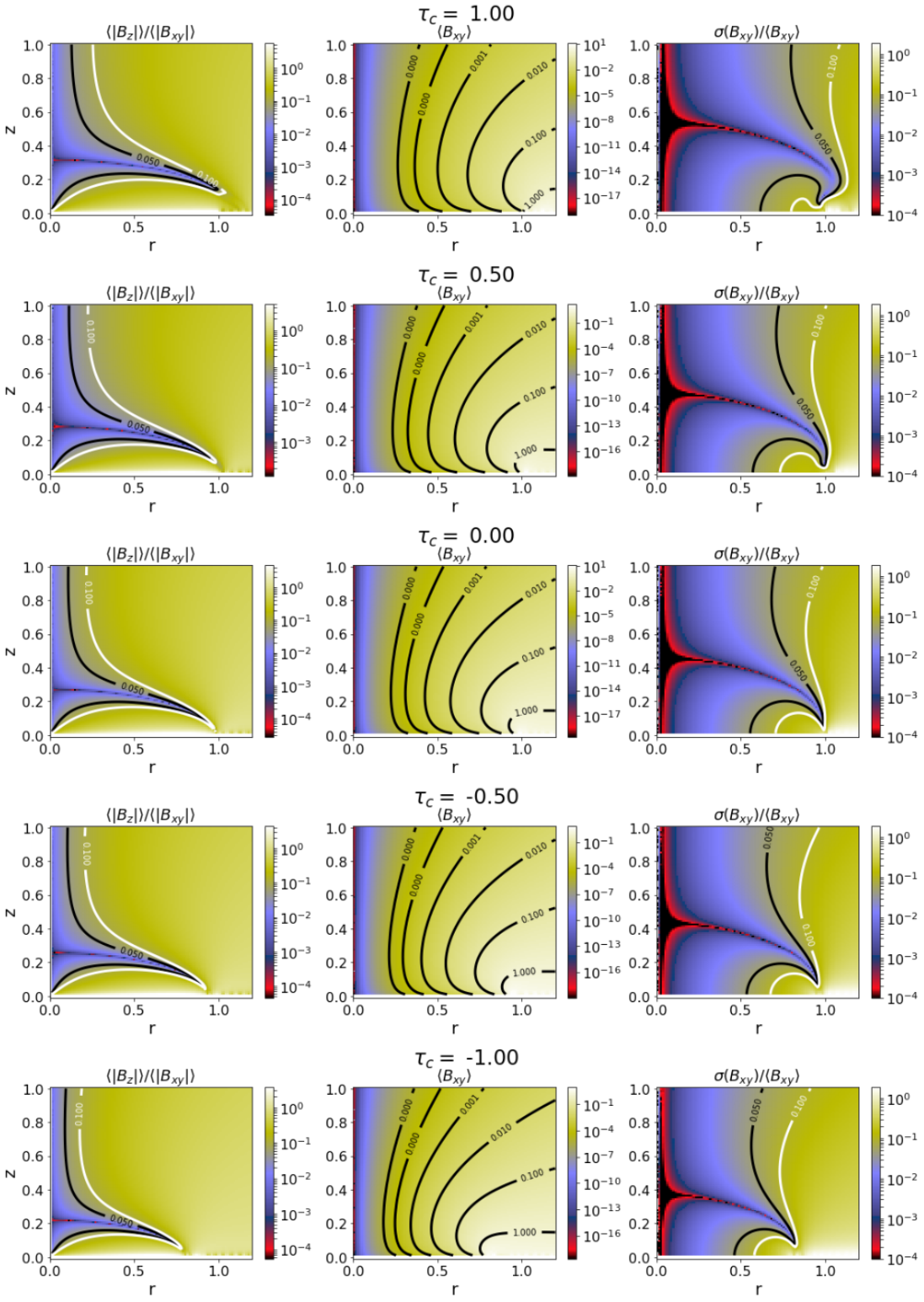


Figure 7.10.: Results of the Biot–Savart simulations for normalized planar antennas with pole order $n = 8$ for different curvatures τ_c in the r, z–plane: ratio of the vertical over horizontal field component amplitudes (left column), amplitude of the horizontal field component (central column) and its spatial fluctuations (right column). Further description in the text.

8. Conclusions and Outlook

This thesis reports on the advances in the experimental project having as objective the demonstration of a guided matter wave Sagnac interferometer, an atom-based device for high precision rotation sensing.

The design of the device includes a ring wave guide in which the position of state dependent atom traps can be actively controlled. This, together with a interferometric protocol, robust over wave guide imperfections, forms the atom–based equivalent of a fibre optic gyroscope.

The main advantage over the optical counterpart is that in the size of a centimetre [50], the used scheme presents interferometric performances equivalent to a FOG using several km of spooled optical fibre [14]. The illustrated scheme also presents enhanced versatility in comparison to optical devices. For instance, it allows full control over the velocity profiles of the counter propagating atomic clouds, a key feature towards the realization of fully strap-down inertial navigation devices.

The description of the experimental setup built in the past four years has been illustrated. This includes two optical tables providing the light necessary for the laser cooling, pumping and imaging of ^{87}Rb atoms, a vacuum setup in which a stable pressure in the order of $10^{-10}\,mbar$ has been achieved, the design of chip–based devices for the production of the required magnetic fields, described also in [84], and a high precision rate table. This last device showed to be able to imprint on the fully mounted vacuum setup an angular speed of $4 \times 10^{-3}\,deg/s$ with residuals on the control position $< 2 \times 10^{-5} deg$ and control over the angular rate better than $3.5 \times 10^{-5}\,deg/s$.

A more detailed list of equipment built and installed can be found on Table–8.1 showing the state of completion of the experimental setup in the month of December 2018. The micro–fabricated and intermediate layer were not delivered yet in their assembled form in 2018 due to unpredictable difficulties encountered by the manufacturers. However, the assembled device reached the laboratory

Item	Designed	Manufactured or purchased	Equipped
Optical and laser setup	YES	YES	YES
Magnetic fields: coils	YES	YES	YES
Magnetic fields: micro–fabrication	YES	YES	NO
Magnetic fields: intermediate layer	YES	YES	NO
Vacuum setup	YES	YES	YES
Control of the experiment: hardware	YES	PART.	PART.
Control of the experiment: software	YES	YES	YES
Safety system	YES	YES	YES
Rate table	YES	YES	YES

Table 8.1.: List of experimental equipment with record of the status at the end of the year 2018. The columns indicate if the item has been designed, manufactured or its components purchased and equipped in the experimental setup. The entries "YES", "NO" and "PART." indicate if the specific task has been fully completed, not started, or partially completed respectively.

in June 2019 and it is currently being installed in the experimental setup. The remaining incomplete task, i.e. the remaining hardware, includes current drivers and electrical protection of the atom chips and of the PCB that are currently under construction.

This thesis also reports on the advance over experimental and more conceptual challenges of this project, listed on Table–8.2. It first presents experimental evidence of loading an initial magnetic quadrupole trap into a ring quadrupole one. Forming the first step towards the formation of a circular matter wave guide.

Experimental evidence of the feasibility of the interferometric protocol on the $|F = 1, m_F = -1\rangle$ and the $|F = 2, m_F = 1\rangle$ sub levels of the $5^2S_{1/2}$ level of ^{87}Rb has been demonstrated. This is obtained with a $\pi - \pi/2 - \pi$ Ramsey sequence where the three microwave pulses are shone on radio frequency dressed rubidium atoms in free fall. Further investigation is required to use the same protocol over magnetically confined atoms.

Finally, a generalization of the trapping scheme presented in [51] has been shown. This consists of substituting an in–plane dipole oscillating field with an oscillating

Milestone	Theoretically understood	Experimentally demonstrated
Magneto optical trap	YES	YES
Magnetic trap	YES	YES
Quadrupole ring trap	YES	YES
Poloidal control	YES	NO
State dependent toroidal control	YES	NO
Splitting/recombining operations	PART.	NO
Read out scheme	PART.	PART.
Interferometric sequence	PART.	PART.
Mechanical vibrational noise	PART.	NO
Enhance toroidal confinement	YES	NO
Overlap of the toroidal surfaces	PART.	PART.

Table 8.2.: List of milestones to be achieved with record of the status at the end of the year 2018. The columns indicate if the task or problem has been theoretically understood or solved and if it had experimental demonstration. The entries "YES", "NO" and "PART." indicate if the specific task has been fully completed, not started, or partially completed respectively.

multi-pole of order n. As a result the number of minima formed along the ring corresponds to the order of the multi-pole; conversely to [51], limited to a single trap. Such generalization enhances the confinement in the direction tangential to the ring, for purely geometrical reasons. This not only has positive impact on the performances of the interferometer, allowing for designs with larger interferometric area, but introduces a new technique to form 1D lattices with close boundary conditions. Moreover, a possible design using current carrying wires confined to a single plane able to produce multi-pole magnetic fields has been illustrated.

The progress achieved during these past four years is evident comparing the tables Table–8.1 and Table–8.2 with the ones presented in Section–4.3, i.e. Table–4.1 and Table–4.2. There are two open questions under investigation in our experimental group that are not presented in this thesis. The first one is how to compensate for the non–zero difference of the Landé factors of the $|F = 1\rangle$ and $|F = 2\rangle$ manifolds of the hyperfine levels of the $5^2S_{1/2}$ electronic state of ^{87}Rb, as

illustrated in Figure–4.7a of Section–4.3. This causes the resonant toroidal surfaces not to overlap, causing kinetic excitation of the atoms under beam splitting, recombining and population inverting operations. Bethany Fox on, Sindhu Jammi and Konstantinos Poulios together with Thomas Fernholz are theoretically and experimentally studying the possibility of solving this task by means of an additional microwave dressing coupling the $|F = 1, m_F = -1\rangle$ and $|F = 2, m_F = -2\rangle$ hyperfine sub levels.

The second open question is to evaluate the effects of vibrational noise on the interferometric signal caused by the mechanical coupling between the environment and the wave guide, and find a protocol allowing to compensate for it. Jamie Johnson, under the supervision of Thomas Fernholz, is currently theoretically investigating this problem looking at possible effects of rotational vibrations in the three spatial axes and the possibility of using more elaborated interferometric protocols compensating for them.

Concluding, this thesis illustrated the experimental and theoretical efforts undertaken to produce a fully guided matter wave interferometer. Such device represents a valid candidate to the future generation of atomic inertial sensors, with high versatility and miniaturisability properties, making it suitable for portable devices. Moreover, as described in the last Chapter, simple modification of the trapping scheme opens for more fundamental research in the field of atomic lattices.

A. On rubidium structure

A.1. Coarse structure

For an Hydrogenoid atom (only one electron) only the principal quantum number n determines the energy of the electron. The other levels are degenerate. The energy is given by the Rydberg formula $E_n = -R/n^2$. For more electrons the energy of the electron can be found as $E_{n,l} = -R/n^{\star 2}$, with $n^\star = n - \delta_l$ and δ_l being an experimentally obtained parameter namely the quantum defect.

A different approach is to start from an Hamiltonian describing the Coulomb interaction of each electron with each other and the nucleus of the atom [77], i.e.:

$$H = \sum_i \left(-\hbar/2\mu\nabla_i^2 - Ze^2 4\pi\epsilon_0/r_i + e^2 4\pi\epsilon_0 \sum_{j>i} 1/r_{ij} \right).$$

[1] In this case it is possible to apply the *central field approximation,* i.e. assuming that electronic repulsion can be treated as a central potential $V_C(r_i)$ [113, 77]. The Schrödinger equation becomes separable and the wave–function of the system can be built as a product of wave functions $\Psi = \prod_i \psi_i$ where each ψ_i is solution of the equation $H_i\psi_i = E_i\psi_i$, with $H_i = -\hbar^2/2m\nabla_i^2 - Ze^2 4\pi\epsilon_0/r_i + V_C(r_i)$.

Being the single electron Hamiltonian only dependent on the radius, a suitable solution ψ_i can be found as $\psi_i = \phi(r_i)Y_l^m$, where ϕ is a function only dependent on the radius r_i and Y_l^m indicates the spherical functions. Observing that the operator ∇^2 can be written in terms of the square angular momentum L^2 as $\nabla^2 = \frac{1}{r^2}\partial_r r^2 \partial_r - \frac{L^2}{\hbar^2 r^2}$ and $L^2 Y_l^m = \hbar^2 l(l+1)Y_l^m$ then it is possible to write

[1] The term μ indicates the reduced mass of the system $\mu = m_e \times M_n/(m_e + M_n)$, where $M_n = Am_n$is the mass of the nucleus composed by A nucleons of mass m_n. Since $M_n \gg m_e \forall A$, the reduced mass results to be almost identical to the electron mass $\mu \simeq m_e$.

$H_i\psi_i = E_i\psi_i$ as

$$\begin{aligned} Er\phi(r_i) &= -\frac{\hbar^2}{2m}\left(r\partial_r^2 + 2\partial_r\right)\phi(r_i) + \left[\frac{\hbar^2 l(l+1)}{2mr^2} - \frac{Ze^2 4\pi\epsilon_0}{r_i} + V_C(r_i)\right] r\phi(r_i) \\ &= -\frac{\hbar^2}{2m}\partial_r^2\left(r\phi(r)\right) + \left[\frac{\hbar^2 l(l+1)}{2mr^2} - \frac{Ze^2 4\pi\epsilon_0}{r_i} + V_C(r_i)\right] r\phi(r_i) \end{aligned}$$

To complete the equation it is necessary to write the explicit form of V_C.

There are no (to my knowledge) fundamental derivations for it. Nonetheless, it is reasonable to assume that an electron in the vicinity of the nucleus will fill the attraction of all the protons of the nucleus, while an outer electron of a neutral atom will feel the charge of only one proton, being the rest of the nuclear charge mostly screened by the other electrons. Similarly, an electron in the intermediate region will perceive the nuclear charge to be partially screen. Therefore it is possible to substitute the last two term in the square brackets with an effective potential $V_{eff} = -\frac{Ze^2 4\pi\epsilon_0}{r_i} + V_C(r_i) = -\frac{Z_{eff}e^2 4\pi\epsilon_0}{r_i}$. Here $Z_{eff}(r)$ is the effective charge experienced by the electron, which is then required to be a function of the distance from the nucleus that equals Z for small r and monotonically decreases to reach asymptotically the value $Z_{eff}(r \gg 1) = 1$. The Eigenenergies can then be obtained through numerical integration of the equation.

If the form of the eigenfunctions for the entire atom is of interest is then also necessary to consider that the overall function needs to be anti–symmetric for particle exchange. A simple way to fulfill this condition is to build the wave function using the Slater determinant [77, 113].

A.2. Fine structure

On top of the coarse structure a further energy splitting on otherwise degenerate levels comes from the spin-orbit interaction of the valence electron. This more detailed splitting of the energetic levels is usually referred as *fine structure* [113, 77]. An electron moving through an electric potential is subject to an effective magnetic field

$$\begin{aligned} \boldsymbol{B} &= -\frac{\boldsymbol{v}}{c^2} \times \boldsymbol{E} = -\frac{\boldsymbol{v}}{c^2} \times \frac{1}{e}\left(\partial_r V\right)\hat{\boldsymbol{r}} \\ &= \frac{1}{m_e c^2}\frac{1}{er}\left(\partial_r V\right)\boldsymbol{r} \times m_e\boldsymbol{v} = \frac{1}{m_e c^2}\frac{1}{er}\left(\partial_r V\right)\boldsymbol{L} \end{aligned}$$

where $\boldsymbol{L}$ is the orbital angular momentum operator. Hence, the Hamiltonian that rules the interaction of an electron with magnetic momentum $\boldsymbol{\mu} = g_s \mu_B \boldsymbol{S}$ is given by $H = \boldsymbol{\mu} \cdot \boldsymbol{B} = \frac{g_s \mu_B}{m_e c^2} \frac{1}{er} \left(\partial_r V\right) \boldsymbol{S} \cdot \boldsymbol{L} = \frac{g_s \mu_B}{m_e c^2} \frac{Z_{eff} e 4\pi\epsilon_0}{r^3} \boldsymbol{S} \cdot \boldsymbol{L}$.

Here the term g_s is the giromagnetic spin for the electron and its value is $g_s \simeq 2$, relativistic correction due to Thomas precession of this formula leads to better accuracy simply substituting g_s with $g_s - 1 \simeq 1$.

As a result, the energy contribution due to spin–orbit interaction can be taken considering the expectation value of the Hamiltonian [89, 88]

$$E_{s-o} = \langle H \rangle \propto \langle \boldsymbol{S} \cdot \boldsymbol{L} \rangle$$

The evaluation of this energy is not straightforward, though. Since, as it can be easily verified, the scalar product $\boldsymbol{S} \cdot \boldsymbol{L}$ is not commuting with the operator L_z nor with S_z [77, 113]. This difficulty can be overcome considering the operator $\boldsymbol{J} = \boldsymbol{L} + \boldsymbol{S}$ whose eigenvalues span in the range $|L - S| \leq J \leq |L + S|$ while the eigenvalues of its third component is $m_J = m_S + m_L$.

Observing that $\boldsymbol{S} \cdot \boldsymbol{L} = \left(\boldsymbol{J}^2 - \boldsymbol{L}^2 - \boldsymbol{S}^2\right)/2$ it is now possible to evaluate the spin–orbit contribution as

$$E_{s-o} \propto \langle \boldsymbol{S} \cdot \boldsymbol{L} \rangle = \left(J(J+1) - L(L+1) - S(S+1)\right)/2$$

For the Rubidium case, we are interested on the fundamental state of the outermost electron and its nearest excited level.

The fundamental level sees orbital of type s, meaning that it possesses orbital angular momentum $L = 0$. This means that $J = S$ and the resulting spin orbit coupling is null. For the next level having $L = 1$ the resulting total angular momentum is comprised in the interval $|L - S| = 1/2 \leq J \leq L + S = 3/2$, hence it can have two possible values $J \in \{1/2, 3/2\}$ and the respective spin–orbit energetic contributions are $E_{s-o}^{(J=1/2)} \propto 1/2(3/2) - 2 - 3/4 = -2$ and $E_{s-o}^{(J=3/2)} \propto 3/2(5/2) - 2 - 3/4 = 11/4 - 2 = 3/4$.

A.3. Atom-magnetic field interaction

In presence of a magnetic field, each of the levels of the hyperfine splittings undergoes Zeeman splitting. The number of lines depends on the number of

possible eigenvalues $|m_F| \leq F, m_F \in \mathbb{Z}$ of the third component of the total angular momentum F_z. The Hamiltonian that rules the interaction is given by [77, 89, 88]

$$H = \mu_B(g_s \boldsymbol{S} + g_L \boldsymbol{L} + g_I \boldsymbol{I}) \cdot \boldsymbol{B}$$

Without any loss of generality, the coordinate frame is selected such that $\boldsymbol{B} = B\hat{\boldsymbol{z}}$. Thus, the Hamiltonian can be rewritten as

$$H = \mu_B(g_S S_z + g_L L_z + g_I I) \cdot B$$

where g_S, g_L and g_I are the giromagnetic factors for the spin, orbital angular momentum and nuclear spin respectively. In this experiment the interest is focused mainly on the electronic level $5^2S_{1/2}$ and its hyperfine structure. Hence, the term relative to the orbital angular momentum will not be considered. For weak magnetic fields (i.e. for fields causing Zeeman splitting much smaller than the Hyperfine splittings), the interaction is well approximated considering only the total angular momentum $\boldsymbol{F}$, the Hamiltonian can be approximated as

$$H = \mu_B g_F F_z \cdot B$$

Of eingenvalues

$$E_{m_F} = \mu_B g_F m_F B \tag{A.1}$$

Where g_F is the Landé factor for, defined as [88]:

$$g_F = g_J + (g_I - g_J)\,\frac{F\,(F+1) + I\,(I+1) - J\,(J+1)}{2F\,(F+1)}$$

With the Landé g_J factor being [88]

$$g_J = g_L\,(g_S - g_L)\,\frac{J\,(J+1) + S\,(S+1) - L\,(L+1)}{2J\,(J+1)}$$

A.3.1. Optical molasses and Magneto Optical Traps (MOT)

A two level atom colliding with a photon of momentum $\hbar\kappa$ gets into the excited state and re–emits a photon of the same frequency in a random direction and phase. When considering a thread of photons of a laser beam, this results in an

average scattering force given by [58, 77]

$$\boldsymbol{F}_{scatt} = \frac{\Gamma}{2}\frac{I/I_{sat}}{1+4I/I_{sat}+4\delta^2/\Gamma^2}\hbar\boldsymbol{\kappa} = \frac{\Gamma}{2}\frac{\Omega_R^2/2}{1+2\Omega_R^2+4\delta^2/\Gamma^2}\hbar\boldsymbol{\kappa} \tag{A.2}$$

where $\delta = \delta_0 + \boldsymbol{\kappa}\cdot\boldsymbol{v} \doteq \delta_0 + \Delta\delta$ is the detuning accounting for the Doppler effect on atoms moving at speed v (δ_0 being the detuning of the radiation for an atom at rest), Γ the decay rate of the excited state, I the intensity of the beam and $I_{sat}$the saturation intensity. For low atom velocity regimes Taylor expansion leads to [77]:

$$\begin{aligned}\boldsymbol{F}_{scatt} &\simeq \boldsymbol{F}_0 + \left(\partial_\delta \boldsymbol{F}_{scatt}\right)_{\delta=\delta_0}\Delta\delta \\ &= \boldsymbol{F}_0 + \left(\partial_\delta \boldsymbol{F}_{scatt}\right)_{\delta=\delta_0}\kappa v\end{aligned}$$

hat, when the atom and the beam travel in opposite directions (i.e. $\boldsymbol{\kappa}/\kappa = -\boldsymbol{v}/v$), can be re–written as

$$\boldsymbol{F}_{scatt} \simeq \boldsymbol{F}_0 - \left(\partial_\delta \boldsymbol{F}_{scatt}\right)_{\delta=\delta_0}\kappa v$$

When two counter propagating beams with same detuning from the transition (i.e. presenting $-\kappa_2 = \kappa_1 \doteq \kappa$) are shined on an atomic cloud, the total force experienced is [77]

$$\begin{aligned}\boldsymbol{F}_{molass} &= \boldsymbol{F}_0 - \left(\partial_\delta \boldsymbol{F}_{scatt}\right)_{\delta=\delta_0}\kappa_1 v - \left(\boldsymbol{F}_0 - \left(\partial_\delta \boldsymbol{F}_{scatt}\right)_{\delta=\delta_0}\kappa_2 v\right) \\ &= -2\left(\partial_\delta \boldsymbol{F}_{scatt}\right)_{\delta=\delta_0}\kappa v\end{aligned}$$

Explicitly differentiating the scattering force results in

$$\left(\partial_\delta \boldsymbol{F}_{scatt}\right)_{v=0} = \frac{\Gamma}{2}\frac{\Omega_R^2/2}{1+2\Omega_R^2+4\delta_0^2/\Gamma^2}\times 4\frac{-2\delta_0/\Gamma^2}{1+2\Omega_R^2+4\delta_0^2/\Gamma^2}\hbar\boldsymbol{\kappa}$$

when the two beams are red detuned w.r.t. the transition (i.e. $\delta_0 < 0$) the quantity $\alpha = 2\left(\partial_\delta \boldsymbol{F}_{scatt}\right)\kappa$ is greater than zero and the molass force can be understood as viscous friction

$$\boldsymbol{F}_{molass} = -\alpha\boldsymbol{v}$$

This technique, albeit being an efficient way to slow down atomic motion (i.e.

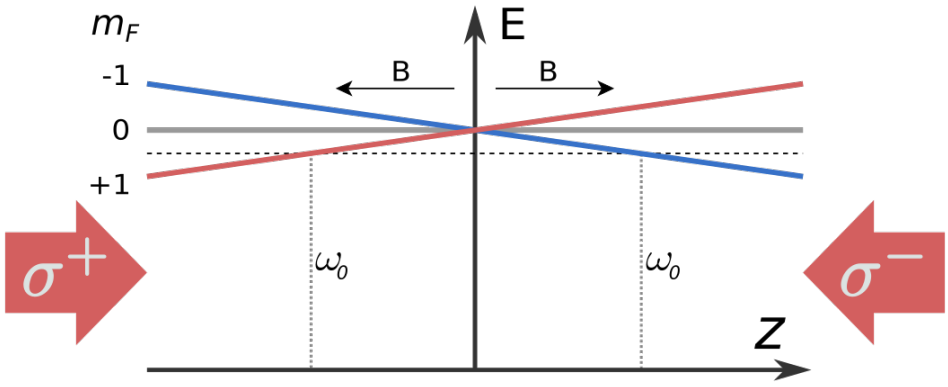


Figure A.1.: Magnetic fields direction with beam propagation and polarization forming a MOT.

cooling of the gas) does not consist on its own a confining method.

In case the light field is accompained by magnetic field, the value of the detuning δ will depend on the Zeeman splitting as well. This can be used in addition to optical molasses to trap and cool down atoms introducing a magnetic quadrupole, originating a trapping scheme commonly referred as Magneto Optical Trap (MOT).

The field generated by the quadrupole in the z direction is described in terms of its gradient $q > 0$ as $B(z) = qz$. The value of the detuning of the (counter-)propagating beam accounts for both the Doppler effect and the Zeeman splitting as $\delta_{(-)+} = \delta_0 + \Delta\delta_{(-)+} = \delta_0 \mp \kappa v + \mu_B \left(g_F^e m_F^e - g_F^g m_F^g\right) qz$, according to the structure of the atom in the limit of low fields. The force generated in this case for two counter-propagating light beams is [58, 77]

$$\begin{aligned} \boldsymbol{F}_{MOT} &= \boldsymbol{F}_0 + \left(\partial_\delta \boldsymbol{F}_{scatt}\right)_{\delta=\delta_0} \Delta\delta_+ - \left(\boldsymbol{F}_0 + \left(\partial_\delta \boldsymbol{F}_{scatt}\right)_{\delta=\delta_0} \Delta\delta_-\right) \\ &= \left(\partial_\delta \boldsymbol{F}_{scatt}\right)_{\delta=\delta_0} \Delta\delta_+ - \left(\partial_\delta \boldsymbol{F}_{scatt}\right)_{\delta=\delta_0} \Delta\delta_- \end{aligned}$$

t is now necessary to make some assumptions on the ground and excited states of the transition.

To simplify the treatment assume the atomic structure such that, the ground state presents internal state with $F = 0$, while the excited state presents $F' = 1$ and a Landé factor $g_F > 0$. The levels of the excited state undergo Zeeman splitting and there exists some distance $\pm z_0$, $z_0 \in \mathbb{R}^+$ from the center of the trap for which the $m_F = \mp 1$ sublevel crosses resonance with the light field. For

this to happen the (counter–)propagating beam needs to possess adequate (left) right handed circular polarization in order to drive a $\sigma_{+(-)}$ transition to satisfy selection rules as illustrated in Figure–A.1.

With this choice of polarization, the detuning of the (counter–)propagating beam can be written as $\delta_{(-)+} = \delta_0 + \Delta\delta_{(-)+} = \delta_0 \mp \kappa v \pm \mu_B g_F^e z$ and the force of the MOT can be expressed as

$$\begin{aligned} \boldsymbol{F}_{MOT} &= \left(\partial_\delta \boldsymbol{F}_{scatt}\right)_{\delta=\delta_0} \left(-\kappa v + \mu_B g_F z\right) - \left(\partial_\delta \boldsymbol{F}_{scatt}\right)_{\delta=\delta_0} \left(\kappa v - \mu_B g_F z\right) \\ &= -2\left(\partial_\delta \boldsymbol{F}_{scatt}\right)_{\delta=\delta_0} \kappa v + 2\left(\partial_\delta \boldsymbol{F}_{scatt}\right)_{\delta=\delta_0} \mu_B g_F z \\ &= -\alpha \boldsymbol{v} - \beta \boldsymbol{z} \end{aligned} \tag{A.3}$$

where $\beta = |2\partial_\delta(\boldsymbol{F}_{scatt})_{\delta=\delta_0}\mu_B g_F|$ and the sign choice comes from the consideration that the scattering force is always directed in the opposite direction of $\boldsymbol{z}$. Equation–(A.3) is recognizable as the force balance of a simple damped harmonic oscillator.

B. Complex plane representation of 2D magnetic multipoles.

Consider a set of infinitely long conductive wires normal to a plane Π. The magnetic field B generated by these wires is completely contained in Π. This allows to represent the components B_x and B_y of the magnetic field as real and imaginary part of a number in the complex plane $\mathbb{C}$. In such a picture, the magnetic field at position z generated by a single wire crossing the complex plane at z_0 can be written as [114]

$$B(z_0) = i\frac{\mu_0 I}{2\pi(z - z_0)^\star}$$

where μ_0 is the magnetic permeability of vacuum and $z^\star$ indicates the complex conjugate of z.

B.1. Bi-dimensional multipoles.

A $2N$-pole is defined as the field produced by $2N$ wires uniformly distributed around a circumference of radius $R > 0$ carrying the same current I flowing in alternate directions. The position of the wires can be written as

$$\left\{ R\, e^{i\frac{l\pi}{N}} \right\}_{l=0}^{2N-1}$$

as shown in Fig. B.1 on the following page.

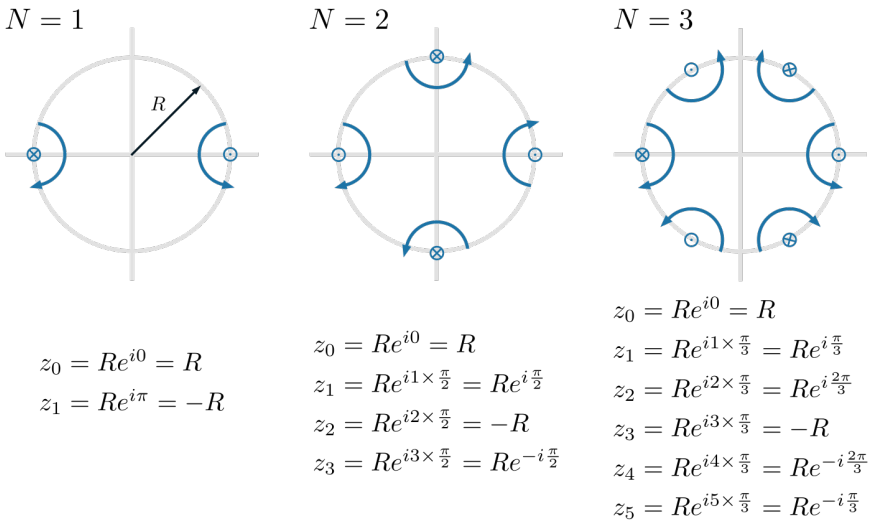


Figure B.1.: Example of spatial wire distribution and field direction for dipole ($N = 1$), quadrupole ($N = 2$) and exapole ($N = 3$) of radius R .

Consequently, the magnetic field $B(z)$ at position z for a $2N$-pole of radius R is

$$B^{2N}(z) = i\mu_0 \frac{I}{2\pi} \sum_{l=0}^{2N-1} \frac{(-1)^l}{\left(z - Re^{i\frac{l\pi}{N}}\right)^\star} \tag{B.1}$$

B.1.1. Amplitude of a magnetic multipole field in the origin

The expression for the magnetic field in $z = 0$ reads

$$B^{2N}(z=0) = i\mu_0 \frac{I}{2\pi} \sum_{l=0}^{2N-1} \frac{(-1)^{l+1}}{\left(Re^{i\frac{l\pi}{N}}\right)^\star} = i\mu_0 \frac{I}{2\pi R} \sum_{l=0}^{2N-1} (-1)^{l+1} e^{i\frac{l\pi}{N}}$$

for the dipole ($N = 1$) the field in the origin is

$$B^2(z=0) = i\mu_0 \frac{I}{2\pi} \sum_{l=0}^{1} (-1)^{l+1} e^{il\pi} = -i\mu_0 \frac{I}{\pi}.$$

While, for instance, for the quadrupole ($N = 2$) and for the exapole ($N = 3$), $B^4(0) = 0$ and $B^4(0)$.It is then reasonable to think that whenever $N > 1$

$$B^{2N}(z = 0) = i\mu_0 \frac{I}{2\pi R} \sum_{l=0}^{2N-1} (-1)^{l+1} e^{i\frac{l\pi}{N}} = 0 \tag{B.2}$$

This is equivalent in showing $\sum_{l=0}^{2N-1} (-1)^{l+1} e^{i\frac{l\pi}{N}} = 0$. Breaking the series in two halves, results

$$\begin{aligned}
\sum_{l=0}^{2N-1} (-1)^{l+1} e^{i\frac{l\pi}{N}} &= \sum_{l=0}^{N-1} (-1)^{l+1} e^{i\frac{l\pi}{N}} + \sum_{l=N}^{2N-1} (-1)^{l+1} e^{i\frac{l\pi}{N}} \\
&= \sum_{l=0}^{N-1} (-1)^{l+1} e^{i\frac{l\pi}{N}} + \sum_{l=0}^{N-1} (-1)^{l+N+1} e^{i\frac{l+N}{N}\pi} \\
&= \sum_{l=0}^{N-1} (-1)^{l+1} e^{i\frac{l\pi}{N}} + \sum_{l=0}^{N-1} (-1)^{l+N+1} e^{i\left(\frac{l}{N}+1\right)\pi} \\
&= \sum_{l=0}^{N-1} (-1)^{l+1} e^{i\frac{l\pi}{N}} - (-1)^N \sum_{l=0}^{N-1} (-1)^{l+1} e^{i\frac{l\pi}{N}} \\
&= \left(1 - (-1)^N\right) \sum_{l=0}^{N-1} (-1)^{l+1} e^{i\frac{l\pi}{N}}
\end{aligned}$$

Notice that whenever $N = 2M$, $M \in \mathbb{N}$ the first factor is identically zero. In case $N = 2M + 1$, $M \in \mathbb{N}$ the series becomes

$$\sum_{l=0}^{2(2M+1)-1} (-1)^{l+1} e^{i\frac{l\pi}{2M+1}} = \sum_{l=0}^{4M+1} (-1)^{l+1} e^{i\frac{l\pi}{2M+1}}$$

That, splitting the series as the sum of even and odd terms

$$\begin{aligned}
\sum_{l=0}^{4M+1}(-1)^{l+1}\,e^{i\frac{l\pi}{2M+1}} &= \sum_{l=0}^{2M}(-1)^{2l+1}\,e^{i\frac{2l\pi}{2M+1}} + \sum_{l=0}^{2M}(-1)^{2l+1+1}\,e^{i\frac{(2l+1)\pi}{2M+1}} \\
&= \sum_{l=0}^{2M}(-1)\,e^{i\frac{2l\pi}{2M+1}} - \sum_{l=0}^{2M}(-1)\,e^{i\left(\frac{2l}{2M+1}+\frac{1}{2M+1}\right)\pi} \\
&= -\left(1-e^{i\frac{\pi}{2M+1}}\right)\sum_{l=0}^{2M}e^{i\frac{2l\pi}{2M+1}} \\
&= -e^{i\frac{\pi}{2(2M+1)}}\frac{\left(e^{-i\frac{\pi}{2(2M+1)}}-e^{i\frac{\pi}{2(2M+1)}}\right)}{2i}2i\sum_{l=0}^{2M}e^{i\frac{2l\pi}{2M+1}} \\
&= e^{i\frac{\pi}{2(2M+1)}}\sin\left(\frac{\pi}{2\,(2M+1)}\right)2i\sum_{l=0}^{2M}e^{i\frac{2\pi}{2M+1}l}
\end{aligned}$$

The remaining sum is identically zero if $M > 0$ (therefore $N > 1$). This because it can be imagined as a set of $2M + 1$ vectors which directions is uniformally distributed on 2π. Hence confirming the validity of (B.2).

B.1.2. Behavior in the neighboring of the origin.

We now look what happens in the region around the origin. We can rewrite equation (B.1) as follows

$$\begin{aligned}
B^{2N}(z) &= i\mu_0\frac{I}{2\pi}\sum_{l=0}^{2N-1}\frac{(-1)^l}{Re^{-i\frac{l\pi}{N}}\left(\frac{z}{Re^{i\frac{l\pi}{N}}}-1\right)^{\star}} \\
&= i\mu_0\frac{I}{2\pi R}\sum_{l=0}^{2N-1}\frac{(-1)^{l+1}}{\left(1-\frac{z}{Re^{i\frac{l\pi}{N}}}\right)^{\star}}e^{i\frac{l\pi}{N}}. \qquad \text{(B.3)}
\end{aligned}$$

Recalling that the Maclaurin expansion of $\frac{1}{1-x}$ is $1+x+x^2+x^3+\ldots$ for $x \ll 1$, we can expand the (B.3) in the limit for $|z| \ll R$ as

$$\begin{aligned} B^{2N}(z) &\approx i\mu_0 \frac{I}{2\pi R} \sum_{l=0}^{2N-1} (-1)^{l+1} e^{i\frac{l\pi}{N}} \sum_{n=0}^{\infty} \left(\frac{z^\star}{R e^{-i\frac{l\pi}{N}}} \right)^n \\ &= i\mu_0 \frac{I}{2\pi R} \sum_{l=0}^{2N-1} (-1)^{l+1} e^{i\frac{l\pi}{N}} \sum_{n=0}^{\infty} \left(\frac{z^\star}{R} \right)^n e^{i\frac{nl\pi}{N}} \\ &= i\mu_0 \frac{I}{2\pi R} \sum_{l=0}^{2N-1} (-1)^{l+1} e^{i\frac{l\pi}{N}} \left(1 + \sum_{n=1}^{\infty} \left(\frac{z^\star}{R} \right)^n e^{i\frac{nl\pi}{N}} \right). \end{aligned} \tag{B.4}$$

Where in the last line the first term of the Maclaurin expansion has been written explicitly. For (B.2) this term is zero whenever $N > 1$. Therefore, we can rewrite the approximation as

$$B^{2N}(z) \overset{|z| \ll R}{\approx} i\mu_0 \frac{I}{2\pi R} \sum_{l=0}^{2N-1} (-1)^{l+1} e^{i\frac{l\pi}{N}} \sum_{n=1}^{\infty} \left(\frac{z^\star}{R} \right)^n e^{i\frac{nl\pi}{N}}, \qquad N > 1.$$

For $N = 2$

$$\begin{aligned} B^4(z) &\approx i\mu_0 \frac{I}{2\pi R} \sum_{l=0}^{3} (-1)^{l+1} e^{i\frac{l\pi}{2}} \left[\left(\frac{z^\star}{R} \right) e^{i\frac{l\pi}{2}} + \left(\frac{z^\star}{R} \right)^2 e^{il\pi} + \ldots \right] \\ &= i\mu_0 \frac{I}{2\pi R} \left[\sum_{l=0}^{3} (-1)^{l+1} e^{i\frac{l\pi}{2}} \left(\frac{z^\star}{R} \right) e^{i\frac{l\pi}{2}} + \sum_{l=0}^{3} (-1)^{l+1} e^{i\frac{l\pi}{2}} \left(\frac{z^\star}{R} \right)^2 e^{il\pi} + \ldots \right] \\ &= i\mu_0 \frac{I}{2\pi R} \left[\left(\frac{z^\star}{R} \right) \underbrace{\sum_{l=0}^{3} (-1)^{l+1} e^{il\pi}}_{(a)} + \left(\frac{z^\star}{R} \right)^2 \underbrace{\sum_{l=0}^{3} (-1)^{l+1} e^{i\frac{3l\pi}{2}}}_{(b)} + \ldots \right]. \end{aligned} \tag{B.5}$$

The term (a) in (B.5) results

$$(a) = \sum_{l=0}^{3} (-1)^{l+1} e^{il\pi} = \sum_{l=0}^{3} (-1)^{l+1} (-1)^{l} = \sum_{l=0}^{3} (-1)^{2l+1} = \sum_{l=0}^{3} (-1) = -4$$

and is the leading order of the Maclaurin expansion, the term (b) represents smaller corrections. As a result, in the limit $|z| \ll R$ results

$$B^2(z) \approx -2i\mu_0 \frac{I}{\pi R^2} z^\star. \tag{B.6}$$

For $N = 3$

$$\begin{aligned} B^6(z) &\approx i\mu_0 \frac{I}{2\pi R} \sum_{l=0}^{5} (-1)^{l+1} e^{i\frac{l\pi}{3}} \left[\left(\frac{z^\star}{R}\right) e^{i\frac{l\pi}{3}} + \left(\frac{z^\star}{R}\right)^2 e^{i\frac{2l\pi}{3}} + \dots \right] \\ &= i\mu_0 \frac{I}{2\pi R} \left[\sum_{l=0}^{5} (-1)^{l+1} e^{i\frac{l\pi}{3}} \left(\frac{z^\star}{R}\right) e^{i\frac{l\pi}{3}} + \sum_{l=0}^{5} (-1)^{l+1} e^{i\frac{l\pi}{3}} \left(\frac{z^\star}{R}\right)^2 e^{i\frac{2l\pi}{3}} + \dots \right] \\ &= i\mu_0 \frac{I}{2\pi R} \left[\left(\frac{z^\star}{R}\right) \underbrace{\sum_{l=0}^{5} (-1)^{l+1} e^{i\frac{2l\pi}{3}}}_{(a)} + \left(\frac{z^\star}{R}\right)^2 \underbrace{\sum_{l=0}^{5} (-1)^{l+1} e^{il\pi}}_{(b)} + \dots \right] \end{aligned} \tag{B.7}$$

The term (a) in (B.7) results

$$\begin{aligned} (a) &= \sum_{l=0}^{5} (-1)^{l+1} e^{i\frac{2l\pi}{3}} \\ &= \left[-1 + e^{i\frac{2\pi}{3}} - e^{i\frac{4\pi}{3}} + e^{i\frac{6\pi}{3}} - e^{i\frac{8\pi}{3}} + e^{i\frac{10\pi}{3}} \right] \\ &= \left[-1 + e^{i\frac{2\pi}{3}} - e^{i\frac{4\pi}{3}} + 1 - e^{i\frac{2\pi}{3}} + e^{i\frac{4\pi}{3}} \right] = 0 \end{aligned}$$

while the term (b) in (B.7) shows

$$(b) = \sum_{l=0}^{5} (-1)^{l+1} e^{il\pi} = \dots = -6$$

and is the leading order of the Maclaurin expansion, further terms represent smaller corrections. Therefore, for $|z| \ll R$ we can write

$$B^6(z) \approx -3i\mu_0 \frac{I}{\pi R^3} (z^\star)^2. \tag{B.8}$$

The results in (B.6) and (B.8) suggest that for $N > 1$ in proximity of $z = 0$ the magnetic field produced by a $2N$-pole of radius R and current I is

$$B^{2N} \approx -Ni\mu_0 \frac{I}{\pi R^N} (z^\star)^{N-1}. \tag{B.9}$$

Let's consider the series expantion in (B.4) and re-write it as

$$\begin{aligned}\sum_{l=0}^{2N-1}(-1)^{l+1}e^{i\frac{l\pi}{N}}\sum_{n=0}^{\infty}\left(\frac{z^\star}{Re^{-i\frac{l\pi}{N}}}\right)^n &= \sum_{n=0}^{\infty}\left(\frac{z^\star}{R}\right)^n\sum_{l=0}^{2N-1}(-1)^{l+1}e^{i\frac{l\pi}{N}}e^{i\frac{nl\pi}{N}}\\ &= \sum_{n=0}^{\infty}\left(\frac{z^\star}{R}\right)^n\sum_{l=0}^{2N-1}(-1)^{l+1}e^{il\frac{n+1}{N}\pi}\\ &= \sum_{n=0}^{\infty}\left(\frac{z^\star}{R}\right)^n\sum_{l=0}^{2N-1}(-1)^{l+1}e^{il\frac{n+1}{2N}2\pi}\end{aligned}$$

The element $\sum_{l=0}^{2N-1}(-1)^{l+1}e^{il\frac{n+1}{N}\pi}$ equivalent to the one in (B.2) and sums to zero unless $n+1=kN$, $k\in\mathbb{N}$ is a integer multiple of N, in which case it reads $\sum_{l=0}^{2N-1}(-1)^{l+1}e^{il\frac{kN}{N}\pi}=\sum_{l=0}^{2N-1}(-1)^{l(1+k)+1}=(-1)^k\,2N$.

The first non-zero element of the Maclaurin expansion is the one corresponding to $k=1$, the next non-zero elements are corrections of the order $O\left((z^\star)^{kN-1}\right)$, $k>1$. Hence, the behavior described by (B.9) represents a very good approximation of the multipole field about the origin.

Bibliography

[1] G. M. M. Sagnac. Léther lumineux démontré par l'effet du vent relatif d'éther dans un interféromètre en rotation uniforme. 157(17):708(10), 1913. 1

[2] B. P. Abbott and LIGO Scientific Collaboration and Virgo Collaboration. Observation of Gravitational Waves from a Binary Black Hole Merger. *Physical Review Letters*, 116(6), February 2016. 1

[3] Ch. Eisele, A. Yu. Nevsky, and S. Schiller. Laboratory Test of the Isotropy of Light Propagation at the 10 17 Level. *Physical Review Letters*, 103(9), August 2009. 1

[4] Shuming Yang and Guofeng Zhang. A review of interferometry for geometric measurement. *Measurement Science and Technology*, 29(10):102001, October 2018. 1

[5] Ian A Robinson and Stephan Schlamminger. The watt or Kibble balance: a technique for implementing the new SI definition of the unit of mass. *Metrologia*, 53(5):A46–A74, October 2016. 1

[6] Andreas Quirrenbach. Optical Interferometry. *Annual Review of Astronomy and Astrophysics*, 39(1):353–401, September 2001. 1

[7] C. Rembe, L. Kadner, and M. Giesen. Approaching attometer laser vibrometry. *Review of Scientific Instruments*, 87(10):102503, October 2016. 1

[8] C.S Adams, M Sigel, and J Mlynek. Atom optics. *Physics Reports*, 240(3):143–210, May 1994. 1, 8

[9] J Baudon, R Mathevet, and J Robert. Atomic interferometry. *Journal of Physics B: Atomic, Molecular and Optical Physics*, 32(15):R173–R195, August 1999. 1

[10] A Miffre, M Jacquey, M Büchner, G Trénec, and J Vigué. Atom interferometry. *Physica Scripta*, 74(2):C15–C23, August 2006. 1

[11] B. Barrett, R. Geiger, I. Dutta, M. Meunier, B. Canuel, A. Gauguet, P. Bouyer, and A. Landragin. The Sagnac effect: 20 years of development in matter-wave interferometry. *Comptes Rendus Physique*, 15(10):875–883, December 2014. 1, 7, 15, 19, 20

[12] A. D. Cronin, J. Schmiedmayer, and D. E. Pritchard. Optics and interferometry with atoms and molecules. *RevModPhys*, 81(3):1051–1129, July 2009. 1, 6, 10, 11, 18, 22

[13] Y. Paturel, J. Honthaas, H. Lefèvre, and F. Napolitano. One nautical mile per month fog-based strapdown inertial navigation system: A dream already within reach? *Gyroscopy and Navigation*, 5(1):1–8, January 2014. 2, 3, 6, 19

[14] H. C. Lef\‘evre. The fiber-optic gyroscope, a century after Sagnac's experiment: The ultimate rotation-sensing technology? *C.R. Phys.*, 15(10):851–858, December 2014. 2, 4, 5, 133

[15] S. Pullen and G. X. Gao. GNSS jamming in the name of privacy. *InsGNSS*, 7(2):34–43, 2012. 2

[16] D. Borio, F. Dovis, H. Kuusniemi, and L. Lo Presti. Impact and Detection of GNSS Jammers on Consumer Grade Satellite Navigation Receivers. *Proceedings of the IEEE*, 104(6):1233–1245, June 2016. 2

[17] F. Dovis and L. Musumeci. Use of the Karhunen–Loève Transform for interference detection and mitigation in GNSS. *ICT Expr.*, 2(1):33–36, March 2016. 2

[18] David H. Titterton and John L. Weston. *Strapdown inertial navigation technology*. Number 5 in IEE radar, sonar, navigation and avionics series. Peregrinus, Stevenage, Herts, 1997. OCLC: 246920262. 2, 4, 5

[19] H. C. Lefèvre. *The fiber-optic gyroscope*. The Artech House applied photonics series. Artech House, Boston, second edition edition, 2014. OCLC: ocn881805657. 2, 4, 5

[20] W. H. K. Lee, H. Igel, and M. D. Trifunac. Recent Advances in Rotational Seismology. *Seismological Research Letters*, 80(3):479–490, May 2009. 3

[21] C. Schmelzbach, S. Donner, H. Igel, D. Sollberger, T. Taufiqurrahman, F. Bernauer, M. Häusler, C. Van Renterghem, J. Wassermann, and J. Robertsson. Advances in 6c seismology: Applications of combined translational and rotational motion measurements in global and exploration seismology. *GEOPHYSICS*, 83(3):WC53–WC69, May 2018. 3

[22] F. Bernauer, J. Wassermann, and H. Igel. Rotational sensors – a comparison of different sensor types. *Journal of Seismology*, 16(4):595–602, October 2012. 3

[23] L. Jaroszewicz, A. Kurzych, Z. Krajewski, P. Marć, Jerzy Kowalski, P. Bobra, Z. Zembaty, B. Sakowicz, and R. Jankowski. Review of the Usefulness of Various Rotational Seismometers with Laboratory Results of Fibre-Optic Ones Tested for Engineering Applications. *Sensors*, 16(12):2161, December 2016. 3

[24] A. A. Velikoseltsev, A. M. Boronakhin, and A. N. Tkachenko. Application of the optical angular rate sensors for rotational measurements in seismology. *Seismic Instruments*, 49(3):229–237, July 2013. 3

[25] A. Di Virgilio, J. Belfi, F. Bosi, F. Morsani, G. Terreni, N. Beverini, G. Carelli, U. Giacomelli, E. Maccioni, A. Ortolan, A. Porzio, C. Altucci, R. Velotta, A. Donazzan, G. Naletto, D. Cuccato, A. Beghi, M.G. Pelizzo, M.L. Ruggiero, A. Tartaglia, G. De Luca, and G. Saccorotti. The GINGER Project. *Nuclear and Particle Physics Proceedings*, 291-293:140–145, October 2017. 3

[26] F. Bosi, G. Cella, A. Di Virgilio, A. Ortolan, A. Porzio, S. Solimeno, M. Cerdonio, J. P. Zendri, M. Allegrini, J. Belfi, N. Beverini, B. Bouhadef, G. Carelli, I. Ferrante, E. Maccioni, R. Passaquieti, F. Stefani, M. L. Ruggiero, A. Tartaglia, K. U. Schreiber, A. Gebauer, and J-P. R. Wells. Measuring gravitomagnetic effects by a multi-ring-laser gyroscope. *Physical Review D*, 84(12), December 2011. 3

[27] J Lense and H Thirring. Über den Einfluss der Eigenrotation der Zentralkourper auf die Bewegung der Planeten und Monde nach der Einsteinschen Gravitationstheorie. *Phys. Z.*, (19):156–63, 1918. 3

[28] C. W. F. Everitt, D. B. DeBra, B. W. Parkinson, J. P. Turneaure, J. W. Conklin, M. I. Heifetz, G. M. Keiser, A. S. Silbergleit, T. Holmes, J. Kolodziejczak, M. Al-Meshari, J. C. Mester, B. Muhlfelder, V. G.

Solomonik, K. Stahl, P. W. Worden, W. Bencze, S. Buchman, B. Clarke, A. Al-Jadaan, H. Al-Jibreen, J. Li, J. A. Lipa, J. M. Lockhart, B. Al-Suwaidan, M. Taber, and S. Wang. Gravity Probe B: Final Results of a Space Experiment to Test General Relativity. *Physical Review Letters*, 106(22), May 2011. 3, 4

[29] J. Belfi, N. Beverini, G. Carelli, A. Di Virgilio, U. Giacomelli, E. Maccioni, A. Simonelli, F. Stefani, and G. Terreni. Analysis of 90 days operation of the gyroscope GINGERINO. *arXiv:1804.02569 [physics]*, April 2018. arXiv: 1804.02569. 3

[30] S Buchman, J A Lipa, G M Keiser, B Muhlfelder, and J P Turneaure. The Gravity Probe B gyroscope. *Classical and Quantum Gravity*, 32(22):224004, November 2015. 4

[31] G. M. Keiser, Saps Buchman, W. Bencze, and D. B. DeBra. The expected performance of Gravity Probe B electrically suspended gyroscopes as differential accelerometers. pages 188–198, Pasadena, California, (USA), 1998. 4

[32] Hervé C. Lefèvre. The fiber-optic gyroscope: Challenges to become the ultimate rotation-sensing technology. *Optical Fiber Technology*, 19(6):828–832, December 2013. 4, 5

[33] Frank Brückner, Daniel Friedrich, Tina Clausnitzer, Michael Britzger, Oliver Burmeister, Karsten Danzmann, Ernst-Bernhard Kley, Andreas Tünnermann, and Roman Schnabel. Realization of a monolithic high-reflectivity cavity mirror from a single silicon crystal. *Phys. Rev. Lett.*, 104:163903, Apr 2010. 5

[34] A A Velikoseltsev, D P Luk'yanov, V I Vinogradov, and K U Shreiber. Super-large optical gyroscopes for applications in geodesy and seismology: state-of-the-art and development prospects. *Quantum Electronics*, 44(12):1151–1156, December 2014. 5

[35] R. W. Dunn, D. E. Shabalin, R. J. Thirkettle, G. J. MacDonald, G. E. Stedman, and K. U. Schreiber. Design and initial operation of a 367-m^2 rectangular ring laser. *Applied Optics*, 41(9):1685, March 2002. 5

[36] B. Culshaw and I. P. Giles. Fibre optic gyroscopes. *Journal of Physics E: Scientific Instruments*, 16(1):5–15, January 1983. 5

[37] L. Marton, J. Arol Simpson, and J. A. Suddeth. Electron Beam Interferometer. *Physical Review*, 90(3):490–491, May 1953. 6, 9

[38] L. Marton, J. Arol Simpson, and J. A. Suddeth. An Electron Interferometer. *Review of Scientific Instruments*, 25(11):1099–1104, November 1954. 6, 9

[39] H. Rauch, W. Treimer, and U. Bonse. Test of a single crystal neutron interferometer. *Physics Letters A*, 47(5):369–371, April 1974. 6

[40] L. Franz S. Altshuer. Matter wave interferometric apparatus, September 1973. 6, 9

[41] V. P. Chebotayev, A. P. Kasantsev, V. P. Yakovlev, and B. Y. Dubetsky. Interference of atoms in separated optical fields. *Journal of the Optical Society of America B*, 2(11):1791, November 1985. 6

[42] J. F. Clauser. Ultra-high sensitivity accelerometers and gyroscopes using neutral atom matter-wave interferometry. *Physica B+C*, 151(1-2):262–272, July 1988. 6

[43] J. F. Clauser. Rotation, acceleration, and gravity sensors using quantum-mechanical matter-wave interferometry with neutral atoms and molecules, October 1989. 6

[44] S. Groth, P. Krüger, S. Wildermuth, R. Folman, T. Fernholz, J. Schmiedmayer, D. Mahalu, and I. Bar-Joseph. Atom chips: Fabrication and thermal properties. *Applied Physics Letters*, 85(14):2980–2982, October 2004. 6, 70, 74

[45] Jakob R. and V. Vuletić, editors. *Atom chips*. Wiley-VCH, Weinheim, Germany, 2011. OCLC: ocn664325852. 6

[46] D. S. Durfee, Y. K. Shaham, and M. A. Kasevich. Long-Term Stability of an Area-Reversible Atom-Interferometer Sagnac Gyroscope. *Physical Review Letters*, 97(24), December 2006. 7, 15

[47] I. Dutta, D. Savoie, B. Fang, B. Venon, C.L. Garrido Alzar, R. Geiger, and A. Landragin. Continuous Cold-Atom Inertial Sensor with 1 nrad / sec Rotation Stability. *Physical Review Letters*, 116(18), May 2016. 7, 18, 19, 21

[48] P. Navez, S. Pandey, H. Mas, K. Poulios, T. Fernholz, and W. von Klitzing. Matter-wave interferometers using TAAP rings. *New Journal of Physics*, 18(7):075014, July 2016. 7, 22, 26, 35, 42

[49] C Ryu and M G Boshier. Integrated coherent matter wave circuits. *New Journal of Physics*, 17(9):092002, September 2015. 7, 22, 43

[50] R. Stevenson, M.R. Hush, T. Bishop, I. Lesanovsky, and T. Fernholz. Sagnac Interferometry with a Single Atomic Clock. *Physical Review Letters*, 115(16), October 2015. 7, 8, 26, 28, 31, 32, 133

[51] T. Fernholz, R. Gerritsma, P. Kr

ger, and R. J. C. Spreeuw. Dynamically controlled toroidal and ring-shaped magnetic traps. *Physical Review A*, 75(6), June 2007. 8, 26, 35, 37, 38, 70, 114, 116, 134, 135

[52] L. Marton. Electron Interferometer. *Physical Review*, 85(6):1057–1058, March 1952. 9

[53] D. W. Keith, M. L. Schattenburg, Henry I. Smith, and D. E. Pritchard. Diffraction of Atoms by a Transmission Grating. *Physical Review Letters*, 61(14):1580–1583, October 1988. 10, 11

[54] O. Carnal and J. Mlynek. Young's double-slit experiment with atoms: A simple atom interferometer. *Physical Review Letters*, 66(21):2689–2692, May 1991. 11

[55] David M. Giltner, R. W. McGowan, and S. A. Lee. Atom Interferometer Based on Bragg Scattering from Standing Light Waves. *Physical Review Letters*, 75(14):2638–2641, October 1995. 11

[56] D. M. Giltner, R. W. McGowan, and S. A. Lee. Theoretical and experimental study of the Bragg scattering of atoms from a standing light wave. *Physical Review A*, 52(5):3966–3972, November 1995. 11

[57] P. R. Berman, editor. *Atom interferometry.* Academic Press, San Diego, 1997. 11

[58] C. Cohen-Tannoudji and D. Guéry-Odelin. *Advances in atomic physics: an overview.* World Scientific, Singapore ; Hackensack, NJ, 2011. OCLC: ocn708357016. 11, 14, 55, 56, 143, 144

[59] Pippa Storey and C. Cohen-Tannoudji. The Feynman path integral approach to atomic interferometry. A tutorial. *Journal de Physique II*, 4(11):1999–2027, November 1994. 14

[60] M. Kasevich and S. Chu. Measurement of the gravitational acceleration of

an atom with a light-pulse atom interferometer. *Applied Physics B Photophysics and Laser Chemistry*, 54(5):321–332, May 1992. 15

[61] M. Kasevich and S. Chu. Atomic interferometry using stimulated Raman transitions. *Physical Review Letters*, 67(2):181–184, July 1991. 15

[62] M. Snadden, J. McGuirk, P. Bouyer, K. Haritos, and M. Kasevich. Measurement of the Earth's Gravity Gradient with an Atom Interferometer-Based Gravity Gradiometer. *Physical Review Letters*, 81(5):971–974, August 1998. 15

[63] J. M. McGuirk, M. J. Snadden, and M. A. Kasevich. Large Area Light-Pulse Atom Interferometry. *Physical Review Letters*, 85(21):4498–4501, November 2000. 15

[64] R. Bouchendira, P. Cladé, S. Guellati-Khélifa, F. Nez, and F. Biraben. New Determination of the Fine Structure Constant and Test of the Quantum Electrodynamics. *Physical Review Letters*, 106(8), February 2011. 15

[65] T. L. Gustavson, P. Bouyer, and M. A. Kasevich. Precision Rotation Measurements with an Atom Interferometer Gyroscope. *Physical Review Letters*, 78(11):2046–2049, March 1997. 15, 19

[66] R. Anderson, H. R. Bilger, and G. E. Stedman. "Sagnac" effect: a century of earth rotated interferometers. *American Journal of Physics*, 62(11):975–985, 1994. 15

[67] Y. Torii, Y. Suzuki, M. Kozuma, T. Sugiura, T. Kuga, L. Deng, and E. W. Hagley. Mach-Zehnder Bragg interferometer for a Bose-Einstein condensate. *Physical Review A*, 61(4), February 2000. 21

[68] Ronald Legere and Kurt Gibble. Quantum scattering in a juggling atomic fountain. *Phys. Rev. Lett.*, 81:5780–5783, Dec 1998. 21

[69] J. C. Hafele and R. E. Keating. Around-the-World Atomic Clocks: Predicted Relativistic Time Gains. *Science*, 177(4044):166–168, July 1972. 23

[70] I. Lesanovsky and W. von Klitzing. Time-Averaged Adiabatic Potentials: Versatile Matter-Wave Guides and Atom Traps. *Physical Review Letters*, 99(8), August 2007. 26, 35, 41

[71] W. H. Heathcote, E. Nugent, B. T. Sheard, and C. J. Foot. A ring trap for ultracold atoms in an RF-dressed state. *New J. Phys.*, 10(4):043012, 2008. 26, 42

[72] Y. Che, F. Yao, H. Liang, G. Li, and X. Wang. Unconventional Geometric Sagnac Interferometer for Rotation Sensing. *arXiv:1805.12554 [quant-ph]*, May 2018. arXiv: 1805.12554. 28, 31, 32

[73] J. Anandan. Sagnac effect in relativistic and nonrelativistic physics. *Phys. Rev. D*, 24:338–346, Jul 1981. 29

[74] D. Dieks and G. Nienhuis. Relativistic aspects of nonrelativistic quantum mechanics. *American Journal of Physics*, 58(7):650–655, 1990. 29

[75] S. Blanes, F. Casas, J.A. Oteo, and J. Ros. The Magnus expansion and some of its applications. *Physics Reports*, 470(5-6):151–238, January 2009. 31

[76] J. Dalibard and C. Cohen-Tannoudji. Dressed-atom approach to atomic motion in laser light: the dipole force revisited. *J. Opt. Soc. Am. B*, 2(11):1707–1720, Nov 1985. 32

[77] Christopher J. Foot. *Atomic physics*. Oxford master series in atomic, optical and laser physics. Oxford Univ. Press, Oxford, reprinted edition, 2011. OCLC: 844787305. 33, 43, 51, 52, 54, 55, 56, 66, 99, 139, 140, 141, 142, 143, 144

[78] O. Zobay and B. M. Garraway. Two-dimensional atom trapping in field-induced adiabatic potentials. *Phys. Rev. Lett.*, 86:1195–1198, Feb 2001. 35

[79] E. Majorana. Atomi orientati in campo magnetico variabile. *Il Nuovo Cimento*, 9(2):43–50, February 1932. 35, 56

[80] J. B. Johnson. Thermal agitation of electricity in conductors. *Phys. Rev.*, 32:97–109, Jul 1928. 41

[81] H. Nyquist. Thermal agitation of electric charge in conductors. *Phys. Rev.*, 32:110–113, Jul 1928. 41

[82] K. Henderson, C. Ryu, C. MacCormick, and M. G. Boshier. Experimental demonstration of painting arbitrary and dynamic potentials for Bose–Einstein condensates. *New Journal of Physics*, 11:043030, April 2009. 43

[83] T. A. Bell, J. A. P. Glidden, Leif Humbert, M. W. J. Bromley, S. A. Haine, M. J. Davis, T. W. Neely, M. A. Baker, and H. Rubinsztein-Dunlop.

Bose–Einstein condensation in large time-averaged optical ring potentials. *New Journal of Physics*, 18(3):035003, March 2016. 43

[84] T. Bishop. *A Guided Matter-Wave Sagnac Interferometer*. PhD thesis, University of Nottingham, Nottingham, April 2018. 46, 71, 74, 76, 133

[85] S. Jammi, T. Pyragius, M. G. Bason, H. M. Florez, and T. Fernholz. Dispersive detection of radio-frequency-dressed states. *Physical Review A*, 97(4), April 2018. 48, 87, 101, 103, 104

[86] S. Jammi. *Towards Quantum Optics Experiments with trapped atoms in a Hollow-Core Fibre*. PhD thesis, University of, Nottingham, September 2017. 48, 87, 101, 103, 104

[87] Wenhui Li, I. Mourachko, M. W. Noel, and T. F. Gallagher. Millimeter-wave spectroscopy of cold Rb Rydberg atoms in a magneto-optical trap: Quantum defects of the *ns* , *np* , and *nd* series. *Physical Review A*, 67(5), May 2003. 51

[88] D. A. Steck. Quantum and Atom Optics, October 2018. 52, 53, 54, 141, 142

[89] D. A. Steck. Rubidium 87 D Line Data, January 2015. 52, 53, 141, 142

[90] S Bize, Y Sortais, M. S Santos, C Mandache, A Clairon, and C Salomon. High-accuracy measurement of the ^{87} Rb ground-state hyperfine splitting in an atomic fountain. *Europhysics Letters (EPL)*, 45(5):558–564, March 1999. 53

[91] J. Ye, S. Swartz, P. Jungner, and J. L. Hall. Hyperfine structure and absolute frequency of the 87 rb 5p3/2 state. *Optics Letters*, 21(16):1280, August 1996. 53

[92] Y. B. Ovchinnikov, K. Szymaniec, and S. Edris. Measurement of rubidium ground-state hyperfine transition frequency using atomic fountains. *Metrologia*, 52(4):595–599, August 2015. 53

[93] W. Petrich, M. H. Anderson, J. R. Ensher, and E. A. Cornell. Stable, Tightly Confining Magnetic Trap for Evaporative Cooling of Neutral Atoms. *Physical Review Letters*, 74(17):3352–3355, April 1995. 56

[94] M. Weel and A. Kumarakrishnan. Laser-frequency stabilization using a lock-in amplifier. *Canadian Journal of Physics*, 80(12):1449–1458, December 2002. 66

[95] T. Pyragius. Developing and building an absorption imaging system for Ultracold Atoms. *arXiv:1209.3408 [physics]*, September 2012. arXiv: 1209.3408. 68

[96] D. A. Smith, S. Aigner, S. Hofferberth, M. Gring, M. Andersson, S. Wildermuth, P. Krueger, S. Schneider, T. Schumm, and J. Schmiedmayer. Absorption imaging of ultracold atoms on atom chips. *Optics Express*, 19(9):8471, April 2011. 68

[97] P. Treutlein. *Coherent manipulation of ultracold atoms on atom chips*. PhD thesis, Ludwig–Maximilians–Universitat Munchen, February 2008. 70, 74

[98] J.R. Johansson, P.D. Nation, and F. Nori. QuTiP 2: A Python framework for the dynamics of open quantum systems. *Computer Physics Communications*, 184(4):1234–1240, April 2013. 100

[99] J.R. Johansson, P.D. Nation, and F. Nori. QuTiP: An open-source Python framework for the dynamics of open quantum systems. *Computer Physics Communications*, 183(8):1760–1772, August 2012. 100

[100] Christian Gross and Immanuel Bloch. Quantum simulations with ultracold atoms in optical lattices. *Science*, 357(6355):995–1001, September 2017. 113

[101] P. M. Preiss, R. Ma, M. E. Tai, A. Lukin, M. Rispoli, P. Zupancic, Y. Lahini, R. Islam, and M. Greiner. Strongly correlated quantum walks in optical lattices. *Science*, 347(6227):1229–1233, March 2015. 113

[102] M. Lohse, C. Schweizer, O. Zilberberg, M. Aidelsburger, and I. Bloch. A Thouless quantum pump with ultracold bosonic atoms in an optical superlattice. *Nature Physics*, 12(4):350–354, April 2016. 113

[103] Michael Lohse, Christian Schweizer, Hannah M. Price, Oded Zilberberg, and Immanuel Bloch. Exploring 4d quantum Hall physics with a 2d topological charge pump. *Nature*, 553(7686):55–58, January 2018. 113

[104] N Horiguchi, T Oka, and H Aoki. Non-equilibrium dynamics in Mott-to-superfluid transition in Bose-Einstein condensation in optical lattices. *Journal of Physics: Conference Series*, 150(3):032007, February 2009. 113

[105] Yibo Wang, Prince Surendran, Smitha Jose, Tien Tran, Ivan Herrera, Shannon Whitlock, Russell McLean, Andrei Sidorov, and Peter Hannaford. Magnetic lattices for ultracold atoms and degenerate quantum gases. *Science Bulletin*, 61(14):1097–1106, July 2016. 114

[106] G. A. Sinuco-León and B. M. Garraway. Radio-frequency dressed lattices for ultracold alkali atoms. *New J. Phys.*, 17(5):053037, 2015. 114

[107] R. Folman, P. Kruger, J. Schmiedmayer, J. Denschlag, and C. Henkel. Microscopic atom optics: from wires to an atom chip. *arXiv:0805.2613 [quant-ph]*, May 2008. arXiv: 0805.2613. 114

[108] Luigi Amico, Gerhard Birkl, Malcolm Boshier, and Leong-Chuan Kwek. Focus on atomtronics-enabled quantum technologies. *New Journal of Physics*, 19(2):020201, February 2017. 114

[109] Luigi Amico, Andreas Osterloh, and Francesco Cataliotti. Quantum Many Particle Systems in Ring-Shaped Optical Lattices. *Phys. Rev. Lett.*, 95(6):063201, August 2005. 114

[110] Luigi Amico, Davit Aghamalyan, Filip Auksztol, Herbert Crepaz, Rainer Dumke, and Leong Chuan Kwek. Superfluid qubit systems with ring shaped optical lattices. *Scientific Reports*, 4:4298, March 2014. 114

[111] CERN Accelerator School on Measurement and alignement of accelerator and detector Magnets. *Basic Theory of Magnets*, number pp. 1-26, April 1997. 114

[112] B. Numerov. Note on the numerical integration of d2x/dt2 =f(x,t). *Astronomische Nachrichten*, 230(19):359–364, 1927. 124

[113] C. Rossetti. *Rudimenti di meccanica quantistica*. Levrotto e Bella, Torino, 2008. OCLC: 928876669. 139, 140, 141

[114] G. Ambrosio and G. Bellomo. Magnetic field, multipole expansion and peak field in 2d for superconducting accelerator magnets. Technical Report INFN-TC-96-15, INFN, 10 1996. 146